DEVELOPMENT AND APPLICATION OF AN ELECTROSPRAY IONIZATION ION MOBILITY-MASS SPECTROMETER USING AN RF ION FUNNEL AND PERIODIC-FOCUSING ION GUIDE

A Dissertation

by

JUNHO JEON

Submitted to the Office of Graduate and Professional Studies of
Texas A&M University
in partial fulfillment of the requirements for the degree of

DOCTOR OF PHILOSOPHY

Chair of Committee,	David H. Russell
Committee Members,	Emil A. Schweikert
	Simon W. North
	James C. Sacchettini
Head of Department,	David H. Russell

December 2013

Major Subject: Chemistry

ABSTRACT

A novel ion mobility-mass spectrometer was designed and built in order to achieve high transmission and high resolution for observing desolvated ion conformations of chemical and biological molecules in the gas phase. The instrument incorporates a home-built electrospray ionization (ESI) source and rf ion funnel(IF) as an ion transfer interface, modular periodic-focusing ion guide (PFIG) as a drift tube (DT) for arrival time measurement, and orthogonally accelerated linear time-of-flight mass spectrometer to maximize analytical figures-of-merit of the instrument including sensitivity and separation of gas-phase ions.

The rationales for implementation of each device aforementioned are discussed as enhanced ion focusing to reduce data acquisition time of the instrument, high mobility resolution (R > 56) to separate ions having a small collision cross section (CCS) difference at low-to-intermediate field strength (10 V cm^{-1} $torr^{-1}$~19 V cm^{-1} $torr^{-1}$), and observation of multiple conformers from isobaric ions at various operation conditions. Gate and transfer ion optic design needed to avoid detrimental gas dynamic effect is presented during hybridization of PFIG into ESI mass spectrometer. The details of instrumentation and electrode/voltage schematics are also discussed along with SIMION calculation results.

The characteristic drift motions of ions inside the PFIG require a normalization procedure to compare CCS values from the instrument with the results using conventional uniform field DT ion mobility-mass spectrometry (IM-MS). Through experimental measurements and ion trajectory calculations from well known model peptides and proteins having multiple charge states, a correlation factor α which links the results from the two different types of instrumentation was derived and successfully applied (within ±4% difference).

Ion heating was also investigated using ubiquitin, insulin, and substance P. Using ESI PFIG-MS, A significant variation of the arrival time distribution at different heated capillary temperature, rf amplitude, and electric field strength was observed for ubiquitin (+7) and (+8) and substance P (+3), while a substantial change was not observed for insulin owing to structural rigidity of disulfide bond cross-linking between two chains. The results imply that ESI PFIG-MS provides a window to monitor conformational variation of gas-phase ions and measure energy barriers of peptide/protein folding processes, which can allow us to reveal pathways in structural energy landscape.

DEDICATION

This dissertation is dedicated to my mother who has committed her life to giving the best education to her three children; to my wife, for accompanying me in this journey with love and courage; and to my two kids for being my great joy and for trying to understand what dad is doing.

ACKNOWLEDGEMENTS

I would first like to thank Dr. David H. Russell for guiding the research and providing the resources for this scientific endeavor. He presented me with the opportunity for invaluable hands-on experience with mass spectrometry instrumentation, from designing to trouble-shooting and this has allowed me to develop a clear understanding of ion-mobility instruments.

Thanks also go to Dr. Kent J. Gillig and Dr. Jody C. May for their help and advice during the early days of my research. I would like to express my appreciation to Greg Matthijetz for sharing his expertise in electronics and implanting LabView® control in the instrument. My former and present colleagues in the Russell research group were essential in making the research possible and I have been blessed with valuable discussions with them, especially, the instrumentation subgroup members, Dr. Chaminda Gamage, Dr. Ryan Blase, Dr. Kevin Kmiec, Joshua Silveira, Kyle Fort, Nicole Wagner, and Kelly Servage. The technical support from Will Seward and Carl Johnson at the Department of Chemistry machine shop is appreciated for the high quality of their work.

I acknowledge the financial support provided for this research by the National Science Foundation, the Welch Foundation, the U. S. Department of Energy, and the Department of Chemistry at Texas A&M University. I also thank the committee members, Dr. Simon W. North, Dr. Emile A. Schweikert, and Dr. James C. Hu for their valuable suggestions and comments throughout this research.

It has been a great experience in my lifetime to enjoy this scientific endeavor that has led to building a very special instrument trough which I can focus my eyes all the way down to the metamorphosis of molecules levitated and flown ‘in the name of electric field energy’, which I have never dreamed at this tiny scale.

NOMENCLATURE

AP	Atmospheric Pressure
API	Atmospheric Pressure Ionization
ATD	Arrival Time Distribution
CCS	Collision Cross Section, Ω
CD	Circular Dichroism
CID	Collision Induced Dissociation
CFD	Computational Fluid Dynamics
CM	Center-of-Mass
CV	Compensation Voltage
DT	Drift Tube
DTIM	Drift Tube Ion Mobility
DV	Dispersion Voltage
ESI	Electrospray Ionization
FAIMS	Field-Asymmetric waveform Ion Mobility Spectrometry
FT-ICR	Fourier Transform-Ion Cyclotron Resonance
HC	Heated Capillary
HPLC	High-Performance Liquid Chromatography
i. d.	Inner Diameter
IF	Ion Funnel
IM	Ion Mobility

IM-MS	Ion Mobility-Mass Spectrometry
IMS	Ion Mobility Spectrometry
M	the Mach Number
MALDI	Matrix-Assisted Laser Desorption Ionization
MD	Molecular Dynamics
NMR	Nuclear Magnetic Resonance
MS	Mass Spectrometry
oa	Orthogonally Accelerated
o. d.	Outer Diameter
PEEK	Polyether ether ketone
PFIG	Periodic-Focusing Ion Guide
Qq	Quadrupole-Quadrupole
SAIMS	Selected-ion Accumulation Mobility Spectrometry
SNR	Signal-to-Noise Ratio
TDC	Time-to-Digital Converter
TOF	Time-of-Flight
TTL	Transistor-Transistor Logic
TW	Traveling Wave

TABLE OF CONTENTS

Page

LIST OF FIGURES

LIST OF TABLES

CHAPTER I

INTRODUCTION TO ELECTROSPRAY IONIZATION ION MOBILITY-MASS SPECTROMETRY

Overview

Mass spectrometry (MS) has advanced significantly over the last several decades owing to the demands for analysis of highly complex chemical/biological samples. Many of the advances have been driven by the field of proteomics[1]. The advance in hybridization of ion mobility (IM) and MS has become one of the most powerful tools in instrumental analysis over the last two decades[2]. IM is a simple separation method for gas-phase ions based on their migration velocity along a gas-filled tube under the influence of an external electric field. The simplicity of instrumentation, selectivity, and speed of analysis have encouraged widespread usage of IM spectrometry (IMS)[3]. On top of these advantages, the hybridization of IM with MS offers a multi-dimensional interpretation of analytical data not possible by each technique alone. It also serves as a conformation probe of gas phase ions[4]. Recently, primarily owing to the advent of electrospray ionization (ESI) and matrix-assisted laser desorption ionization (MALDI)[4c, 5], IM-MS has provided new capability presenting a bright future for investigation of protein/peptide folding structures and interactions through valuable collision cross section (CCS) data[6]. For example, the process of metalation and demetalation of human metallothionein has been investigated by mass-selected collision-induced dissociation (CID) IM-MS. Such studies show that the first four Cd^{2+} ions are located in the α

domain and additional Cd^{2+} ions go to the β-domain[7]. The monovalent-specific ion channel study using gramicidin A reveals that the Na^+-binding form closely resembles the neutral conformer, whereas K^+ and Cs^+ complexes are quite different even though the free energy of each conformation from molecular dynamics (MD) calculations is similar, strongly indicating wide structural flexibility[8]. The CCS values from singly charged tryptic peptides of cytochrome c formed by MALDI do not differ greatly from those ions formed from ESI within ± 8%, which suggests compatibility of the two ionization sources for low charge states[9]. All these advancements underscore the importance of development of new techniques which can tackle current research issues and push the limits using convergence of available up-to-date technologies and new concepts.

Types of Ion Mobility-Mass Spectrometers

There are two major types of ion mobility techniques adaptable to MS. First, field-asymmetric waveform ion mobility spectrometry (FAIMS), also known as differential mobility spectrometry (DMS), separates gas-phase ions at atmospheric pressure using alternating positive/negative asymmetric square waveform (‘dispersion voltage’, DV) across two electrodes (cylindrical or planar) which causes oscillation of ions in the middle of the electrodes[10]. The compensation voltage (CV) can be adjusted to selectively pass ions through the device which is mounted on the front of the mass spectrometer. Because of its small size and add-on type instrumentation, FAIMS has a broad applicability field[11]. However, although FAIMS can achieve efficient ion separation within a small fraction of time, the complicated waveforms and high field condition hinders direct extraction of conformational information, specifically CCS.

The second IM instrument type is drift tube (DT) IM which was developed in the 1950s. This apparatus consists of stacked ring electrodes having wide i. d. to generate a low uniform electric field across a cylindrical cell (0.05 m to 2 m) filled with inert gases. The coupling of IM to MS requires a conductance limit at the end of the DT since it operates at much higher pressure (1~700 torr) compared with the MS detector region (10^{-5}~10^{-7} torr). Under a weak electric field, ion packets are gated and they achieve characteristic steady state drift velocities related to their CCS. Different arrival time distribution (ATD) for mass-selected ions are recorded by the MS (quadrupole or time-of-flight (TOF)) as shown in Figure 1; the drift time (t_d) required for the ions is obtained by subtraction of the out-of-drift cell from their arrival time (AT) using variation of the field strength. The CCS is calculated from the ATD which is referenced to the centroid of one of the peaks maintaining a constant profile over different field strengths using the Mason-Schamp equation[12].

Owing to the direct relationship between t_d and CCS in the equation, DTIM is favored for empirical determination of CCS. However, inherent radial diffusion of ions crossing the drift tube and duty cycle of gating result in ion loss which degrades the sensitivity of DTIM-MS. To address the low ion transmission, traveling wave (TW) DTIM-MS was developed by Giles *et al*.[13] This modified version of DTIM-MS utilizes rf confinement to lessen ion loss during drift motion and deliver the ions by continuous sweeping dc pulse along the stacked ring electrodes instead of adapting the potential gradient. A commercialized version of the instrumentation has been widely used in many areas owing to high ion transmission with moderate IM resolution coupled to high resolution MS, although other studies have claimed ion heating from it[14].

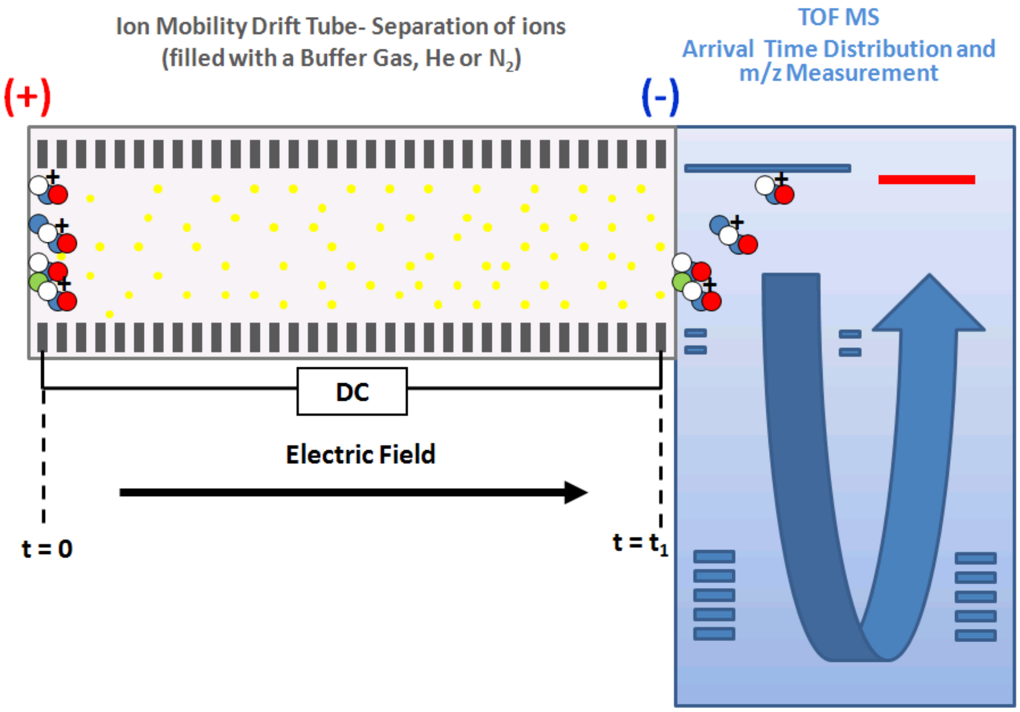

Figure 1. Schematic of DTIM-MS. The DT consists of a stack of ring electrodes which have the same dimension. The gap between the electrodes is much less than the i. d. of the electrode to minimize the distortion of the field. Various types of MS can be used for detection of ions and TOF MS is presented in the schematic.

Fundamentals of Drift Tube Ion Mobility

The DTIM is based on ion drift velocities (v_d) in a buffer gas under an electric field (E)[12, 15].

$$v_d = KE \tag{1.1}$$

A pulsed packet of ions is injected into a drift tube typically filled with helium (He) or N_2. After ion injection, E applied across the drift tube causes the ion packet to move towards the exit of the tube. Due to the balance between the forces imposed by a given E and ion-neutral collisions, the ion packet has a steady state drift velocity v_d. During the travel, the localized packet of ions becomes dispersed through the neutral gas by the gradient in their spatial concentration.

The mathematical expression for this process can be simplified by momentum-transfer theory which considers the momentum and energy balance for the ions between acceleration and collision[15b]. Under constant pressure and temperature, K depends on the number of collisions when the ions encounter the buffer gas and it is largely affected by ionic mass, the charge of the ion, and the gas pressure. The CCS (Ω) of the ion is determined from mobility measurement from the equation

$$K = \frac{3}{16}\frac{q}{N}\left(\frac{1}{m_i}+\frac{1}{m_g}\right)^{\frac{1}{2}}\left(\frac{2\pi}{k_B \mathrm{T}}\right)^{\frac{1}{2}}\frac{1}{\Omega} \qquad (1.2)$$

where q is the charge of the ion, N is the gas number density, k_B is the Boltzmann constant, T is the gas temperature in kelvin, and m_i and m_g are the mass of the ion and the mass of the gas molecule, respectively. This expression for ion transport originates from taking averages of momentum loss per collision and few approximations under a low electric field strength; it is assumed that the ion kinetic energy resulting from field-directed motion is much less than the thermal energy. K is independent under low electric field condition. Although the error from the equation can be reduced when higher Chapman-Enskog approximations are considered, the improvement amounts to less than 2% for ions whose masses are equal to or greater than the mass of the gas molecule[15b]. In general, the measured mobility K is converted to the reduced mobility K_0 using the standard pressure normalized to 0℃ (P_0) for comparison,

$$K_0 = \frac{P}{760}\frac{273.15}{\mathrm{T}}K = \frac{P_0}{760}K \tag{1.3}$$

where P is the gas pressure in torr during the experiment. From the definition of v_d for an ion traveling the drift tube length (L) during the time (t_d), K_0 can be written as

$$\frac{t_d E}{L} = \frac{1}{K} \tag{1.4}$$

Substituting K from equation (1.4) into (1.3) yields

$$\frac{1}{K_0} = \frac{760}{p}\frac{\mathrm{T}}{273.15}\frac{1}{K} = \frac{760}{p}\frac{\mathrm{T}}{273.15}\frac{t_d E}{L} \tag{1.5}$$

Then, by substituting equation (1.5) into the mobility equation (1.2) followed by rearrangement of terms, the equation below for Ω is obtained.

$$\Omega = \frac{3q}{16N_0}\left(\frac{2\pi}{\mu k_B \mathrm{T}}\right)^{\frac{1}{2}}\frac{t_d E}{L}\frac{760}{P}\frac{\mathrm{T}}{273.15} \tag{1.6}$$

Here, N is converted to N_0 (Loschmidt constant, $2.69 \times 10^{19}\mathrm{cm}^{-3}$) since the K is reduced to the standard temperature and pressure and μ is the reduced mass ($1/\mu = 1/m_i + 1/m_g$). Thus, experimentally measured drift time (t_d) provides information needed to calculate CCS.

IM-MS measurement yields CCS of mass-selected conformers and it is necessary to employ MD simulations to understand distinctive ion shapes[5a]. CCS calculations are performed on the conformations generated from MD results using MOBCAL software package[16] providing three options: projection approximation (PA), exact hard-sphere scattering (EHSS)[17], and trajectory method (TM)[18]. PA is the simplest among the calculation methods; it determines the CCS from orientational averaging of the projected area of a structure. EHSS is the calculation method for CCS that uses the assumption of elastic hard-sphere collision between the molecule and monoatomic gas. TM considers ion-neutral interaction during collision from a spherical gas molecule and the atoms in an ion but TM computing is expensive. Calculated CCSs are filtered by empirical CCS data within a predefined precision (*ca*. ± 3%) and corresponding structures within the range are clustered by their characteristic conformational index (for example, backbone shape) with percent populations of each cluster out of the total corresponding candidates.

ESI IM-MS and Analytical Figures of Merit

The ion generation for IM-MS studies is typically performed through either ESI or MALDI[4c, 19]. ESI generates multiply charged ions while primarily singly charged ions are generally produced in MALDI[20]. Coupling of ESI source to IM-MS has been of special interest because it allows seamless conformational investigation from solution phase to gas phase. According to the recent study of Pierson *et al.*[21], high resolution ESI IM-MS can identify 10 different gas-phase conformations of bradykinin (+3) ion at different solvent compositions. The number of conformations appearing varies as the ratios of solvents change, which means that a peptide/protein may have more than a single geometry in solution phase. The ability of characterizing multiple structures in solution phase of peptide/protein by ESI IM-MS can be hardly expected from traditional methods including nuclear magnetic resonance (NMR).

Also, multiply charged ions experience larger drift forces than singly charged ions in a given electric field and different charge states from isobaric ions will be separated on different trendlines in the conformational space (mobility time vs. m/z)[22], reducing congestion of mass spectral information and increasing sequence coverage. Since the single peak resolution of IM-MS (R_P) is defined by the ratio of the drift time at the peak centroid (t_d) to the full width at half maximum of the peak (Δt_{fwhm}),

$$R_\mathrm{P} = \frac{t_d}{\Delta t_{fwhm}} \tag{1.7}$$

the merit of high peak capacity can be enhanced by achieving a longer drift time and narrower peak width. Assuming that the inevitable diffusion through axial and radial direction is the only detrimental factor, diffusion-limited mobility resolution (R_d) is increased by higher charge states from ESI due to the fact that it is proportional to the square root of the charge on the ion[12, 23].

$$R_d = \left(\frac{ELq}{16k_BT\ln 2}\right)^{\frac{1}{2}} \tag{1.8}$$

To increase the mobility resolution, a high E or long DT can be chosen. Cryogenic DTIM may be an alternative to reduce the ion diffusion from thermal motion and to increase the resolution.

In terms of the separation time domain, IM-MS typically has a very narrow time window of 0.1-50 ms for IM and ~10 µs for MS, compared to a few minutes to hours for liquid chromatography or capillary electrophoresis[22b, 24], depending on the drift tube length, m/z of ions and electric field.

In summary, the major advantages of ESI IM-MS are the determination of multiple conformations originated from solution phase and fast separation of multiply charged ions from μs to ms even for isobaric ions in the gas phase, which cannot be achieved through conventional techniques. Based on these premises, this research has focused on development of a versatile high resolution/high transmission ESI IM-MS instrument to accommodate all aforementioned technological merits. To implement the goal, the present study has explored the coupling of a homebuilt ESI source featuring an rf ion funnel interface[25] and a novel modular periodic-focusing ion guide (PFIG)[26] as an ion mobility drift tube attached to an orthogonal TOF MS. The figures of merit for each device and the considerations for building the instrument will be discussed in detail along with application results.

CHAPTER II

FUNDAMENTALS OF PERIODIC-FOCUSING ION GUIDE ION MOBILITY-MASS SPECTROMETER

Uniform Field Drift Tube Ion Mobility

For measurement of ATDs for the purpose of CCS determination, it is essential to create a uniform electric field. Homogeneous electric field is critical for reducing deviations in the ion drift motion. The inherent field quality from electrodes and drift tube design can be verified through ion trajectory calculation using the SIMION software package. SIMION generates the potential array representing a collection of a square mesh of points to calculate the electrostatic fields. Because the electrode geometry is designated for particular array points by the user, these array points have fixed potentials. The electrostatic potentials beyond the electrodes can be determined by solving a differential equation with boundary values using Laplace operator ($\nabla\cdot\nabla$, ∇^2, or Δ) representing the divergence of the gradient of a function on Euclidean space, commonly defined by Cartesian coordinates. In a Cartesian coordinate system, the Laplacian to the electric potential is given by the sum of the second partial derivatives of the function with respect to each independent variable,

$$\nabla^2 V = \nabla \cdot \nabla \mathrm{V} = \nabla \cdot \mathrm{E} = \frac{\partial \mathrm{E_x}}{\partial \mathrm{x}} + \frac{\partial \mathrm{E_y}}{\partial \mathrm{y}} + \frac{\partial \mathrm{E_z}}{\partial \mathrm{z}} \qquad (2.1)$$

To solve the equation, SIMION uses a finite difference method to estimate the value of each point by averaging its nearest points with an over-relaxation technique until the potential of each point reaches a stable solution value ("refining")[27]. After all array potentials are determined, ions are allowed to traverse the potential array volume defined by symmetry assumption (planar, cylindrical) at the beginning of the potential array generation. Ion trajectory calculations are performed to acquire electrostatic forces at the current location of the ion, and ion acceleration by the applied forces is calculated from the numerical integration algorithm (fourth order Runge-Kutta method is used) to predict the position and velocity of the ion at the next time step. Since IM-MS is performed under the pressurized cell, ion-neutral collisions are inevitable and it requires an appropriate collision model. The program option in SIMION 8.0 uses the elastic hard-sphere collision model coded with Lua programming language[28].

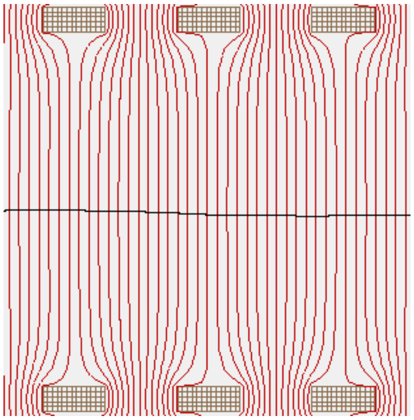

Figure 2. Ion trajectory calculation from SIMION under a dc gradient in a uniform field DT. The solid black line represents the ion trajectory and the rectangles are electrodes. The red lines are equipotential lines perpendicular to the field direction. The elastic hard-sphere collision model was used for ion-neutral collision at 1.0 torr (He) with $C60^{+\cdot}$ model ion.

Figure 2 exhibits an example of ion flight through a uniform field DT at 1.0 torr He pressure. There are distortions around the electrode edges yet at the center the equipotential lines are parallel to each other and homogeneous. The model ion ($C60^{+\cdot}$) shows very linear axial drift motion and the length of the drift cell is almost the same as the distance of the ion traveled.

The homogeneity of the field in DT is optimized when the ratio of the thickness to the i. d. of the ring electrode is kept to a minimum (< 0.1) and the spacing between the electrodes must be considered for minimizing the field distortion from the grounded metallic enclosure[29]. Moreover, the matching of gate geometry and its size should be considered to see if the homogeneity of the electric field in front of DT can be degraded by fringing field. As long as the inherent homogeneity from electrode geometry is maintained, the length of the DT is irrelevant to the field quality. Therefore, a long DT increases the resolution in IM-MS.

Periodic-Focusing Ion Guide

As ions propagate through the uniform field DT, radial diffusion is unavoidable. From the IM resolution equation in the previous chapter, high resolution separation is obtainable using a low temperature to minimize the thermal diffusion, longer DT, and high electric field. The ultimate IM-MS performance related to high resolution and high transmission, however, is dependent on diffusion since the radial diffusion increases as the length of the DT increases. It becomes highly detrimental to ion transmission owing to the conductance limiting aperture of the drift tube exit (*ca*. ~ 0.5mm) in IM-MS instrumentation. At high electric field, the operation of IM-MS is made more difficult by electrical breakdown of the buffer gas (He)[30]. Thus, increasing pressure and field strength together may help to increase resolution but the gas load to MS must also be considered.

Periodic-focusing ion guide (PFIG) developed by Gillig *et al*.[26] can address this complication. The characteristic geometry of PFIG electrodes generates effective potential in the inertial frame from dc. The origin of effective potential depending on electrode design and their focusing effect have been explained well in our previous results[31]. Briefly, PFIG generates a fringing field near the electrode edges by dc gradient.

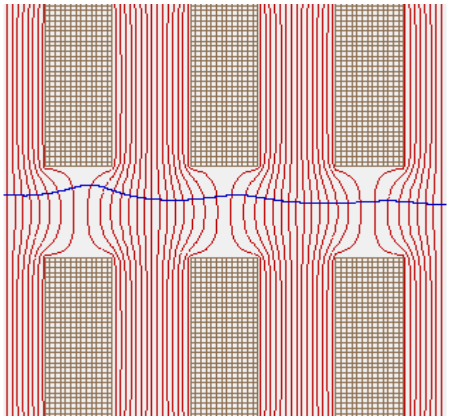

Figure 3. Ion motion in PFIG using SIMION under dc gradient. The sinusodial blue line represents the ion trajectory and the rectangles are electrodes (thickness: spacing: i. d.= 3:3:4).

The repetitive pattern of this fringing field is determined by the ring electrode geometry (the ratio of thickness, spacing, and i. d.). Note that this field pattern is caused by the potential drop across the region. Thus, ions traveling along the axial and radial direction experience the repetitive potential variation (but still in the gradient) which results in the pseudo-sinusoidal ion motion in Figure 3. As shown in the trajectory, the linear axial drift motion is not dominant any more compared to that in Figure 2. In the middle of the electrodes, the ion approaches the electrode (radial ripple motion) and in the gap between two electrodes, it moves toward the central axis (central drift motion).

Usually the time-varying rf electric field with opposite phase on neighboring electrodes generates a time-averaged static effective potential (or "pseudopotential") barrier and in turn, guides macroscopic sinusoidal motion. Similar phenomena occur when ions are moving fast in the stacked ring electrodes wherein each pair of electrodes have alternatively negative and positive dc voltages[32]. Since the ion feels a spatial potential periodicity (z_0, [m]), the frequency depending on the velocity of the ion (v) can be expressed by sinusoidal variation

$$f = \frac{v}{2\pi z_0} \text{ [Hz]} \tag{2.2}$$

or

$$\omega = 2\pi f = \frac{v}{z_0} \text{ [rad]} \tag{2.3}$$

The potential drop across PFIG produces acceleration of positively charged particles toward negative potential as in the uniform field DT. Therefore, the fringing potential variation from the thick electrode edge is superimposed on top of the linear axial potential gradient slope. Investigation of field strength by flying ions in SIMION also reveals that there are local electric field oscillations which are low in the middle of the electrodes and high in the spacing to adjacent electrodes, reflecting potential oscillations. The magnitude of the effective potential $V^*(r)$, which the ion feels in radial position (r), is defined by the well-known pseudopotential equation

$$V^*(r) = \frac{q^2 E(r)^2}{4m_i \omega^2} = \frac{q^2 E(r)^2 {z_0}^2}{4m_i v^2} \tag{2.4}$$

Therefore, at a given periodicity z_0 (intrinsic property from specific electrode geometry), the electric field increment across PFIG sufficiently amplifies the fringing field which maintains the focusing by the effective potential. However, since the velocity of the ion also depends on its mobility and the acceleration by the field is different in the location, the effective potential would not have a straightforward relationship with the velocity of the ion. The potential variation within z_0 is not large compared with the overall axial dc potential gradient[31a, 31c] and the magnitude of the effective potential in periodic motion would be smaller than that of ordinary rf ion guides.

In addition, owing to the conducting thick electrodes, the field free region exists in the middle of the electrode like a Faraday cup, which can be negligible in case of a thin ring electrode, and it plays a major role in motion of ions as in Figure 3. When the ion travels the spacing between the electrodes, they are accelerated and focused to the center axis by electric field distortion of the fringing field and the voltage drop across. However, when the ion travels in the middle of the electrode, it might not be accelerated and collide with buffer gas molecules which leads to collisional cooling. If ions do not have enough kinetic energy by acceleration before the field free region, they would be neutralized by the electrode. The ion motion in this region could be another reason that PFIG requires a minimum field strength to keep ions collimated[31a]. When they approach the exit edge of the electrode, they are re-accelerated by the voltage drop across to the adjacent electrode direction.

Analytical Advantages of Periodic-Focusing Ion Guide

The largest benefit of PFIG in IM-MS instrumentation is to reduce the diffusion of ion swarms when they reach the conductance limit. The ion transmission can be enhanced by a factor of 40 compared to the uniform field DTIM-MS in the case of MALDI without severe degradation in the mobility resolution as reported by Blase *et al*[31b]. The consequential motion of ions in PFIG is similar in an rf ion guide without applying actual rf voltage, which minimizes rf noise if it is coupled to Fourier transform-ion cyclotron resonance (FT-ICR) MS yet efficient ion transmission is maintained. Hence, PFIG as a drift tube for ESI-IMS can improve the analytical figures in terms of high transmission and high resolution minimizing ion loss by diffusion without aforementioned complications with a suitable interface. This study will discuss the preliminary results from the prototype ESI-IM-MS using modular PFIGs as a mobility cell to increase ion transmission and secure accurate/precise CCS measurements of gas-phase ions from chemical/biological molecules.

CHAPTER III

AN RF ION FUNNEL INTERFACE FOR PERIODIC-FOCUSING ION GUIDE-MASS SPECTROMETER

Introduction to an RF Ion Funnel

ESI is typically performed at atmospheric pressure and ions are delivered to the device under vacuum[20a, 20c]. It must therefore adapt differential pumping to maintain the low pressure required for a mobility cell (1~20 torr) and the mass spectrometer ($<10^{-5}$ torr) by conductance limiting apertures. Ion transmission is inherently decreased by this restriction so that the sensitivity of ESI-MS is always a challenge for instrumentation. To tackle the issue, there are two types of ion focusing mechanisms employed together - pneumatic focusing and electrostatic focusing. Pneumatic focusing utilizes directional gas flow by the pressure gradient. The gaseous plume of ions is entrained in the gas flow through a heated capillary or orifice to the first pumping stage at a pressure of 0.5 ~ 5 torr. Then ions expand in the jet stream by pressure drop until they reach the Mach disk where turbulence occurs. Electrostatic focusing is very difficult in this region for prompting ions to change their directional momentum or collimate the ions on the propagation axis owing to the gas dynamic effect. A skimmer is usually located before the location of the Mach disk to maintain quality of the ion stream and a fraction of the ions is then sampled through the skimmer to the next pumping stage of which the pressure range is roughly 10^{-2} ~ 10^{-5} torr. This multi-staged pneumatic flow involves inevitable loss of entrained ions by collision with neutral gas and limited aperture size.

To address the issue, an rf ion guide is used for the regions where the background gas pressure is relatively high (~10^{-2}torr). According to Douglas and French, ion kinetic energies are dampened and ion trajectories are confined near the center line of the quadrupole due to the collisions between ions and the neutral bath gas in the device[33]. By changing the shape from a quadrupole to multiple ring electrodes and applying a dc pulse to prevent the reduction of ion axial velocity, Giles and coworkers developed a TW ion guide compatible with a high efficiency ion guide and drift tube[13]. However, collisional focusing by an rf ion guide is only effective at lower pressures of 10^{-2}~1 torr and an ion focusing apparatus for high transmission is still required at the pressure range of 1~10 torr for matching the low pressure region to the DT pressure range.

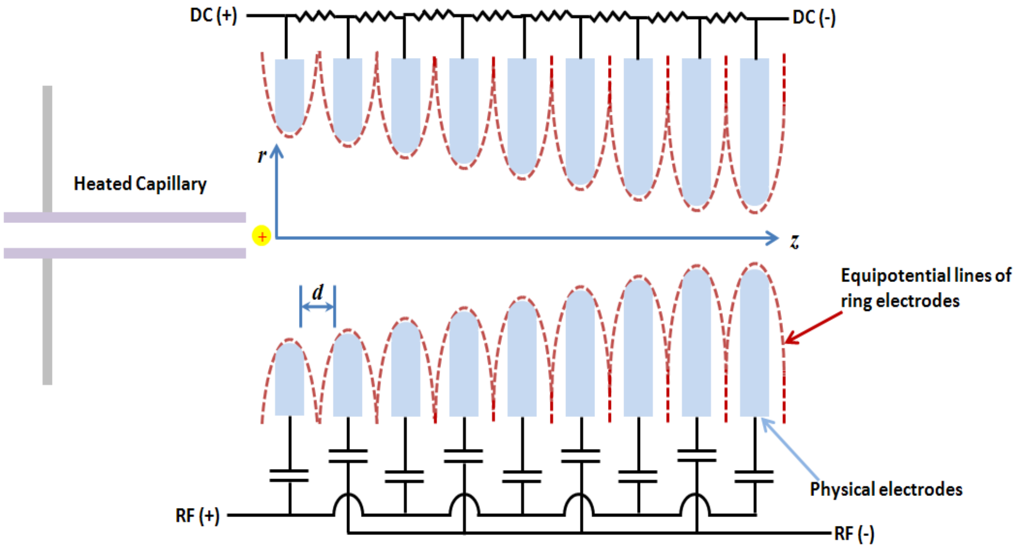

Figure 4. Schematic of an ion funnel with electrical diagram. When ions spread out from the heated capillary, the motion of ions is radially confined by rf field and the tapered inner diameter geometry. The dc and rf potentials are separated by capacitor chains which are connected to every other electrode.

The first rf ion funnel (IF) was invented by Shaffer *et al*. to address the problem. The prototype device utilizes the concept of gradual concentric confinement of ions[25, 34]. It consists of a heated capillary followed by a series of stacked ring electrodes with tapered center holes which focus ions to the exit aperture by both rf and dc potential as seen in Figure 4. The dc field developed by the voltage gradient across the resistor chain helps ions move toward the axial direction (z) and the rf field by the neighboring electrode having opposite phases restricts radial (r) motion of ions to the center axis of the device. The rf IF acts similarly to the stacked ring rf ion guide which is operated at a pressure lower than 0.1 torr. The concept of the device is well described by Dehmelt and reviewed by Gerlich[35]. The purpose of the tapered design is to minimize ion spread after Mach disk located close to the heated capillary by turbulence. Thus the dimensions of the rf IF are critical since the device has to be large enough to accommodate the jet stream from the heated capillary and accomplish optimal ion focusing. Since the fundamentals of the rf IF have been well established in the last decade, incorporation of the device into ESI IM-MS is an attractive choice[5b, 9, 36].

Characteristics of Gas Flow in a Heated Capillary

Since the heated capillary (HC) is accommodated in the rf IF interface, it is necessary to understand the fluid dynamics owing to the air flow passing through; to characterize the flow condition, some calculations are required using measured values. The heated capillary had 400 μm i. d. and 11.4 cm length. One end of the heated capillary was exposed to the atmospheric pressure and the other end was in the interface chamber. The measured chamber pressure and the HC temperature were 0.74 torr (mechanical pumping speed of 20 m^3/h at 760 torr N_2) and 70 ℃ respectively, as determined by a capacitance manometer and a resistance temperature detector. Hence the mean free path (λ) of the air can be estimated by from the equation below

$$\lambda = \frac{1}{\left(\sqrt{2}\sigma N\right)} = \frac{kT}{\left(\sqrt{2}\sigma P\right)} \approx 5.0 \times 10^{-7} m \tag{3.1}$$

where σ is the CCS of nitrogen and oxygen which is from the sum of the radius of N_2 1.1Å and O_2 0.96 Å[37]. The pressure inside of the heated capillary (*P*) is not the numerical average of the input and output side of the heated capillary [38] but for convenience, it is estimated to be 380 torr. Therefore, the Knudsen number (*K*), which specifies the type of gas flow can be deduced from the condition

$$K = \frac{\lambda}{d} \approx \frac{5.0 \times 10^{-7} m}{400 \times 10^{-6} m} = 1.2 \times 10^{-3} \tag{3.2}$$

where *d* is the diameter of the cylindrical tube. Since $K \ll 1$ holds for a viscous flow regime, we can apply fluid dynamics calculations for continuous viscous flow to the experimental condition. When $K \gg 1$, the mean free path is longer than the diameter of the cylindrical tube and the gas flow regime belongs to molecular flow of which gas molecules mostly interact with the wall.

To characterize the flow in a cylindrical geometry as one of the three viscous flow types, i. e., laminar, turbulent, and transition, we can derive the Reynolds number which gives the ratio of inertial force from the velocity of the fluid to the viscous force from the characteristic property of the fluid and describes which flow type corresponds to the HC flow. When the Reynolds number is less than 1, it is called Stoke’s flow. Laminar flow occurs at low Reynolds numbers with slow velocity of the fluid characterized by constant sliding motion on each layer without mixing in which the velocity of the fluid at the wall is nearly zero and maximum at the center of the tube. Turbulent flow occurs at high velocity of the fluid of which Reynolds number is approximately over 2040 and accompanies flow instabilities including chaotic eddies and vortices[39]. The transition from laminar flow to turbulent flow is sensitive to the flow geometry and the level of disturbance. The Reynolds number is calculated by the following equation to define the flow regime,

$$Re = \frac{\rho v d}{\mu} = \frac{vd}{\nu} \tag{3.3}$$

where ρ is the density of the fluid (kg m^{-3}), v is the velocity of the fluid based on the cross section of the cylinder (m/s), d is the diameter of the tube, μ is the dynamic viscosity of the fluid (Pa·s or N·s m^{-2} or kg m^{-1} s^{-1}) and ν is the kinematic viscosity ($\nu = \mu/\rho$, m^{2}s^{-1}). For air at 70 °C and 760 torr, ν is 1.97×10^{-5} m^{2}s^{-1} and μ is 2.03×10^{-5} N·s m^{-2} [37]. To figure out the velocity of the air in the Reynolds number calculation, it is required to estimate the rate of volume flow of the air across the heated capillary. The cross-section of the capillary is $1.2 \times 10^{-7} m^2$ and the air flow can be considered as a viscous flow since the mean free path is much smaller than the tube diameter as calculated previously. Note that Hagen-Poiseuille’s law can be applicable for obtaining the velocity of a steady viscous laminar flow through a long cylindrical tube of which length is larger than 20 times the diameter of the tube. The gas flow rate (Q) is proportional to the pressure drop at the ends of the tube ($P_1 - P_2$) and the fourth power of the tube radius (r).

It is also inversely proportional to the length of the tube (L) and the viscosity of the gas (μ)[40].

$$Q = \frac{\pi r^4}{8\mu L}(P_1 - P_2) = 2.7 \times 10^{-5}\mathrm{m}^3\mathrm{s}^{-1} \tag{3.4}$$

Since the cross section of the tube is$1.2 \times 10^{-7} m^2$, the velocity of the air can be calculated by

$$v = \frac{2.7 \times 10^{-5}\mathrm{m}^3\mathrm{s}^{-1}}{1.2 \times 10^{-7} m^2} = 2.3 \times 10^2 m\ \mathrm{s}^{-1} \tag{3.5}$$

In another approach, we can use the pumping capacity and measured pressure values for calculating the gas throughput and conductance. The pressure at the atmospheric entrance region of the HC is close to 760 torr. However, when the fluid passes and reaches to the end of the tube, the pressure inside of the tube is changed by the viscosity of the air and the inner wall resistance from the mass flow of the air. Therefore, the pressure of the fluid past the capillary has a reverse sigmoid curve and the intake pressure value (P_1) from the equation should consider the pressure curve by the effect[41]. To identify the variation of the inlet pressure, we can use the equation for calculating the size of a thin aperture ($L \ll d$) in the viscous gas flow regime[42],

$$A = \frac{C}{20} \tag{3.6}$$

where A is the cross section (cm^2) of the aperture and C is its conductance (liter/s). Since we already know the pressure after the HC and the cross section, we can use 760 torr for the pressure in front of the aperture so that the equation (3.6) gives the value of the required aperture size to maintain the pressure of 0.74 torr, which leads us to reversely compare the value with the actual cross section of the heated capillary. Since the pressure drop occurs only by a mechanical pump connected to the effective pumping speed of 20 m^3/h, the calculation for gas throughput Q is

$$Q = SP = 4.1 \times 10^{-3} m^3 s^{-1} torr \tag{3.7}$$

and the conductance can be calculated by

$$C = \frac{Q}{P_1 - P_2} = 5.4 \times 10^{-3}\ liter\ s^{-1} \tag{3.8}$$

where $P_1 - P_2$ is the pressure drop across the heated capillary[42]. Hence the calculated aperture size (A) is

$$A = \frac{5.4 \times 10^{-3}}{20} = 2.7 \times 10^{-8}\ m^2 \tag{3.9}$$

Compared to the actual value of $1.2 \times 10^{-7} m^2$, the result is about four times smaller and if we take 25 % of the atmospheric pressure as the inlet pressure for the calculation, then the conductance C under the conditions of the experiment is

$$C = \frac{Q}{P_1 - P_2} \approx 2.2 \times 10^{-5} m^3 s^{-1} \tag{3.10}$$

The velocity of the air passing through the capillary is then calculated by

$$v = \frac{2.2 \times 10^{-5} m^3 s^{-1}}{1.2 \times 10^{-7} m^2} = 1.8 \times 10^2 m\ s^{-1} \tag{3.11}$$

At first glance, the number is smaller than the result of the Hagen-Poiseuille's law (2.3×10^2 m s^{-1}). The reason is that the uncertainty of the inlet pressure of the tube and the effect of the length of the tube are not considered in this calculation. However, the result from the Hagen-Poiseuille's law is based on the assumption that the flow is a viscous laminar flow whereas the result above uses only the viscous gas assumption at the beginning of the discussion. Therefore, the calculation can give an idea of the range of the velocity passing through the tube. By considering both pumping speed of viscous flow and Hagen-Poiseuille flow, the velocity of the air flow can be estimated to be ~$2.1 \times 10^2 m\ \mathrm{s}^{-1}$. The density of air inside the HC is also changed by variation of the pressure. If we calculate the kinematic viscosity by considering the air as an ideal gas, we now have the velocity of air, and we can determine Reynolds number.

$$Re = \frac{\rho v d}{\mu} = \frac{v d}{\nu} \approx 4.3 \times 10^3 \tag{3.12}$$

The calculated value indicates that the flow regime in the HC under the conditions of the experiment is turbulent flow. However, the results might be applicable to the end of the HC at the low pressure side since the inside pressure follows the reverse sigmoid curve and the velocities from Hagen-Poiseuille's law and the aperture size calculation are close. By the simulation of a cylindrical tube using computational fluid dynamics (CFD), the axial velocity reaches a plateau in the middle of the tube with mass flow resistance and viscosity and the velocity of the escaping fluid from the end of the HC is faster than from the middle of the tube[41b] .

To estimate the actual velocity distribution, we can adopt techniques from rarefied gas dynamics. This technique has played a crucial role to address molecular phenomena including molecular reaction, isentropic cooling and condensation by acceleration of sample gas from a pressurized cell through vacuum system harvesting ions by skimmer in mass spectrometry[43]. One of the methods to observe the velocity distributions from the nozzle beam is to measure the flight time of ions/particles by chopping the beam with a rotating slotted disk[44]. The time density pattern from the segments of the beam was detected at the downstream by an ionization gauge. In the case of Ar at 300 K with 0.33 mm nozzle i. d. at 200 torr to high vacuum (~10^{-5} torr), the most probable velocity was ∼560 m/s[45]. In addition, CFD shows a velocity range of 0 to 720 m/s for the expanding gas flow through a 0.25 mm i. d. orifice from atmospheric pressure to 1-3 torr vacuum[46]. These results support the air flow velocity obtained from the calculation discussed so far.

The imposed pressure difference across the HC accelerates the air toward the exit at a speed comparable to the speed of sound as seen previously. Propagation of the air results in a pressure disturbance and the speed of propagation of the disturbance depends on the thermal molecular velocity affected by the molecular weight and specific heat capacities of the air. When the air speed reaches the speed of sound (340 m/s) or above, the disturbance approaches a fixed position of surroundings at the sum of the speed of sound and the speed of the flow. No propagation of the disturbance exists at the front of the fluid, which means that it reaches all directions with different velocities[47]. For example, if we think of a spherical wave propagation at rest and move the center of the sphere at different time following the direction of the fluid motion, then the upstream would have small wave spheres and the downstream gradually would have large wave spheres since the propagation of the wave has the same speed, the speed of sound. Almost all gases, including air, experience significant variations of density during the propagation and the acceleration of a flow in a gas can be treated as a compressible flow model. While the sonic speed from a nozzle is easily achievable in gases at a pressure ratio of as low as 2:1, in the case of liquids, extreme pressure as high as 1000 atm is required[48]. When the flow velocity is close to the speed of sound, the flow starts compressing the air ahead of the flow and increasing the local density of the air accompanied by substantial changes of temperature and pressure in the region. The compressibility depends on the speed of flow and can be determined by the Mach number (M) which is the ratio of the flow speed to the speed of sound in the medium, in this case, the air. At the subsonic to sonic speed (M≃1), the change in the density linearly increases and if the flow reaches supersonic speed (M>1), the density change is proportional to the square of M. Characteristic properties of a compressible flow are shock waves (acoustic wave) and choked flow. To explain the behavior of compressible gas at subsonic or sonic speed, it can be considered as an adiabatic expansion owing to no heat exchange with the surroundings in an extremely short time and with negligible entropy increase; the phenomenon can be treated as an adiabatic reversible expansion. The thermodynamic expression for the isentropic process is[47],

$$S_2 - S_1 = C_p \ln\frac{T_2}{T_1} - R\ln\frac{P_2}{P_1} = C_v \ln\frac{T_2}{T_1} - R\ln\frac{\rho_2}{\rho_1} = 0$$

$$\frac{P_2}{P_1} = \left(\frac{T_2}{T_1}\right)^{\frac{k}{(k-1)}} = \left(\frac{\rho_2}{\rho_1}\right)^{k} \tag{3.13}$$

where S is the entropy, C_p is the specific heat capacity at constant pressure, and C_v is the specific heat capacity at constant volume. The subscripts 1 and 2 refer to the initial and final states, respectively and k is the specific heat ratio (= C_p/C_v). In case of air, k is 1.4 and the sonic speed (M=1) can be achieved at the nozzle exit, given that the ratio of the stagnant pressure (the pressure inside the HC, P_1) to the background pressure (the pressure after the HC, P_2) is smaller than 2.1 from the equation[49]

$$\frac{P_2}{P_1} = \left(\frac{k+1}{2}\right)^{\frac{k}{k-1}} \tag{3.14}$$

Also, the temperature of gas flow is changed since the expansion is isentropic and by replacing the values taken from the previous discussion,

$$\frac{0.74\ torr}{190\ torr} = \left(\frac{T_2}{343\ \mathrm{K}}\right)^{3.5}$$

$$T_2 = 71\ \mathrm{K} \tag{3.15}$$

Therefore, the temperature of the flow is much lower than that of the stagnant flow inside the HC. However, the stagnant pressure is higher than the background pressure after the HC and the flow is under-expanded, which results in subsequent expansion in the zone of silence where the isentropic expansion process occurs (Figure 5). Since the flow moves faster than the speed of sound which means that boundary conditions propagate slower than the speed of the flow, the Mach disk and the barrel shock are developed by overexpansion of the flow. These shocks, which have the thickness of the mean free path of gas molecules at the background pressure, recompress the flow and a non-isentropic process including large density, pressure, temperature, and velocity gradient occurs subsequently. The location of the Mach disk can be determined by the nozzle diameter and the ratio of the initial pressure to the final pressure[49] from the equation

$$\frac{x_m}{d} = 0.67\left(\frac{P_1}{P_2}\right)^{\frac{1}{2}} \tag{3.16}$$

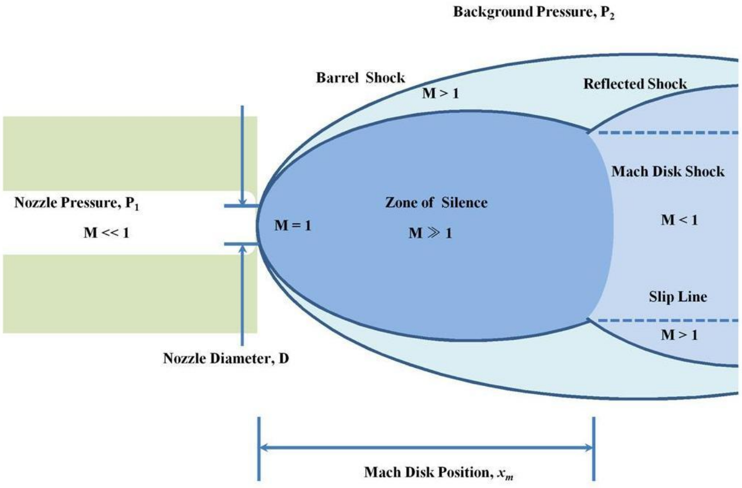

Figure 5. Jet expansion from high pressure to low pressure. In general, a sampling skimmer cone is located in the zone of silence to minimize turbulence effect by the Mach disk shock. The Mach disk position depends on the ratio of the stagnant nozzle pressure to the background pressure.

As an example, for a pressure drop from 760 torr to 1 torr across the HC, the Mach disk is expected to be 7 mm away from the end of the capillary. A case of higher background pressure involves weak shock structures. However, even in weak shocks, the collisions in the shock region are detrimental to ions which travel with the mixed air flow and the skimmer must be positioned before the Mach disk. The intensity of the molecular beam or ion stream can be increased by using a skimmer with a wide i. d., although this approach is limited by the available pumping capacity of the next stage. ESI includes all the processes discussed to deliver ions from atmospheric pressure to a detector device *in vacuo* and to achieve this goal, differential pumping is essential. The rf IF is expected to accommodate more ions and address the disadvantages of gas dynamics effect during the process.

Experimental

Homebuilt ESI Source and Rf Ion Funnel

The homebuilt ESI source was mounted on an x-y-z and rotational stage holding a Macor® plate for electric insulation from a pulled capillary tip (330 μm o. d. with 50 μm i. d.). The spray potential ~5 kV was applied to a stainless steel union which accommodated the tip. The HC inlet (Thermo, Catalog Number 70005-98041) was located in front of an in-house rf IF interface through a bellows mount. The angle of the heated capillary was adjustable to the rf IF acceptance area to reduce the directional neutral jet flow to the next stage. Since other rf IFs were fabricated with various custom-made materials and dimensions including a printed circuit board for all-in-one type[25, 34], the in-house rf IF, referred to the original design, was assembled by commercially available ion optic part s (eV parts®, Kimball Physics) for convenience and machined for variation of i. d. size. Each stainless steel electrode had a 35.5 mm × 35.5 mm square shape with 0.67 mm thickness. The first 15 electrodes of the IF had identical i. d. of 25.4 mm while the remaining 18 electrodes had progressively decreasing i. d. from 25.4 to 2.0 mm. The last electrode using dc only (2.0 mm i. d.) worked as a conductance limit and was sealed by an O-ring to a polyether ether ketone (PEEK) enclosure. The electrodes were stacked together using ceramic spacers with identical thickness; the total length was 48.5 mm. The angle of half of the tapered region was 22°. Four ceramic rods penetrated each corner of the assembly to provide physical support. Capacitors (NP0, 100pF, 1kV, Mouser Electronics) and resistors (metal thin film resistor, 11MΩ, ± 5%, Mouser Electronics) were silversoldered to each electrode through 4mm long nickelcoated copper wires which were press-fitted to notches (0.5 mm × 2.0 mm) at the electrode edges.

SIMION Ion Trajectory Calculations

To obtain estimated operational conditions of the in-house rf IF, an ion trajectory calculation was performed by SIMION 8.0[28] using C_{60} (+·) ion as a model ion and N_2 pressure at 0.1~5.0 torr with a modified user program coded by Lua language[50]. All calculations were based on the hard sphere collision model provided by the SIMION 8.0 program package and 1.24×10^{-18} m^2 was used for the CCS of the model ion C_{60} (+·)[51]. Unfortunately, this version of the program was not able to simulate space charge effect. Thus the result might not represent the definitive effect for the case of a tightly focused ion stream in a narrow region. However, the level of charge density which leads to space charge effect is expected to be hardly achieved by a continuous ion source like ESI owing to a flow subsequently wiping out ions inside of the rf IF.

Coupling to a Commercial Instrument

Based on the simulation results, operational parameters were fine-tuned and the focusing performance was tested by mounting the device to a QSTAR® Qq-TOF (AB Sciex, CA) using two solutions which contained 15 μM bradykynin 1-8 (MW 903.5, Sigma-Aldrich, MO) and 30 μM ALILTLVS (MW 829.5, Bachem, CA) with 50 μM CsI (MW 251.8, Sigma-Aldrich, MO) used for calibration of the commercial instrument. All sample solutions were prepared using water: methanol: acetic acid (49.5: 49.5: 1.0, vol. %) solvent mixture to the concentrations. The ion current was measured with a 610C electrometer (Keithley, CA). The test setup for fine-tuning the device at actual conditions is shown in Figure 6. One of the methods for examining ion focusing devices is the measurement of ion current using an electrometer[34g]. The front of the rf IF was capped off by a blank square electrode which was electrically separated from the rest of the IF and connected to the electrometer when the ion current was directly measured right after the heated capillary. The homemade ESI source replaced the instrument Turbospray® source. The flow rate was 2.0 μl/min from the instrument syringe pump. Collisional focusing Q0 was separated by a skimmer (i. d. 2.0 mm) from the rf IF which is not shown in Figure 6 for clarity.

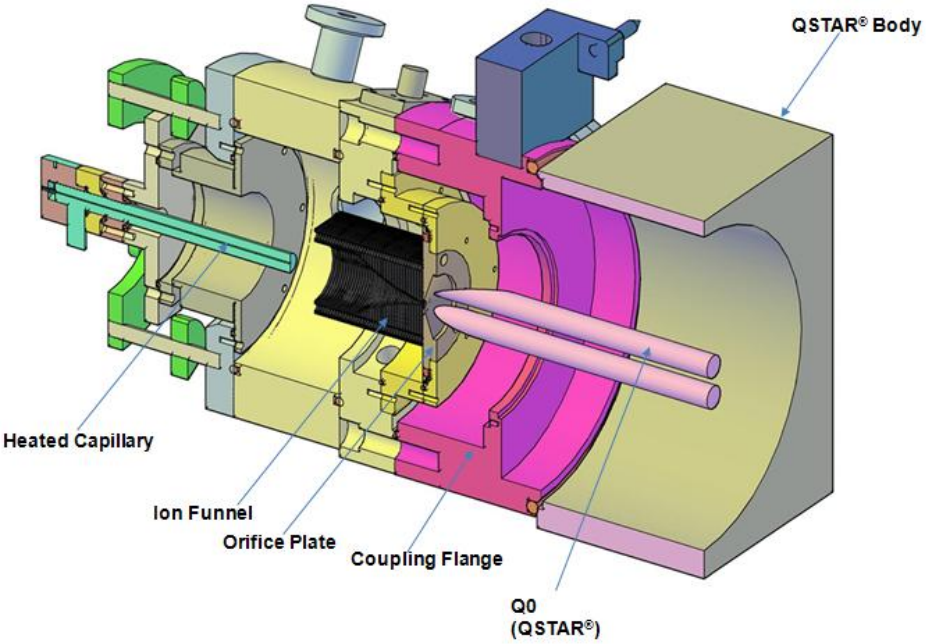

Figure 6. Rf IF test setup in front of ABSciex QSTAR® Qq-TOF. Collisional focusing quadrupole ion guide (Q0) followed the IF exit electrode and additional pumping assisted to keep the pressure in Q0 lower than 10 mtorr. The incidence angle was adjusted by the knobs (green) on the treaded guides supporting the HC surrounded by the bellows. The ion current was measured at the orifice plate (i. d. 2.0 mm).

Results and Discussion

According to the cross-cut of the calculation result in Figure 7, as the i. d. of the stacked ring electrodes is decreased, collisions induced by oscillating rf fields near the inner rim of the ring electrodes dampened ion motions along the centerline as similar to a segmented rf ion guide[52].

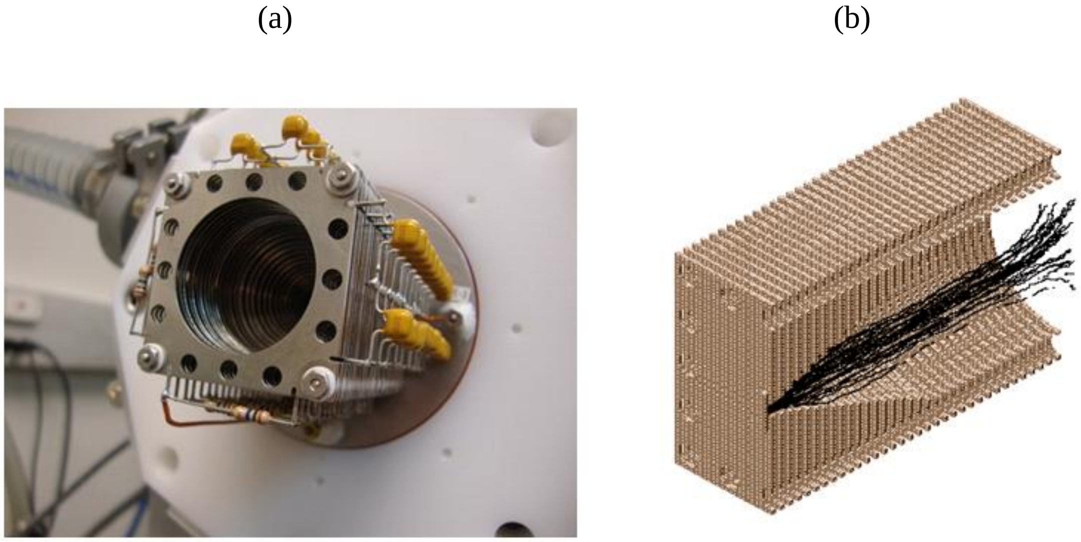

Figure 7. (a) Photograph of the assembled rf IF and (b) ion trajectory calculation of C_{60} (+·) ion at 1.0 torr N_2 with 100 V_{pp} rf and 15 V/cm dc gradient across the rf IF.

Also, it was found that adjustment of the number of electrodes was necessary at the end of the tapered region from the initial design to avoid unnecessary ion trapping at the rf IF exit by the effective potential well as shown in Figure 8. The two electrodes before the exit electrode had the same inner diameter of 2.0 mm and the long narrow passage near the exit worked as a trapping zone at lower dc field to block ion propagation. This could mean that the weak dc field is not able to provide enough kinetic energy to pull out ions in the pocket produced by effective potential surface[35b]. Since the last exit aperture worked as a conductance limit to the next stage, a larger aperture size was anticipated to benefit ion transmission if the pumping speed and design of ion-guiding electrodes allowed it. The last dc only electrode can also operate as a gating electrode by applying a dc potential to block or pass ions exiting the IF. Therefore, the number of electrodes in the tapered region was changed to 33 by the simulation to decrease the long narrow exiting zone and the final version had 2.0 mm exit aperture.

(a)

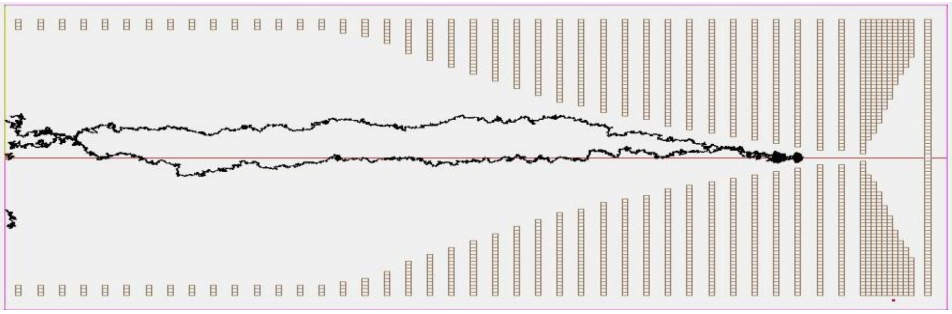

(b)

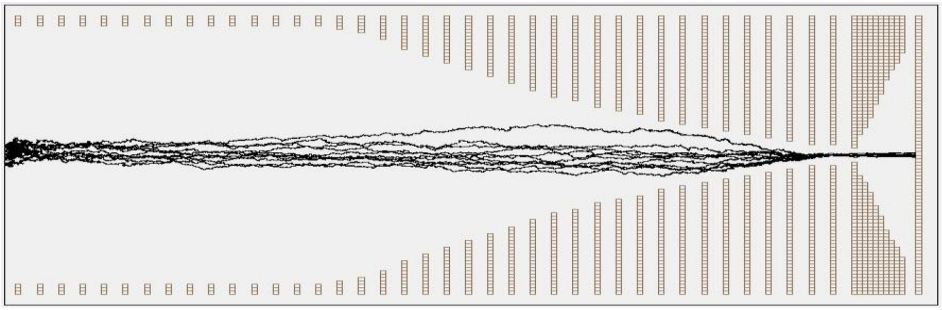

Figure 8. (a) Ion trajectory calculation showing trapped ions near the exit of the IF at the dc field 8V/cm across the IF and (b) 90% transmission at the condition of the dc field 14V/cm. Both conditions have the same rf 50 V_{pp} at 500 kHz with the pressure 1.0 torr N_2 and the exit aperture i. d. of 1.5 mm.

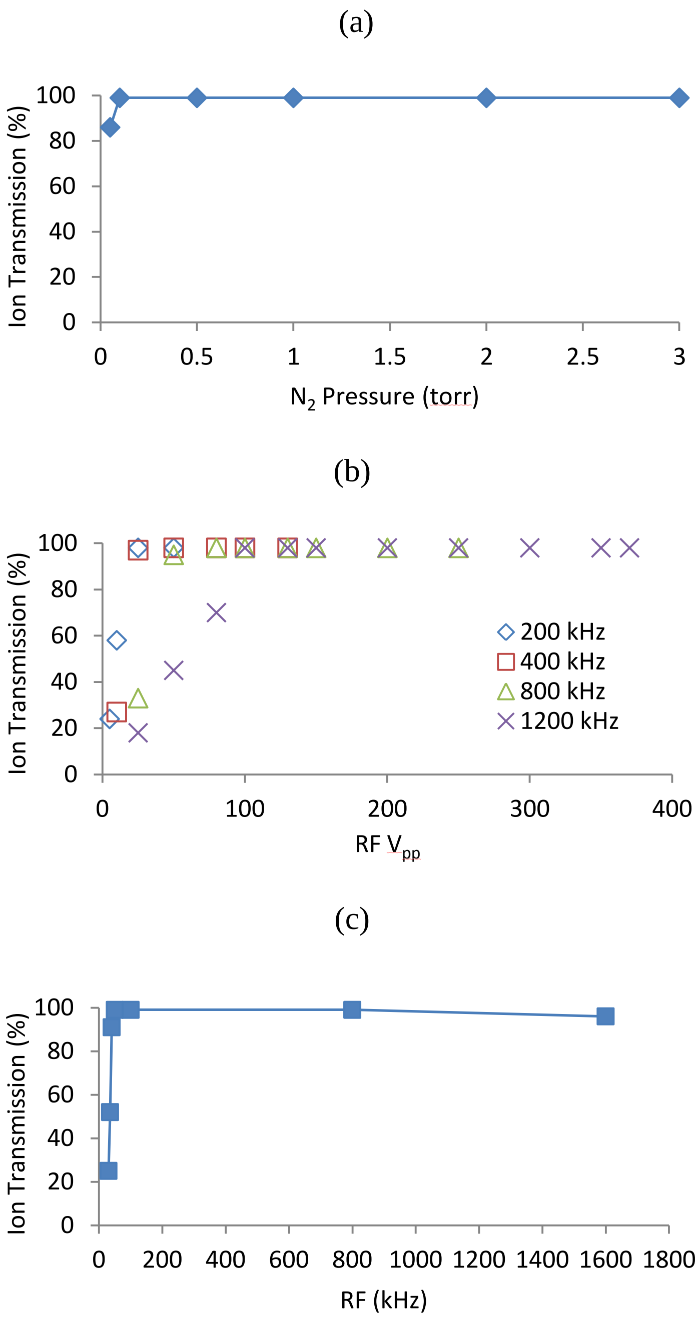

Figure 9. Ion transmission of the in-house rf IF from ion trajectory calculations at various conditions; (a) static N_2 pressure changes at dc field 15 V/cm and rf 100 V_{pp} with 800 kHz, (b) various rf amplitudes of 800 kHz at N_2 pressure 1.0 torr with the same dc field, and (c) the range of effective rf frequency at N_2 pressure 1.0 torr and rf 100 V_{pp}.

Although gas dynamics was not considered and static pressure was applied to the region during the ion trajectory calculations, the operational conditions from the calculation results matched well with the experimental data reported by other groups[34g]. For example, the model design showed high transmission over 90% in the various simulated conditions described in Figure 9 at the rf amplitude of 50~200 V_{pp} and 800~1200 kHz under the pressure of 0.5~3 torr N_2. The calculation data over 3 torr is not shown here since the collision frequency increased and the trajectory calculation after every collision slowed down extremely at the same voltages and parameters. At lower than 0.2 torr, the mean free path was long and the directional momentum gain by electric field was too large to be deflected by collision between ions and gas molecules with the oscillating rf field around the ring electrode. Since the effective potential of an rf focusing device is proportional to the square of the rf amplitude and inversely proportional to the square of the rf frequency, the focusing effect decreases as the rf frequency increases at the same amplitude. It also depends on the mass and the charge state of the ions, which can result in ion discrimination inside the rf IF[34d]. Therefore, these factors should be considered when determining the parameters to operate the rf IF to optimize the ion transmission and minimize the adverse effects.

The rf IF is intended for tight ion confinement from its geometric advantages and application of rf. However, the HC generates a directional jet flow across the region and the introduced fast gas stream disrupts the vacuum pressure of the next stage if it is aimed straight to the IF exit. In addition, accompanying neutral solvent clusters and charged cluster ions can reduce the signal-to-noise ratio if they enter into the mass analyzer section. A jet disrupter can address the problem[53]. However, it needs to have another independent control channel for the potential applied and this would increase the complicacy of the rf IF structure. Instead of using the jet disrupter, the adjustable bellows system holding the heated capillary inlet flange was adapted at the interface. By transition of the incident angle to the center axis of the rf IF, the ion current was changed as shown in Figure 10 (a). Since the stacked ring electrode structure had a void among the electrodes through which neutral molecules and light ions could escape, it would enhance the ion current of heavier ions. But large incident angles (>10°) could harm the focusing owing to the large momentum change required for the directional motion of heavy ions entrained by gas flow. The gas loading is affected by the HC temperature. An entering unit volume of gas is expanded upon thermal equilibrium with the HC wall. The increased temperature results in internal resistance and reduction of the flow rate and number of ions entrained in the flow. This effect was identified by the ion current change after the HC in Figure 10 (b). On the other hand, low HC temperature induces less desolvation and evaporation which are essential to generate more ions from ESI droplets and this leads to low ionization efficiency. The effect of dc and rf was also tested and the dc voltage drop associated with rf shows increased ion current as shown in Figure 10 (c). The directional gas flow is anticipated to be dominant since the rf without dc still shows the high ion current. The variation of the actual rf amplitude was measured after insertion of the same capacitor used in the IF as an inline capacitor. Since the dual channel self-oscillating rf power supply (Ardara Technologies PS-6901C) responds to the total capacitive load in the IF circuit and the frequency is inversely proportional to the square root of the total capacitance, the additional capacitor can adjust the operating

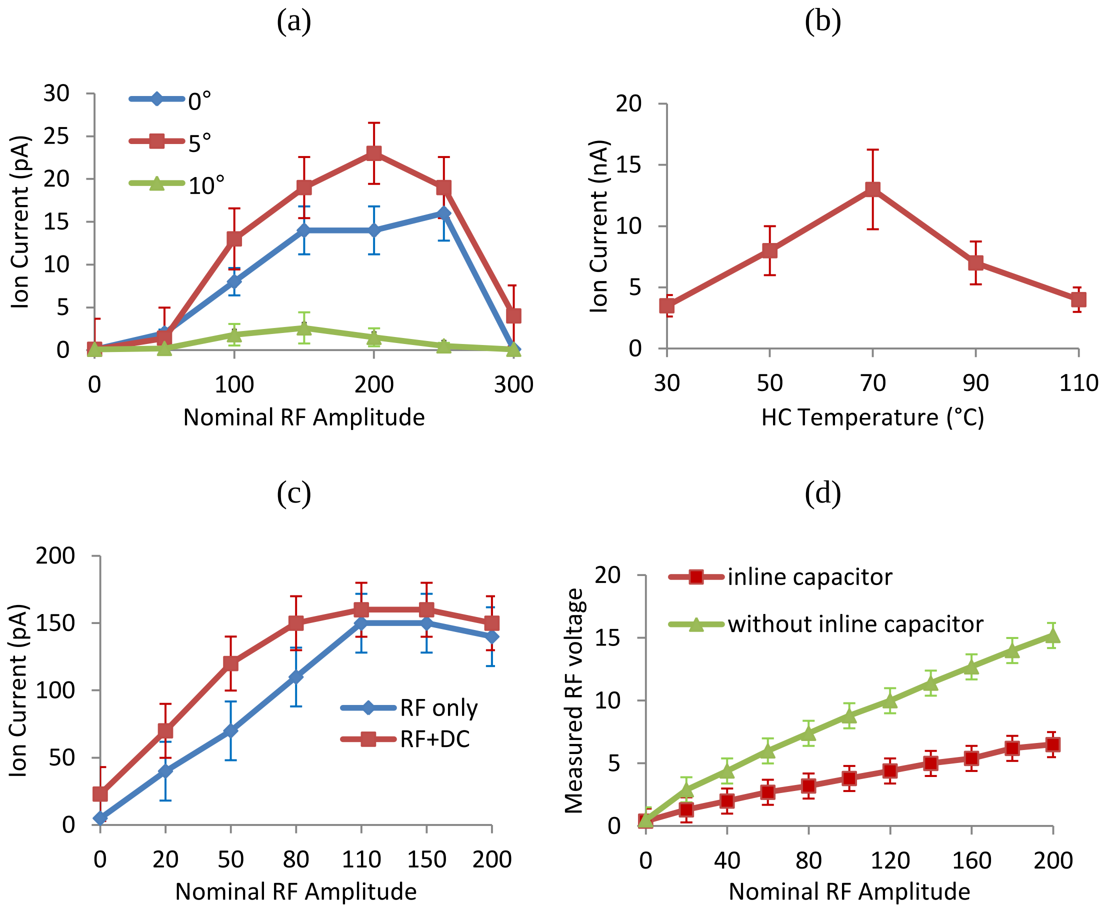

Figure 10. (a) Ion current variation to different incidence angles between the HC and the IF central axis at 95 ℃ of the HC (b) ion current as the HC temperature changes measured at 5 mm away from the end of the HC (c) dc and rf effect on ion focusing at 70℃ of the HC (d) measured rf amplitude at the orifice plate with the addition of the inline capacitor. The total capacitance was 500 pF and 1000 pF with and without inline capacitor, respectively. The sample solution was 15 μM bradykinin 1-8 in water: methanol: acetic acid (49.5: 49.5: 1.0, vol. %) solvent at 5.0 kV ESI voltage with 2.0μl/min flow rate from (a) to (c).

frequency and the amplitude accordingly. In rf electronics, addition of capacitance works as increase of resistance and this effect was identified by measuring the actual amplitude from the orifice plate using an oscilloscope in Figure 10 (d).

When the effective amplitude is high, it is anticipated that equipotential wells near the exit region can trap ions from SIMION results and ion transmission decreases.

(a)

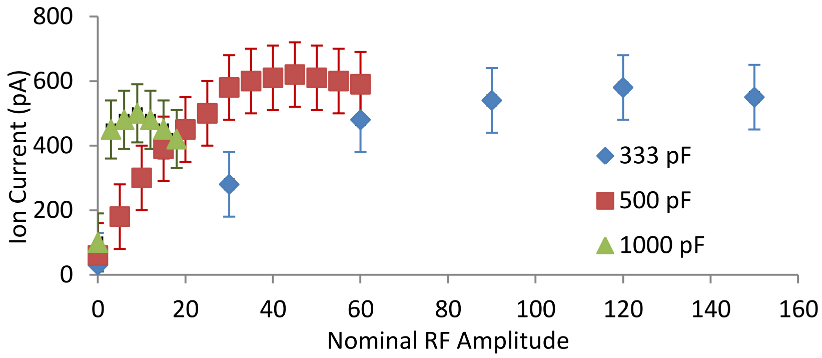

(b)

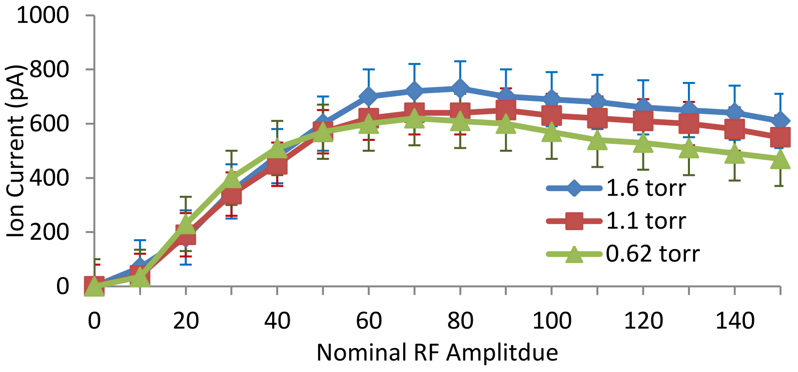

Figure 11. (a) Effect of the capacitive load in the IF at 1.1 torr and (b) ion transmission as the pressure changes at 500 pF of the total capacitance. The pressure was controlled by closing the butterfly inlet valves at mechanical pumps. 15 μM bradykinin 1-8 was electrosprayed for the measurement.

The trapping effect can be explained by the curved ion transmission at different total capacitive loads as the rf amplitude increases (Figure 11 (a)). In the case of 1000 pF, ion current gain is in a narrow range of the amplitude which makes it difficult to set the nominal rf amplitude for operation. As the total capacitance decreases from 1000 to 333 pF, the measured rf amplitude gets lower and the depth of the effective potential well decreases, which allows more ion current[34d]. In Figure 11 (b), the plot exhibits the relationship of the ion transmission and the IF pressure at 500 pF of the capacitive load. For the same reason, when the amplitude is high, the last few electrodes having narrow i. d. develop equipotential wells in-between at different pressures. It might have pneumatic advantages since the small ion current increases are observed in the plot when the pressure increases, although the overall ion transmission is not changed severely. The data shows acceptable ion current in the working ranges proposed from the ion trajectory calculations in Figure 9.

The measured ion current is close to 3~13 nA right after the HC and 0.5 ~ 0.7 nA at the IF exit, presenting 3~30 % ion transmission which is lower than the over 60% transmission claimed in other results[34c]. However, the ion current at the rf IF exit is close to the values from similar experiments[34b]. Therefore, it is assumed that the evaporation of solvent molecules from ESI droplets would not be sufficient to produce more ions in the given condition, and protonated solvent clusters would take a large portion of the ion current right after the HC. When drifted to the IF, the Mach disk shock and collision might heat up the ionized clusters and dissociation could occur. Owing to lower mass to charge ratio upon dissociation, the ions would be susceptible to turbulence and neutralized by collision into the electrodes. In the case of the peptide ions, the relatively large mass could help the ions to move forward since their moment of inertia would be greater than small cluster ions. Actual mass spectra were obtained using the calibrant

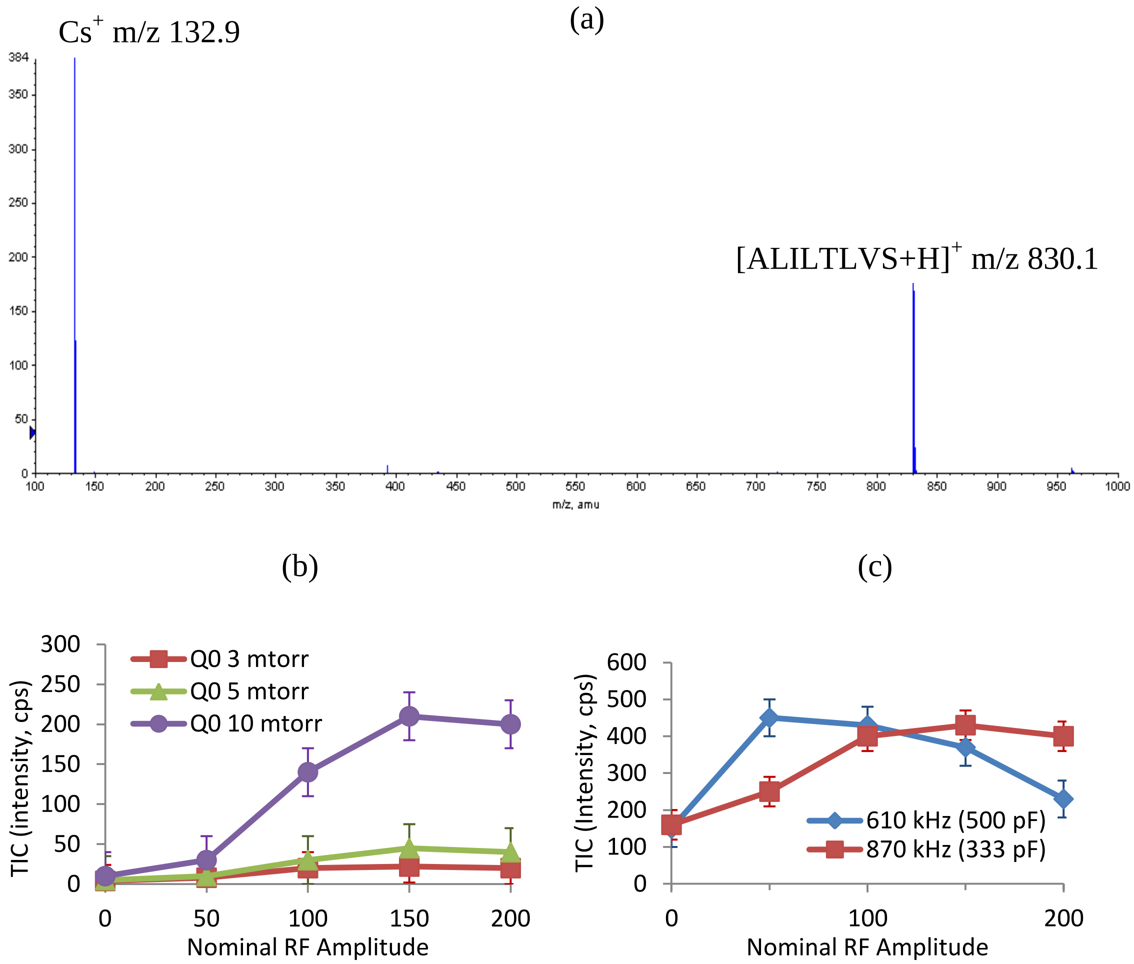

Figure 12. (a) Mass spectrum using the rf IF interfaced QqTOF with the calibration solution at 1.1 torr in the IF and Q0 10 mtorr with capacitive load of 333 pF at nominal rf amplitude 150 (b) total ion current (TIC) by the sum of two dominant peaks in mass spectrum at different Q0 pressure (c) TIC response with change of capacitive load in the IF circuit. The pressure in Q0 was controlled by adjusting a butterfly valve attached to the region.

solution containing CsI and synthetic peptide ALILTLVS through the IF interface in Figure 12. Peptide fragment ions and cluster ions were not observed. Since Q0 is designed for collisional ion cooling and focusing by rf only[33], it requires a minimum pressure to keep ions focused but it is not effective at less than 5 mtorr. However, Q0 pressure over 15 mtorr heated up the turbo-molecular pump in the region, which limited the pressure increase. The TIC responded to connection of the inline capacitor as anticipated from the ion current measurement.

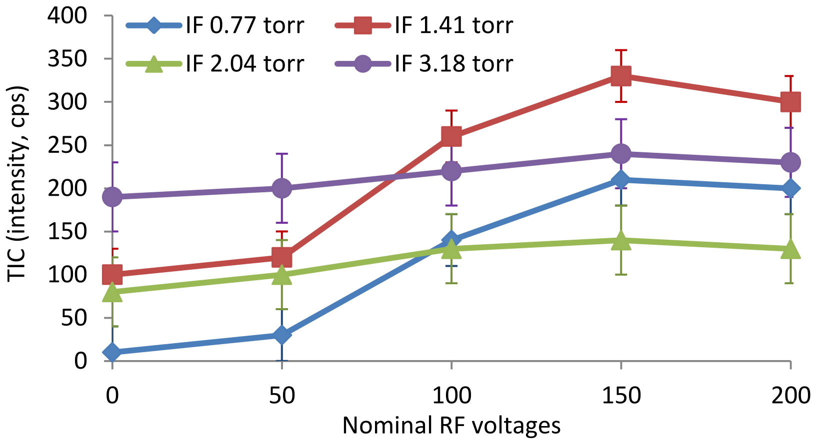

Figure 13. TIC for the variation of the rf IF pressure. The focusing by the rf IF was dampened by gas dynamics when the IF pressure was over 2.0 torr.

As shown in Figure 13, the ion transmission depends on the pressure inside of the rf IF as well. At over 2.0 torr, the overwhelming pneumatic flow pushes ions to the Q0 region regardless to the rf amplitude and the number of ions passing through is proportional to the pressure. At the increased pressure, the effective potential from the rf amplitude would not be large enough to change the linear momentum of the ions. The extended gas load to the Q0 is also detrimental in collisional focusing. Based on the result, the ion optics after the rf IF should be considered carefully by gas dynamics and at the effective working pressure range to maximize the benefit. The initial report by Shaffer *et al.* used a hexapole ion guide as a connective guiding device to a mass spectrometer. This would be an ideal choice for the interfacial pressure drop from 0.1 torr to 10^{-4} torr [25]. The length of the ion guide should be determined by consideration of under/overexpansion of the gas flow at the entrance. The ion acceptance area of rf multipole guides is closely related to transport efficiency and the initial kinetic energy of the ions should not be large enough to escape the pseudo-potential confinement. Electrostatic focusing including an einzel lens system would not be effective to minimize ion loss owing to the gas expansion plume and dominant collisions between ions and neutral gas molecules in this region.

Conclusions

The in-house rf IF was characterized by SIMION on trajectory calculations and various parameters including the HC temperature, gas pressure, and the capacitive load in front of the commercial instrument. The crucial factors are pseudo-potential barriers formed by the imposed rf potential and geometric features of gradually decreasing ring electrodes.

The utilization of the rf IF as an interface for delivering ions has a broad spectrum. According to specific instrument needs, it can be an interface for a continuous ion transporter minimizing radial diffusion of ions[36b] and an ion separator by adapting an extended narrow channel at the exit with ramping barrier voltage (selected-ion accumulation ion mobility spectrometer , SAIMS)[54]. The most benefited area is IM-MS which has suffered from intrinsic low ion transmission. Applications have shown promising results[36a]. A hermit seal with Teflon sheets between the electrodes can show enhanced ion focusing by taking advantage of pneumatic confinement although the strong jet stream should be overcome by jet disrupter[34c]. Consecutive addition of another IF can provide a trapping and dynamic pulsing region to enhance the overall transmission efficiency.

CHAPTER IV

INSTRUMENTATION OF ELECTROSPRAY IONIZATION PERIODIC-FOCUSING ION GUIDE-MASS SPECTROMETER

Interfacing Ion Source to Drift Tube

Since an intrinsic pulsed ionization including MALDI does not require additional gating of ion swarm before the DT and for the reason that the technique generates ions under vacuum, the implementation of IM-MS with pulsed ion sources may be the first pick[2a, 4c, 55]. However, consideration of the free ride effect and contamination of drift gas by intruding external gas species suggests that the pressure before and after the DT should be kept lower than that of the DT using, in most cases, ultra high purity helium (99.999%). When an IM-MS is built upon an atmospheric pressure ionization (API) source and high pressure DT, ion introduction to MS may simply follow the direction of the gas flow. Tang *et al.* developed this type of IM instrument having ESI source and atmospheric pressure (AP) IM, with mobility pressure ~700 torr air[56]. The connection to the mass spectrometer was a flared inlet capillary receiving ions from the end of AP DT and transferring ions to the MS region. Even though air itself is a mixture of gases, separation of different conformations is achievable and can simplify instrument design. Installment of the DT between vacuum devices (or pumping regions) for API sources, however, can change the game in every detail. In particular, the ion introduction region to the DT, which can be called as an interfacial pressure regime includes complicated gas dynamics and faces two strong flows coming from both sides and colliding into each other. To overcome the adverse flow effect and succeed in delivering ions to the DT, we needs careful adjustments of the gating potential and effective ion focusing devices. Besides, IM requires rigorous gating in the case of a continuous ionization source including ESI, which leads us to come up with advanced ion injection techniques.

The high transmission rf IF technique with its thorough investigation from the Dick Smith group has been urging experimental instrumentation to move forward by adapting and combining established technologies[34g]. The approaches have been gaining momentum by pioneering studies from several groups and various fields[36b, 57]. So far, most of beneficiaries are IM-MS and related area since it has been disadvantaged by intrinsic low duty cycle and ion loss through IM interfaces. For instance, the number of ions reaching to space charge limit, assumingly $\simeq 10^5$ ions /cm^3, starts at the gate before the DT. The gating normally operates at the rate of 50~500 Hz depending on the DT length and the gate pulse width is about 20~200 μs which means less than 2 % of ions are utilized. Moreover, when the ions are detected by TOF MS having extraction frequency of 40 kHz with 1μs pulse width, it aggravates the loss further down to 0.04% which corresponds to only 20 ions out of 10^5. To address this issue, two different approaches have been developed: (1) trapping ions to maximize the number of ions before they enter to the DT, and (2) multiplexing ion gating by Fourier transform (FT).

Ion trapping has been tried by several groups using an ion trap in front of the DT and an hourglass IF consisting of a consecutive or back-to-back two funnel type geometry, where the second funnel works as an accumulation/injection device[36a, 58]. However, technical difficulties owing to accurate voltage setup for extracting ions from the ion trap and pressure control ($10^{-2} \sim 10^{-3}$ torr) against high pressure drift tube (1~10 torr) were beyond consideration. Depending on injection voltage and trapping time, the drift time profile could also be changed severely owing to collisional heating[58b]. Lower efficiency of ion trapping/accumulation in the hourglass ion funnel is also expected since the pulsing stagnant ions facing counter-flow within 50 μs requires a sophisticated pulsing voltage scheme and well stabilized electronics to minimize electronic jitters and surges from the power supplies. Furthermore, the utilization of the DT having a wide i. d. of over 5 cm to generate a homogeneous electric field requires a mesh at the exit side of the rf IF that blocks ion smearing and works as a gate, although it can reduce ion transmission.

An early version of achieving high ion utilization efficiency by multiplexing from time dispersive techniques can be found in the FT approach by Knorr *et al.*[59] using IMS. The IMS with a continuous ion source has two separate gates, entrance and exit. These gates are always synchronized together and driven by the same binary square wave (on/off) rather than periodic pulse train without delay. According to their characteristic transit time in the DT under a given condition and gate modulation timing, ions have different outputs and the gates filter ion streams out through drift tube. The output is summed and time-averaged to produce a mobility interferogram using a gating correlation function in real time. FT can convert the mobility interferogram to ATD and this technique claims utilization of up to 25% of ion stream when ion diffusion is considered[60]. A similar trial has been done by Belov *et al*. to increase spectral intensity and signal-to-noise ratio (SNR) using an in-house rf IF interfaced IM-MS instrument [61].

An ion packet entering drift tube is multiplexed by modulation of the exit potential with pseudorandom binary sequence at the end of the hourglass type IF and IM gating is synchronized with TOF MS using IM gating pulse period which is divisible by TOF acquisition time. By this technique, it is possible to achieve ~10-fold increase in SNR and ion utilization efficiency. However, these techniques require extensive modeling to find the correct timing sequence and data processing algorithm conditions for which are difficult to optimize in the case of analytes having unknown mobility characteristics.

Since TOF MS has been popular owing to recent advancements, the coupling of IM to TOF MS is also common. However, the gate timing is always synchronized to TOF extraction pulsing and during the TOF acquisition time, the mobility drift time cannot be acquired (single averaging). Interleaving is a technique which can be pursued when decoupling mobility resolution from mass spectrometer acquisition time[62]. Inherently, the unit time scale of IM is determined by TOF acquisition time in sequential manner. For example, we assume that IM-MS has a time window of 4 ms coupled TOF flight time at specific m/z range of *ca*. 50 μs at extraction frequency at 20 kHz. To identify a peak in IM following a Gaussian shape requires at least 8 data points and a baseline peak width in the range of 400 μs. Therefore, the ultimate number of identifiable data points in the IM time window will be 80 and the number of peaks which it can accommodate will be 10 with this timing scheme if all baseline peak widths are separate. The deficiency limits the resolution of the instrument only to *ca*. 20 according to the definition of IM resolution and the peak capacity, which is a drawback of IM-TOF MS instrumentation[23]. To address these issues, TOF acquisition time should be made shorter and the IM time window has to be increased by adapting a longer drift tube or low gating frequency. Even with the condition of high TOF extraction frequency and low IM gating frequency, the number of ions pulsed to the detector would decrease and overall ion counts would be poor. The interleaving technique can save IM-TOF MS from this instrumentation challenge[22b]. A sequential series of interleaved pulses are inserted by offsetting each other with a certain amount of time during TOF-MS data acquisition as shown in Figure 14. Each interleaved mass spectrum is saved at different local memory and, after the experiment, the sum of all mass spectra generates the ATD.

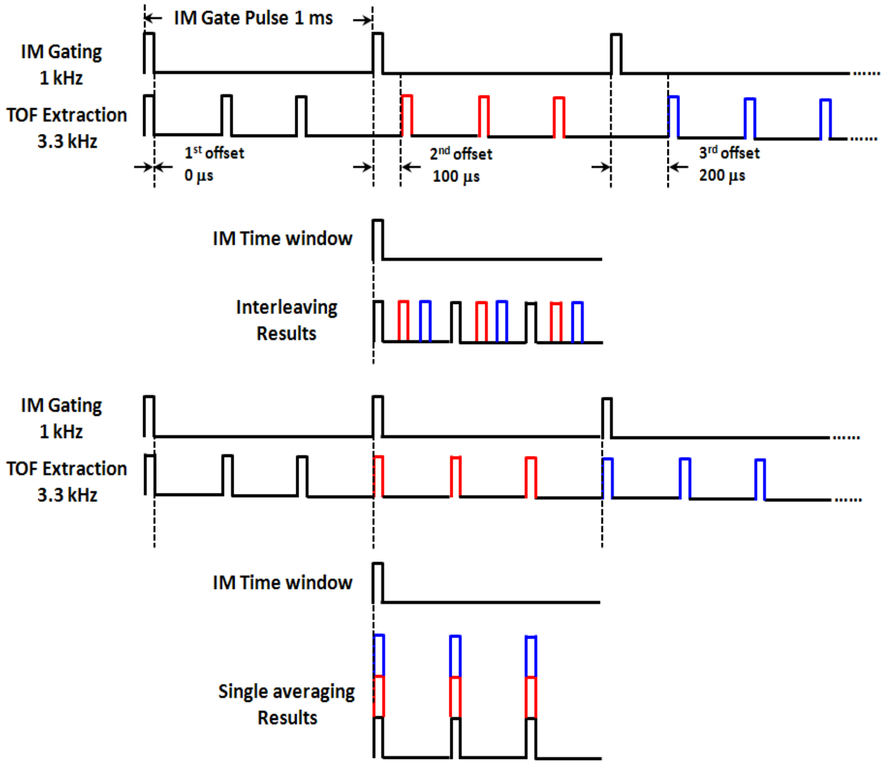

Figure 14. Interleaving vs. single averaging sequential pulse. By offsetting each set of TOF extraction pulse with specific amount of time, the resolution deficiency can be overcome.

Conventional high resolution TOF-MS can be coupled to IM by this method without tradeoff of mobility resolution and MS sensitivity. However, since the number of bins in time-to-digital converter (TDC) is limited by operational unit time resolution, allowance of bins for interleaved pulse sequence sacrifices bins which should be shared for processing mass spectrum signal. Therefore, it might have a restriction on utilizing all available TDC bins and the dynamic range of the TOF-MS but it can be acceptable in general operation.

In this chapter, implementation of ESI PFIG-MS as an IM-MS instrument interfaced with the rf IF will be described. Compared with conventional DTIM-MS in operation with a similar rf IF interface, PFIM-MS can be easily coupled to the tapered IF exit (2 mm i. d.) since PF utilizes narrow 8 mm i. d. electrodes which can minimize ion spreading with proper ion optics working at 0.1~1.0 torr range. Hyphenation of the IF interface to PFIG is also expected to have a synergetic effect for improving ion transmission from intrinsic focusing capabilities of each device and it might not require a supplementary ion trapping region which adds complicacy to the pulsing scheme and electronics. This endeavor includes design and implementation of efficient methods to couple the in-house rf IF to modular PFIGs and interfacing them to an orthogonally accelerated (oa) linear TOF MS detector with the aforementioned interleaving data acquisition system.

Experimental

Modular Periodic-Focusing Ion Guide

The home-built ESI rf IF device was mounted in front of modular PFIGs. The space between the rf IF (~0.7 torr) and first PF IG worked as a differential pumping zone for additional pneumatic focusing. Two modular PFIGs were assembled using Delrin® (polyoxymethylene) flanges and ceramic tubes which contained stacked stainless steel ring electrodes of PF geometry. The first module had 17 electrodes and the second module 28 electrodes. The total length of the two module assembly was 58 cm (23 cm + 35 cm) and each module was sealed by viton o-rings between the ceramic tubes and the flanges. The endcap flanges were tightened by 4 threaded rod in each module. All electrodes inside the PFIGs were connected by a serial resister chain (1MΩ, metal thin film, ±1%) and the aspect ratio of the ring electrode used was 4:3:3 (8 mm i. d. and 6 mm spacing/thickness). The two modules were connected by an external resistor connector having the same specification and sealed by a viton o-ring.

Gate Pulsing and Ring Electrode

The gate was opened by inversed transistor-transistor logic (TTL) pulse signal, which drove a high voltage dc power supply. Then the negative output pulse was combined through a pulse combination box which added the voltage drop on top of the continuous gate-on voltage. To ensure the pressure of the PFIG higher than other regions and prevent buffer gas contamination from intruding air, the gate electrode had 1.0 mm i. d. aperture. A stainless steel ring electrode having 10 mm i. d. and 0.6 mm thickness was mounted by nylon screws on the gate electrode to prevent ions from spreading before the gate electrode.

Ion Transfer Optics to TOF MS

The first module with a 500 μm exit aperture was directly connected to the TOF MS for assessing operation parameters and the two module assembly replaced it later.

According to the measurement of the pressure in the TOF MS and the gas load calculation, the aperture was moved to the last electrode in the two-module assembly and was followed by another differential pumping chamber accommodating 2.0 mm i. d. skimmer to minimize gas load. After the skimmer, ions were guided to the in-house linear TOF MS through three cylindrical electrodes ion optics.

Pressure Monitoring and Mobility Experiment Conditions

The pressures in each section was monitored by capacitance manometers (Type 626 and 722A, MKS Instrument, Inc.) and adjusted by a pressure regulator and manual valves. The schematic and photo of the instrument are shown in Figure 15 and Figure 16. The ATDs were measured at electric field strength of 13.0~23.1 V/cm of 0.6~1.0 torr He (99.999%) in PFIG. The TOF MS consists of a 28 cm flight tube and push-pull pulsing plates at the ion entrance region which extract ion packets from 20 kHz to 40 kHz with 1~2 μs pulse width. The acceleration voltage of ions is usually set to 5.3 kV from the pull plate to the flight tube. Dual microchannel plates (MCP) were aligned to each other with chevron geometry and the voltage drop across the two MCPs was 1.7 kV. A single anode was attached to the back of the MCP assembly. The electric potential across the differential chambers and interface ion optics were simulated using SIMION 8.0 ion trajectory calculations with the hard sphere elastic collision at room temperature in the software package. In-house data acquisition software was used to control the instrument and collect the ATD and MS data (Ionwerks, Houston, TX).

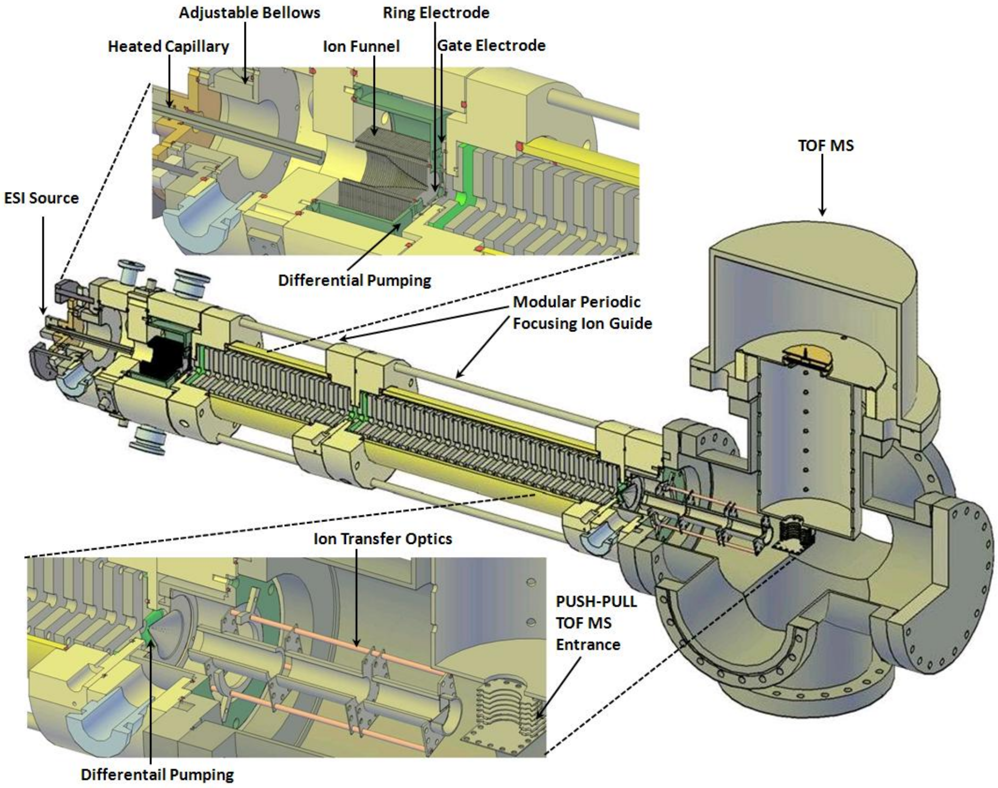

Figure 15. Schematic of the ESI PFIG-MS instrument with cut-away view.

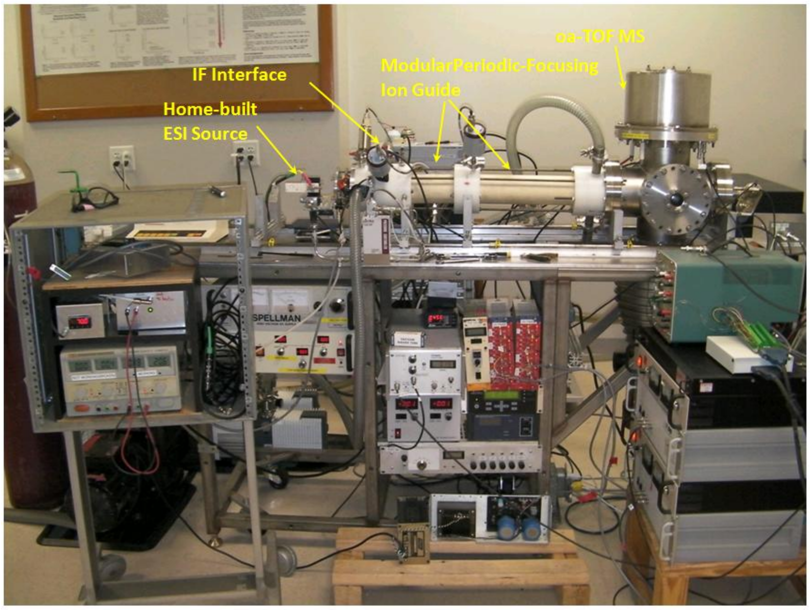

Figure 16. Photo of the instrument. Each major section is labeled.

Chemicals and Sample Preparation

The ATD acquisition using the instrument was examined using various sample solutions. Reserpine (MW 608, Sigma-Aldrich, MO) 37 μM was prepared by dilution with acetonitrile: water: formic acid (50: 50: 0.1, vol. %) as solvent from a stock solution containing 2.0 vol. % of ethyl acetate in acetonitrile for testing the first module directly attached to the TOF-MS. The ion transmission across the entire instrument was tested using 10 μM synthetic cyclic peptide PGPGPG (abbreviated to c$(PG)_3$, MW 462, Sigma-Aldrich, MO) with 100 μM Ca^{2+} from $CaCl_2$ by dissolution in methanol: water (50: 50, vol. %). 1 μM equine heart cytochrome c (MW 12384, Sigma-Aldrich, MO) was prepared for protein ion transmission test by dilution in methanol: water: formic acid (50: 50: 0.1, vol. %). To assess the mobility resolution of the instrument, 16 μM somatostatin (MW1638, American Peptide, CA) and 6 μM tryptophan zipper (TZ)1 (MW 1608, GeneScript, NJ) were prepared by dilution in methanol : water: formic acid (50: 50: 1.0, vol. %). In all cases, the electrospray voltage was 2.0~3.0 kV and the flow rate was 0.5~1.0 μL/min. All solvents were HPLC grade. Chemicals and peptide/protein samples were used without further purification and the HC temperature was maintained at 70℃.

Results and Discussion

Configuration of the interface between the rf IF and to the mobility cell is one of the most challenging parts of the instrumentation. The API source in combination with the HC introduces a strong directional flow of the air. From the previous measurement, the fluctuation of the ion current to the rf IF was noticed through the HC temperature variation. Owing to the balance between desolvation and flow resistance inside the HC, it was necessary to monitor the pressure change for obtaining an optimal flow condition.

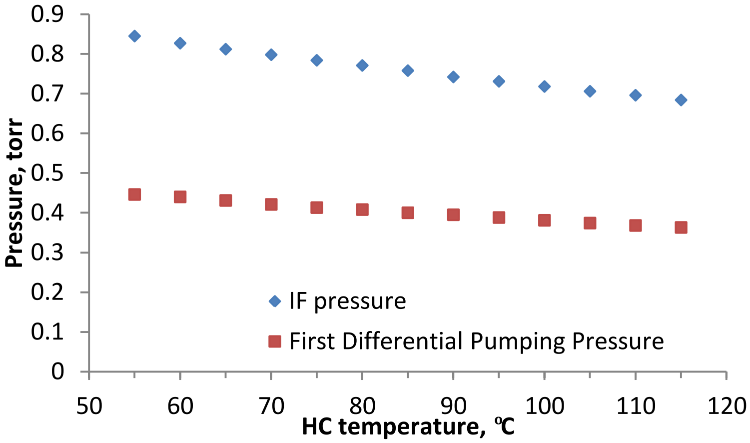

Figure 17. Variation in pressure with the change in the HC temperature measured in the rf IF and first differential pumping region. Relative standard variation of the measurement was less than 0.2%.

The pressure in the rf IF region and the first differential pumping region were measured and the result is shown in Figure 17. Based on the pressure measurement, the ion optic configuration to be installed in the region was designed and investigated using SIMION ion trajectory calculations since each ion optic has different optimum working pressure and voltage drops at a given condition. The interface should not allow the diffusion of external gas into the mobility cell which enables ungated ion transfer and distort the ATD and should include an ion gate to pull ions to the mobility cell. To satisfy these conditions, a Bradbury-Neilsen type gate might be adapted by using thin grids[63]. However, the gate aperture was only 1.0 mm based on available pumping speed and

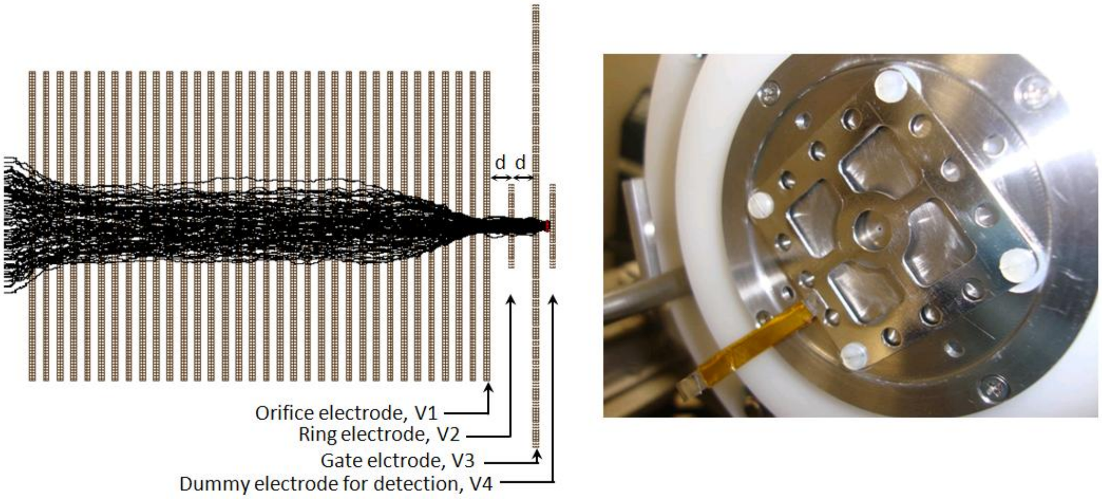

Figure 18. Schematic for SIMION 8.0 simulation in the interface region between the IF and gate electrode (left) and the photograph of the actual parts (right). The i. d. of the ring electrode (square shape in the photo) is 10 mm with 0.7mm thickness. The rf IF condition is simulated for 20V/cm dc field and rf of 800 kHz with V_{pp} 50 under N_2 pressure of 0.5 torr in the region.

application of thin wires crossing the aperture can be hard to achieve and degrade ion transmission. Considering its thickness (50μm) and i. d., imposing uphill potential on the aperture might create a strong electric field around the rim blocking ions when the gate

Table 1. Dc potential setup for SIMION 8.0 ion trajectory calculation and ion transmission from Figure 18. Volt Set 4 means no ring electrode between the orifice electrode of the IF and the gate. The distance d in Figure 18 was conserved with 5 mm in all voltage sets.

Electrode Potential	V1	V2	V3	V4	Ion Transmission (%)
Volt Set 1	90	90	70	60	70.4
Volt Set 2	90	85	70	60	72.8
Volt Set 3	90	80	70	60	71.2
Volt Set 4	90	N/A	80	70	45.6

is off state (inversed pulse mode). In addition, the distance between the rf IF and the gate is critical to minimize ion spreading in the region from SIMION results. A ring electrode was adapted as shown in Figure 18.

Table 2. Ion transmission at various ring electrode positions (d in Figure 18). The rf IF part was omitted in ion trajectory calculations and ions started at orifice plate.

Ion Transmission (%)	d = 3 mm	d = 5 mm	d = 7 mm
He 0.5 torr	93	92	84
N_2 0.5 torr	71	68	52

Although gas dynamics was not considered, ion transmission without the ring electrode was decreased by 37 % relative to the highest transmission Table 1. Since the region would be filled with air from the rf IF and He from PFIG, ion transmission was calculated with two different gas species at 0.5 torr and different ring electrode distance. The results in Table 2 show acceptable focusing effect when using the ring electrode location within 5mm from both sides in the calculations. Compared with He, N_2 shows less focusing effect. Assuming the elastic hard sphere collision, the calculation results can be treated as when a relatively fast moving ion having velocity (v_i) and mass (m_i) collides into a standing gas molecule with mass (m_n). Momentum and total kinetic energy should be conserved and the final velocities of the ion (v_i') and gas molecule (v_n') can be determined from equation (4.1) and (4.2).

$$m_i v_i = m_i v_i' + m_n v_n' \tag{4.1}$$

$$\frac{1}{2} m_i v_i^2 = \frac{1}{2} m_i v_i'^2 + \frac{1}{2} m_n v_n'^2 \tag{4.2}$$

From the equations above,

$$v_n' = \frac{2m_i}{m_i + m_n} v_i \tag{4.3}$$

The transferred energy from ion to gas molecule through the collision is

$$\frac{1}{2}m_n v_n'^2 = \frac{4m_n m_i}{(m_i + m_n)^2}\left(\frac{1}{2}m_i v_i^2\right) \tag{4.4}$$

and the final velocity of ions (v_i') after collision is

$$v_i{}' = \frac{m_i - m_n}{m_i + m_n} v_i \tag{4.5}$$

Therefore, the collision with N_2 slows down the ion more than the collision with He. Since the collision occurs under an electric field, the ion drift motion follows the direction normal to equipotential lines and ions are diffused through the gas. The mean displacements of ions from the origin can be calculated using a distribution function from integration of the number density distribution function at one dimension[15b]

$$|\bar{x}| = \left(\frac{4Dt}{\pi}\right)^{1/2} \tag{4.6}$$

Since the drift velocity (v_d) is the distance (L) divided by the drift time t, the equation above can be written as

$$|\bar{x}| = \left(\frac{4D}{\pi v_d L}\right)^{1/2} \tag{4.7}$$

Therefore, if the drift velocity is slower by collision with heavy gas molecules, ion diffusion is increased and ion path is more deviated from the center axis. Assuming a singly charged ion following the relationship of mobility constant in equation (1.1) and diffusion constant from the Einstein equation ($K=eD/kT$), it reveals that the magnitude of the displacement depends on voltage drop.

$$|\bar{x}| = \left(\frac{4kT}{\pi eV}\right)^{1/2} \tag{4.8}$$

The equation indicates that a higher voltage drop required is to minimize the dispersion of ions from gas molecule collision.

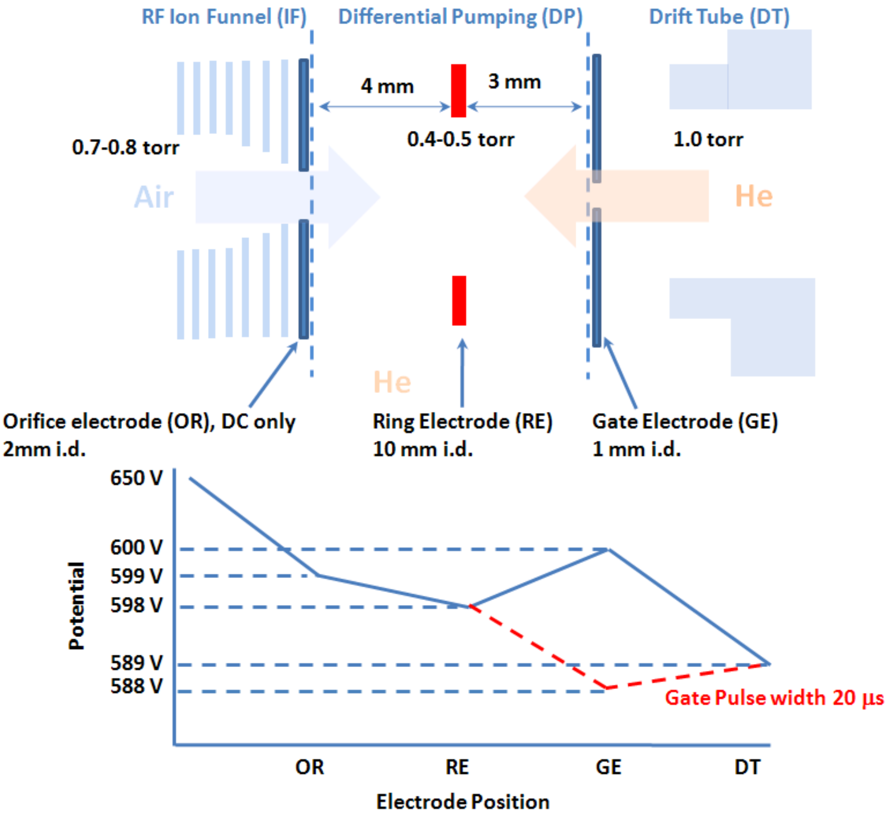

Figure 19. Pulsing schematic in the rf IF and the gate interface region. When the gate is on, GE stays at 600 V and when off, GE drops to 588 V.

Based on the results, the ring electrode was installed using the same size of a stainless steel electrode from the rf IF and the actual i. d. was enlarged to 10 mm to accommodate more ions dispersed by counter-flow turbulence. The pulse schematic was tested to maximize ion transmission across the region as shown in Figure 19. To overcome the turbulence generated by the collision of the two flows from either direction, the gate voltage provided 10 V drop across the region. Considering 2.0 mm the orifice size of the rf IF exit electrode and the pressure drop from it to the differential pumping region, the gas flow dispersion would not be large; the field strength within the 3mm distance between the ring and the gate was 30V/cm which might provide enough downhill kinetic energy to guide ions against the He flow from the PFIG module. Although there was still uncertainty since all ion transmission calculations did not consider gas dynamics, the pulse voltage schematic gave acceptable signal acquisition time (~5 min) to obtain ATDs from sample solutions.

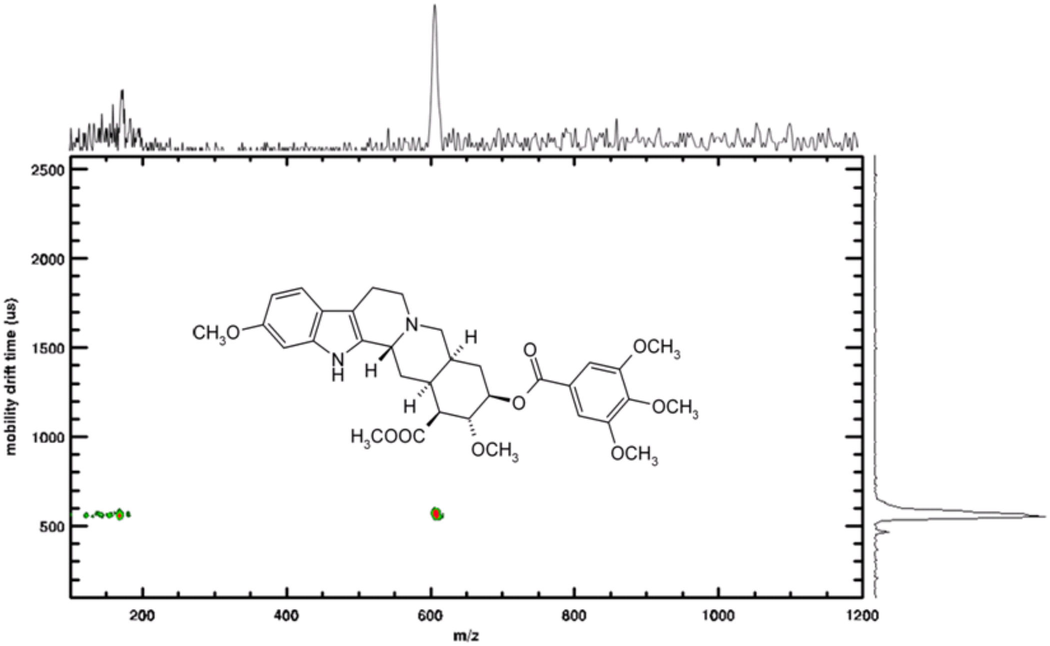

Figure 20. ATD of reserpine with the first PFIG module (23 cm) directly connected to the TOF MS at 23.1 V/cm under 1.0 He torr.

Using the pulsing and gating schematic, the reserpine solution was run through the instrument to characterize operational parameters and acquire the 2D conformational data shown in Figure 20. Based on the peak centroid of m/z 609, $[M+H]^+$ was identified and the ATD distribution showed a well-resolved single peak on the right side of the conformational space, which indicates that $[M+H]^+$ is the most abundant peak. This result is supported from other measurements at similar ESI conditions[64]. The instrument was calibrated by Cs (+) (m/z 132) and ALILTLVS (+) (m/z 829). The streak line with multiple dots on the lower left is assumed as fragment ions from $[M+H]^+$ caused by the given condition, which impelled adjustment of voltages accordingly to reduce unintended fragmentation. However, since the resolution of the TOF MS was low (< 80) and an isotope pattern could not be seen, the other peaks smaller than m/z 200 could not be resolved and identified. The peak ahead of $[M+H]^+$ in the mobility drift time is a noise peak from the acquisition system. By the variation of voltages from the back of the PFIG region, it was possible to calculate CCS of reserpine (265 $Å^2$) at 1.0 torr He pressure. The value was between two available reference values (167 $Å^2$ with He and 280 $Å^2$ with N_2) which were measured by a different type of instruments[65].

Since the pressure of the TOF MS region in the reserpine mobility experiment was 1.4×10^{-5} torr when PFIG in 1.0 torr and the high pressure might increase the collisional activation with large voltage drop required to focus ions in the TOF MS entrance. Therefore, another differential pumping region was introduced before the TOF MS as shown in Figure 15. The ion transfer region consisted of three cylindrical electrodes similar to an einzel lens system. The differential pumping region was connected to a mechanical rotary vane pump (Alcatel 2033, France) after 500 μm exit aperture and before the 2.0 mm i. d. skimmer located 4 mm away from the PF IG exit aperture. After the addition of the differential pumping, the pressure of the TOF MS dropped to 1.2×10^{-6} torr which could provide less fragmentation through collisions and better focusing with less voltage drops (30~70V) among the electrodes. An example voltage set and its ion transmission at the same pressure are described in Figure 21 using SIMION. Each cylindrical lens is 5 cm long with 4.5 mm spacing in between each other. The beam shaping exit slit on Electrode 3 has a width of 1.5 mm and length of 2.5 cm. Another type of electrode system having a stack of 5 PF geometry electrodes with the similar cylindrical lens was used to guide ions to the TOF push-pull entrance without a differential pumping. However, from SIMION simulation and experimental results, effective potential focusing was not able to achieve high ion transmission without a high voltage drop because the pressure was lower than 10^{-4} torr and jet expansion from the PFIG exit was dominant. The mount of the PF electrodes in this region might skim the

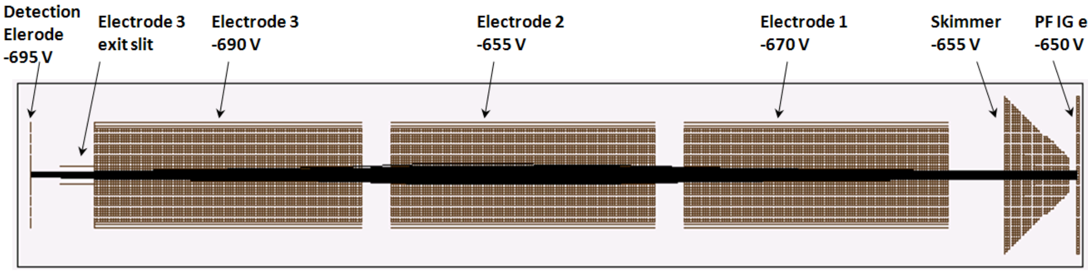

Figure 21. Ion optic simulation from the PFIG exit to TOF MS region. The pressure was 1.2×10^{-6} torr He and at the given electric potentials on each electrode the transmission was 92%.

skirt of jet spread and allow only the central portion of the jet stream to the next electrodes. This was identifiable by burn marks on each PF electrode which had expanding concentric circle pattern as the electrode was away from the PFIG exit. Rather than application of PF electrodes at the beginning of the jet expansion, differential pumping after the PFIG exit and the skimmer take advantage of pneumatic focus. Although the three-electrode einzel lens system is used to focus ions not by changing the axial velocity but changing radial velocity with applying the same voltage on the entering and exiting electrodes and specific potential on the middle to achieve intended focusing distance to next ion optics, it can be applicable for different approaches. In addition, this region is one of the sections most vulnerable to gas dynamics and it is required to minimize the time spent by ion (out-of-drift tube time) to increase the mobility resolution. Acceleration of ions was inevitable for this reason. Multipole ion guides can be applicable if they are carefully adapted to eliminate time delay by trapping effect with collision at elevated pressure[34c]. Electrode 3 had the same potential with the grid in the middle of push-pull electrodes which worked as a bias.

To calculate CCS from mobility experiments, the electric field strength is varied and other potentials on the following electrodes should be adjusted accordingly. The kinetic energy of the ions escaping the PFIG should be kept the same to keep the time that ions spend outside of the PFIG constant. To meet this requirement, the electric potentials from the PFIG exit to the bias of the TOF push-pull electrodes were set to maintain the same amount of voltage drop among the electrodes while the potentials at the front part of the instrument from ESI source to the first electrode on the first PFIG module were constant. Some of the in-house instruments built by other groups accommodate the IF exits instead of using an aperture to reduce ion loss by the conductance limit owning to the fact that large i. d. ring electrodes (~5 cm) are used in the uniform field DT[36b, 57]. Since the PFIG utilizes the narrow i. d. ring electrodes (8 mm) and at the exit aperture pneumatic focusing helps ions to escape, the second rf IF was not considered. The optimization of the potentials requires experimental trial and error procedures to find the highest ion count through the TOF MS.

However, there were discrepancies of the set voltages and actual voltage outputs through each power supply channel during manual adjustments. LabView® control might diminish the difficulties of the output voltage controls with the resolution of 0.3V out of the range of -100V~ -750V. The negative voltages were established on the electrodes from the PFIG exit to decrease breakdown since the PFIG was at 1.0 torr He wherein the Paschen curve indicates the lowest breakdown voltage[30]. This strategy is based on the observation that most of the time breakdown occurs in the interface regions. Initiation of breakdown starts from acceleration of electrons or ions by the electric field leading to a cascade ionization process or self-sustained electrical avalanche by collisions with other gas molecules[66]. Even though the electric field produced by a voltage gradient across the PFIG was not high enough to induce discharging at a given pressure, rough electrical connections and sharp edges of parts might raise discharging by strong local field strength to find a pathway to nearby ground potential or sudden voltage drop point. Because of this reason, the fast flow of He by pressure drop is sensitive to the potential drop within a short distance to reduce ion diffusion. Based on the total resistance of the two PFIGs, the position at 32 cm from the gate electrode reaches the ground potential and the parts past the position are faced with about half of the applied voltage drop. There are several countermeasures to prevent the breakdown from exposed ground potentials through floating entire electric potentials to a certain reference[36a] and lessening the exposed area of parts by surrounding electrodes with insulating materials (except the inner side of ring electrodes) and letting the connecting leads be exposed to atmospheric pressure[36b].

Since Electrode 3 in Figure 21 had the same potential as the TOF source bias voltage between the push and pull plate and the TOF source design was very close to a simple Wiley-Mclaren type [67], it is inevitable to observe the shift of m/z as the electric field strength was changed and independent voltage control for ion beam shaping and focusing ions to the TOF entrance is necessary.

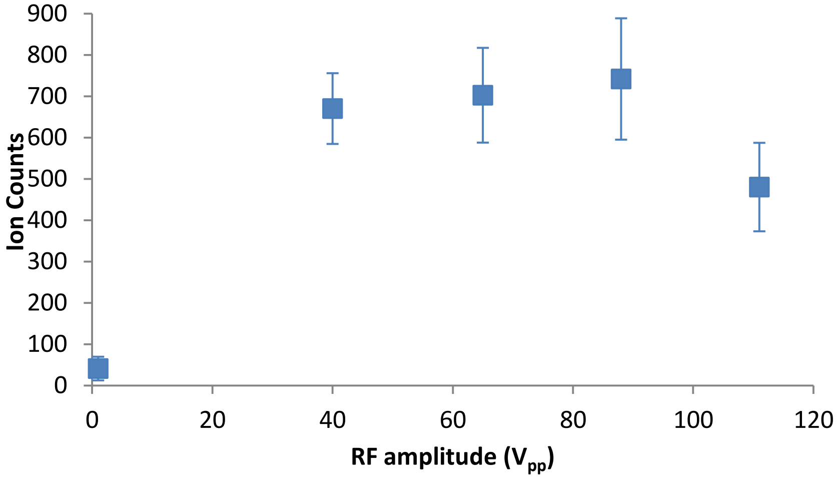

Figure 22. Ion counts variation in the ESI PFIG-MS at different rf V_{pp}. 10 μM c(PG)$_3$ with 100 μM Ca(+2) in methanol: water(50:50) at 19.3 V/cm across the PFIG and 1.0 torr He.

After connecting all interface sections and the two PFIG modules, the test of overall ion transmission across the entire instrument was performed using $[c(PG)_3 + Ca]^{2+}$ ion giving the data shown in Figure 22. $[c(PG)_3 + Ca]^{2+}$ has been a model for the study of complexation through non-covalent bonding interactions between carbonyl oxygen and metal cations using ESI-MS[68]. Therefore, it was selected to test the ion transmission and check the voltage setups to see whether they would be high enough to dissociate the nonbonding interaction. The ion count of $[c(PG)_3 + Ca]^{2+}$ (m/z 251) was monitored at various rf amplitude and other voltages were constant. The result shows the anticipated increment of the ion counts as the rf amplitude increases, which indicates successful hybridization of the rf IF to PFIG. The rf amplitude in the plot represents actual rf amplitude measured by an oscilloscope in operation.

Although the resolution of the TOF MS was not high enough to identify isotope distributions, multiple charge states from large molecules might be identifiable in the 2D conformational plot since the variation of CCS is anticipated from different Coulomb repulsion of multiple charges on a small protein like cytochrome c. In Figure 23, the top 2D plot is the ATD of cytochrome c when the small PFIG module was connected to the TOF MS and the bottom plot is the result from the two consecutive modules using the same solution. As shown in the alignment of different charge states in the 2D conformational space, it is noticeable that the contours from each charge state are converged to a narrow ATD peak in the case of the short PFIG module with a shallow slope, whereas the steep slope shows more inclination among the contours and partially resolved peaks around the ATD in the long PFIG. Although the pressure and electric field strength are slightly different, this is confirmative that the increase in the total distance of PFIG contributes to separation of each charge state.

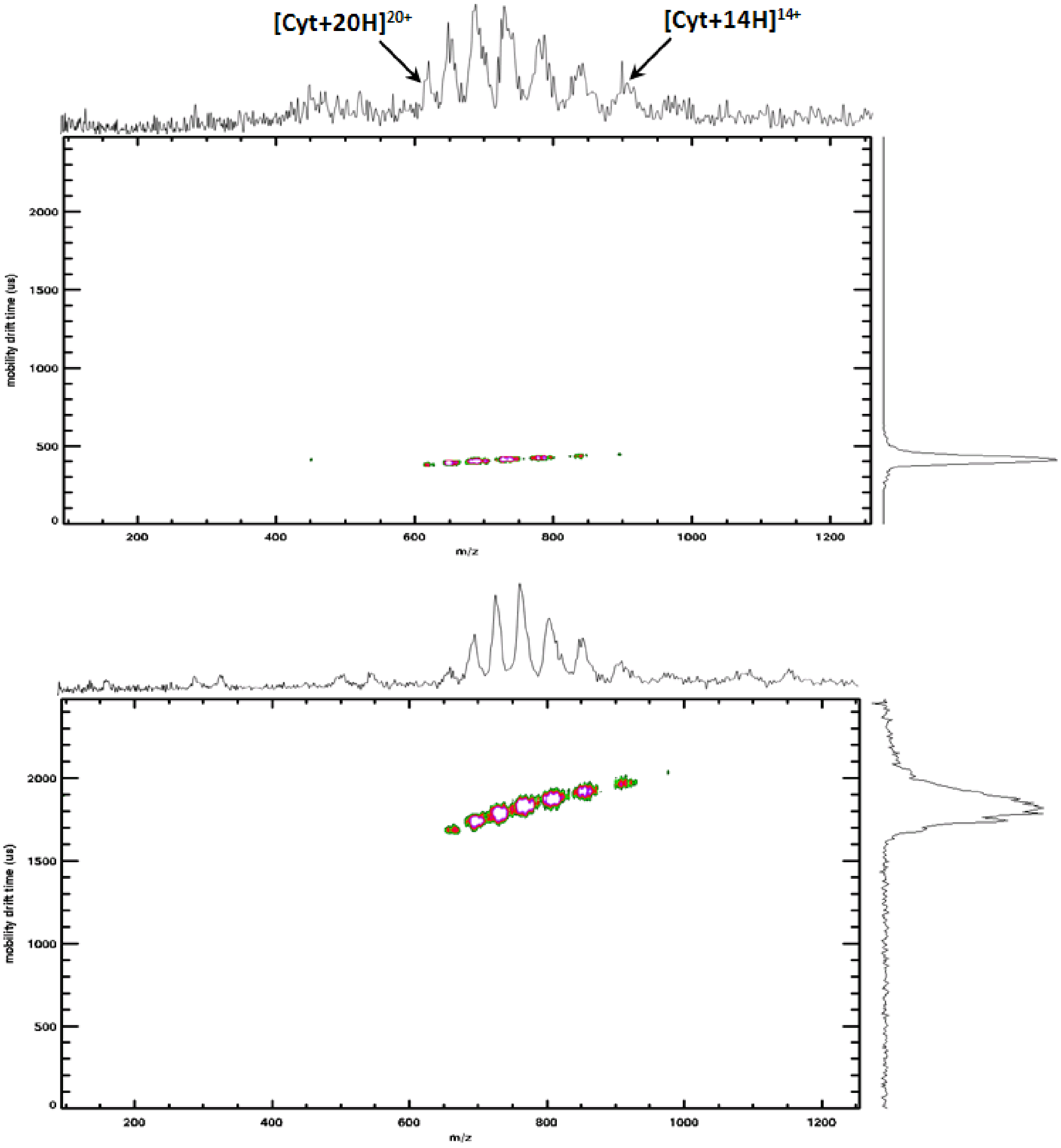

Figure 23. Single module (22 cm) in the ESI PFIG-MS data (top) under electric field of 23 V/cm at 0.6 torr He with 1 µM horse heart cytochrome c and the double module (58cm) result of the same solution (bottom) under electric field of 19 V/cm at 0.8 torr He.

Since the first goal of the IM-MS is the separation of ions having different conformations, the resolution might be an index of the instrument performance. Hence, the ATDs of TZ1 (+3) and somatostatin (+3) were measured using the instrument to determine a single peak resolution. Somatostatin, a peptide having 14 amino acids of which Cys(3) is connected to Cys(14) through a disulfide bond is expected to exhibit a narrow ATD owing to a rigid cyclic structure[69] and TZ1 has a beta hair pin structure are well known for stable ion conformation from the other studies[70]. These structural identities might be maintained and the single peak resolution of the instrument was determined using these two molecules. As shown in Figure 24, the ATDs for the $[M+3H]^{3+}$ ions of somatostatin and TZ1give a resolution of 56.5 and 58.8, respectively, at 19.3 V/cm under 1.0 torr He. The diffusion limited resolution equation explains the

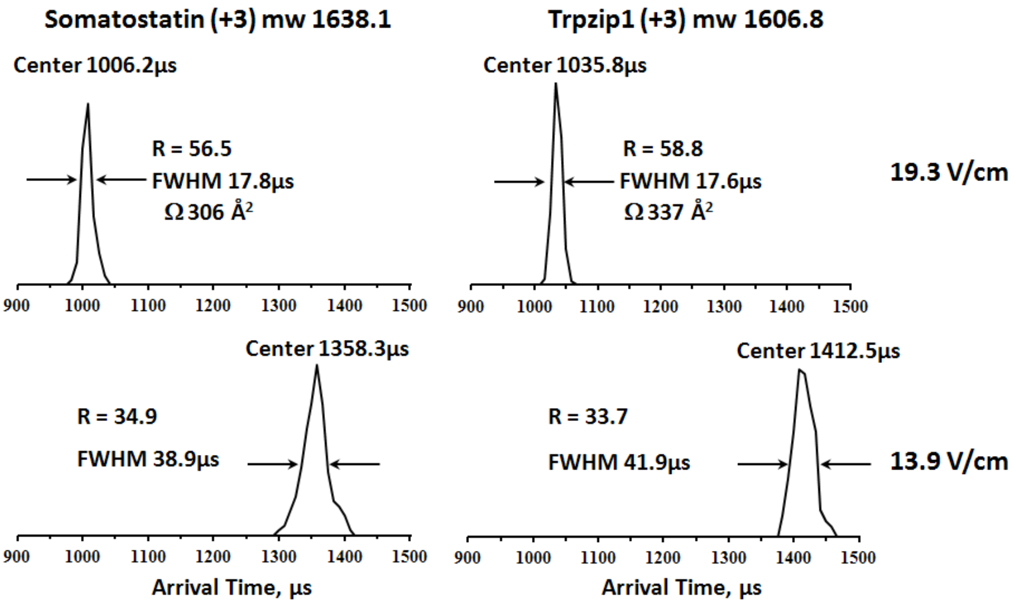

Figure 24. Single peak resolution of the in-house ESI PFIG-MS using somatostatin (+3) and TZ1 (+3).

decrease of resolution at low field strength since the resolution is proportional to the square root of the field strength. However, the equation is derived from collisions of atomic ions and gas molecules. Dynamics of conformational change in peptide/protein ions has multiple degrees of freedom when ions collide with buffer gas molecules including internal energy redistribution and vibrational excited states. Thus the resolution change at different field strengths would not follow a straightforward relationship from the equation. Also, since the ATDs of both peptides are not Gaussian, it is possible that there are more than two different conformers. However, the overall ATD profiles at the two different field strengths are conserved in each case and this data supports the possibility of having ATDs at intermediate and high electric field strength compared to the DTIM-MS without significant distortions.

Conclusions

Implementation of ESI PFIG-MS with the rf IF interface was accomplished by consideration of appropriate ion transfer optics and gate schematic. Application of ion trajectory calculations was successful in designing the ring electrode and ion transfer optics including the estimation of operation voltages. The mobility resolution and total ion transmission were tested by the sample peptides and protein solutions including the metal-peptide complex, which gave high resolution in the case of the (+3) charge states of the selected peptides. These results strongly support the application of the instrument for CCS calculations derived from ATD measurements.

CHAPTER V

COLLISION CROSS SECTION CALCULATIONS USING ELECTROSPRAY IONIZATION PERIODIC-FOCUSING ION GUIDE-MASS SPECTROMETRY

Mobility Correlation Factor

Determination of CCS by IM-MS has been providing various opportunities in chemical and biological research to derive structural information as well as additional ms time window of mimicking solution phase chemistry by virtue of soft ionization techniques[71]. ESI IM-MS is an alternative to X-ray crystallography and NMR, which are the conventional methods for investigating conformations of peptides and protein. It is a time-saving and efficient tool for elucidation of solution phase structures because of convenient access and intuitive data interpretation. So far, the results from studies where only solution factors such as solution composition are varied definitely show that conformation changes in gas-phase ions are related to structural variation in solution phase mediated by non-bonding interactions[21, 72]. Efforts continue toward obtaining and observing native states of peptides/proteins without complicated data interpretation. To keep pace with the march, instrumentation should be accompanied by comprehension of available technologies and exploration to develop better pathways for the next level of advancement.

PFIG has shown high ion transmission which was one of the challenges faced by IM-MS[4c, 31b]. However, MALDI PFIG-MS requires calibration to report CCS from measurements and the calibration procedure should consider a variety of factors including electric field strength, gas pressure and type of ions or calibrants[31b]. Even in commercial IM-MS, rigorous calibration is essential to obtain CCS by thorough investigation of charge states of ions to be measured and selection of calibrants which have molecular weights close to analyte ions[73]. The basic principles of IM-MS do not require these additional steps to calculate CCS and the calibration approach is a necessity for peculiar instrument characteristics.

Since PFIG has characteristic additional ion drift motions[31a], it is not intuitive to compare the CCS values using the instrument with DTIM results. The sinusoidal motion of ions owing to the variation of the fringing field around ring electrodes, and the field free region at the center of the electrodes overall increases the distance travelled by ions[31c]. However, calibration of the instrument using known CCS values from DTIM amplifies the inconvenience of this application and eventually, users should adjust the instrument parameters based on calibration data. Besides, there is no absolute calibrant that will guarantee accurate CCS calculation and the values from DTIM-MS of the same ion differ by a few percent from instrument to instrument[74]. Hence, development of correlation factor connecting CCS measurement from PFIG to DTIM might facilitate calibration procedures and widen the application of PFIG-MS.

By comparison of the data using a known CCS from DTIM with SIMION ion trajectory calculations, it was found that the slope of the plot of arrival time vs. $1/V$ from PFIG is apparently smaller than that from DTIM[75]. The discrepancy can be expressed as the ratio of the two slopes and this was found to be close to 0.79. When the electric field strength is low, PF cannot be achieved since the repetitive sinusoidal motion of ions demands conversion of mode in the radial direction. The radial momentum of the ions is caused by the field gradient heading toward the center of the ring electrode (field free region) from the rim of the electrode. Hence, minimal field strength to generate and maintain radial momentum of ions is crucial.

The ratio of the slope of the arrival time vs. 1/v from PFIG to that of DTIM is a measure of the deviation from normal drift motion. The estimated value of this ratio is less than 1 in low and intermediate fields. When the field strength increases (high E/N), the two slopes are convergent owing to dominant axial drift motion in both DTMS and PFIG[75]. Thus, the empirical suggestion of this correlation factor, “damping factor α”, is represented mathematically as

$$\alpha \approx \frac{1/n_{z,\mathrm{PF\ IM}}}{1/n_{z,\mathrm{DT\ IM}}} \tag{5.1}$$

where n_z is the number of ion-neutral collisions per unit axial (z) displacement. This expression gives us an intuitive sense of the origin of deviation because in PFIG, ions have more collisions owing to the sinusoidal pathway during traveling the unit distance which results in an increment of arrival time. The collision during radial ripple motion can be affected by field variation according to the radial position of the ion since the field strength is dropping to the direction of the center of the electrode. However, the trajectory calculation shows that the contribution is less than 2 % of overall collisions[31a]. Based on these simulation results, the relationship of calculated CCS in PFIG and DTIM was investigated using well known model peptide/protein ions.

Experimental

Chemicals and Solution Preparation

Peptides and proteins were purchased from Sigma-Aldrich (St. Louis, MO) and used without further purification. Bradykinin1-9 (BK), LHRH, angiotensin II, melittin, and horse heart cytochrome c were diluted to the concentration of 1 to 50 μM in methanol: water: formic acid (50:50:0.1, vol. %). A 10 μM solution of bovine ubiquitin was prepared in water: formic acid (99.99: 0.01, vol. %) to obtain lower charge states in the given ESI condition (0.5 μl/min flow rate and ~ 2.8 kV electrospray voltage)[76]. A 10 μM solution of cyclic PGPGPG peptide (abbreviated to $c(PG)_3$, MW 462, Sigma-Aldrich, MO) was prepared by dissolution in methanol: water (50: 50, vol. %) and mixed in a 1:1 vol. ratio with 100 μM of Ca^{2+} , Mg^{2+}, and Cu^{2+} from $CaCl_2$, $MgCl_2$, and $CuCl_2$, respectively. Phosphorylated peptides were obtained from Dr. Helen Cooper at University of Birmingham, UK and 15μM solutions were prepared using methanol: water: formic acid (50:50:0.1, vol. %) as solvent. All peptides and proteins were used without further purification. The spray tips were made by a pulled capillary method using 330 μm o.d. and 50 μm i.d. fused sillica coated with polyimide[77].

Mobility Experiment Conditions

The heated capillary temperature was 75℃. The rf IF was set to 44~77 V_{pp} (measured amplitude) with the dc field 10 V/cm at the pressure of 0.78 torr. All arrival time measurements were performed at 1.0 torr of ultra high purity (99.999%) helium. Mobility drift time was determined using the field strength ranging from 10 V/cm to 19 V/cm at every 1.7 V/cm step. PFIG electrodes had 8mm: 6mm: 6mm (i. d.: spacing:

thickness) aspect ratio. The potentials after the PF IG modules and ion transfer optics were adjusted to maintain the same kinetic energy accordingly for each voltage setting. Measurement of arrival time was repeated 5 times at the same voltage set and the relative standard deviation was less than 0.3% for the arrival time of each ion at the given voltage setting. The peak centroid for arrival time reference was determined using the in-house data processing program by Ionwerks (Houston, TX). Mobility gating pulse frequency was 200 Hz and the pulse width 20 μs. The TOF MS was calibrated with the (+2) and (+3) peaks from tryptophan zipper 1(MW 1606.8) and its pressure was ~1.8 × 10^{-6} torr and with extraction frequency by push-pull action of 20 kHz and pulse width of 1.0 μs. Data acquisition time was 1~ 5 min for each ion species.

Results and Discussion

The number of collisions between analyte ions and buffer gas molecules repetitively changes as the fringing field varies and this results in longer drift time. However, the sinusoidal motion also depends on drift tube pressure and electrode geometry since the ion focusing in PFIG can be affected by not only variation of the characteristic unit distance z_0 from equation (2.4) but also the number of collisions at the given field strength[31b, 31c]. Hence the consideration of the correlation factor α should involve the pressure and geometric specificity. These expectations are theoretically based on the relationship of the effective potential with angular frequency from equation (2.4) which in this case, is determined by velocity of the traveling ion and the specific unit distance. Increased pressure at the same electric field strength slows down ions and the magnitude of effective potential decreases.

An additional effect that should be considered in validation of the correlation factor α is the charge state of ions. As PF is increased by high electric field, the charge state of ions induces a similar effect since the effective potential also can be augmented by the incremental charge state. The effect was obvious in the initial data interpretation (Figure 4 in reference 75). The originally derived factor of 0.79 from SIMION was

Table 3. Correlation factor α; the values were derived from experimental values by comparison with literature values. The charge dependence was corrected by $\alpha(z) = 0.00303 \cdot z + 0.757$.

Ion Charge (z)	Correlation Factor α
1	0.760
2	0.763
3	0.766
4	0.769
5	0.772
6	0.775
7	0.778
8	0.781
9	0.784
10	0.787
11	0.790
12	0.793
13	0.796
14	0.799
15	0.802
16	0.805
17	0.808
18	0.811
19	0.814
20	0.817

*The table was adapted with permission from American Chemical Society, Copyright © 2012[75].

applied by multiplication with the arrival time of individual analyte ion and the percent difference in predicted CCS with the literature values decreased as the charge state increased. The charge state dependence required modification of the factor and the pursuit of a linear relationship was performed by polynomial fitting of the experimental values. From the results of 14 different charge states from peptides and proteins, it was clear that the percent difference between the reported values from DTIM-MS and PFIG-MS was ~ 4.0 % considering the charge dependence of α in Table 3. The α corrected CCS from PFIG-MS has high correlation coefficient ($R^2 = 0.999$) with the literature values, indicating remarkable linear relationship between these two measurements[75]. Since a higher charge state accompanies more acceleration in the axial direction ($F = qE = ma$), it is reasonable to think that the axial drift momentum normal to equipotential lines is dominant. The contribution from the effective potential confinement and acceleration of axial drift motion are likely to be synergetic owing to the reduced travel time from the increased velocity and small amplitude of radial motion. Therefore, PFIG is anticipated to have different ion transmission efficiency relative to the charge state of ions at the same field strength. This effect requires further investigation through comparison of multiple charge state distribution of single peptide/protein ions with the results from DTMS. So far, the range of α values ($0.76 \leq \alpha \leq 0.82$) is very close to the simulation result (0.79) and the elastic hard sphere model shows good agreement with empirical results (Table 3).

Table 4. Calculated CCS values from ESI PFIG-MS in 1.0 torr He at 300 K using the correlation factor α.

Peptide/Protein	z	PFIG-MS	Reference	% Difference
		Ω, Å^2	Ω, Å^2	
Bradykinin	2	245	246[78]	+0.4
			236[79]	+3.9
			242[9]	+1.3
			237[80]	+3.4
LHRH	2	250	240[81]	+4.0
			247[74b]	+1.2
Angiotensin II	2	254	253[82]	+0.2
			245[80]	+3.5
Melittin	4	583	572[83]	+1.9
			576[83]	+1.2
	5	593	602[83]	-1.4
			605[83]	-1.9
Ubiquitin	8	1384	1442[84]	-4.0
		1577	1622[84]	-2.7
	9	1603	1649[84]	-2.8
			1612[84]	-0.5
			1670[84]	-4.0
	10	1716	1732[84]	-1.0
			1689[84]	+1.6
			1730[84]	-1.8
Cytochrome c	14	2448	2473[85]	-1.0
			2435[79]	+0.6
			2451[9]	-0.1
			2520[80]	-2.8
	15	2555	2579[85]	-0.9
			2564[9]	+0.3
			2600[80]	-1.7
	16	2633	2679[85]	-1.7
			2642[9]	+0.3
			2670[80]	-1.4
	17	2731	2723[85]	+0.3
			2740[80]	-0.3
	18	2798	2766[85]	+1.1
			2800[80]	-0.07
	19	2921	2800[85]	+4.3
			2870[80]	+1.8

*Part of the table was adapted with permission from American Chemical Society, Copyright © 2012[75]. The literature references used in the table have been modified from the citation.

The confirmation of the correlation factor α definitely enhances the application of ESI PFIG-MS. The multiplication of the α factor to the calculated CCS from ESI PFIG-MS can provide the proximity of DTMS results to users with a reasonable accuracy. However, note that CCS values are different among DTMS results for the same ion as shown in Table 4. The source of error in ATD might arise from the pressure fluctuation in the mobility cell, instability of electric potential from the power supply during the experiments, and the peak centroid deviation from ATD profiles, since all reported values are not ranged but only single-numbered. From the ESI PFIG-MS results, the instability of the instrument parameters is less than 0.3 % in general and the difference (~ ±4%) in CCS is likely from the peak centroid variation in ATD profiles, indicating the necessity of close examination of the ATDs. Including the peptides and protein ions from Table 4, comparison has been performed by using available drift time profiles from the literature.

BK has been extensively studied using IM-MS. The reported CCS of $[BK+Na]^+$ and $[BK-H+2Na]^+$ are $245 \pm 5Å^2$ and $247 \pm 5Å^2$, respectively, which agrees very well with $[BK+H]^+$ ($242 \pm 5Å^2$) using MALDI DTIM-MS[86]. The experimental results support globular structures wrapping metal ions, leading to narrow ATDs, of which a β-turn is most likely present in the structure as indicated by a solution NMR study[87]. In addition, the presence of salt bridges mediated through the interaction of proton/sodium ion with carbonyl groups in the backbone and both guanidine groups in arginine

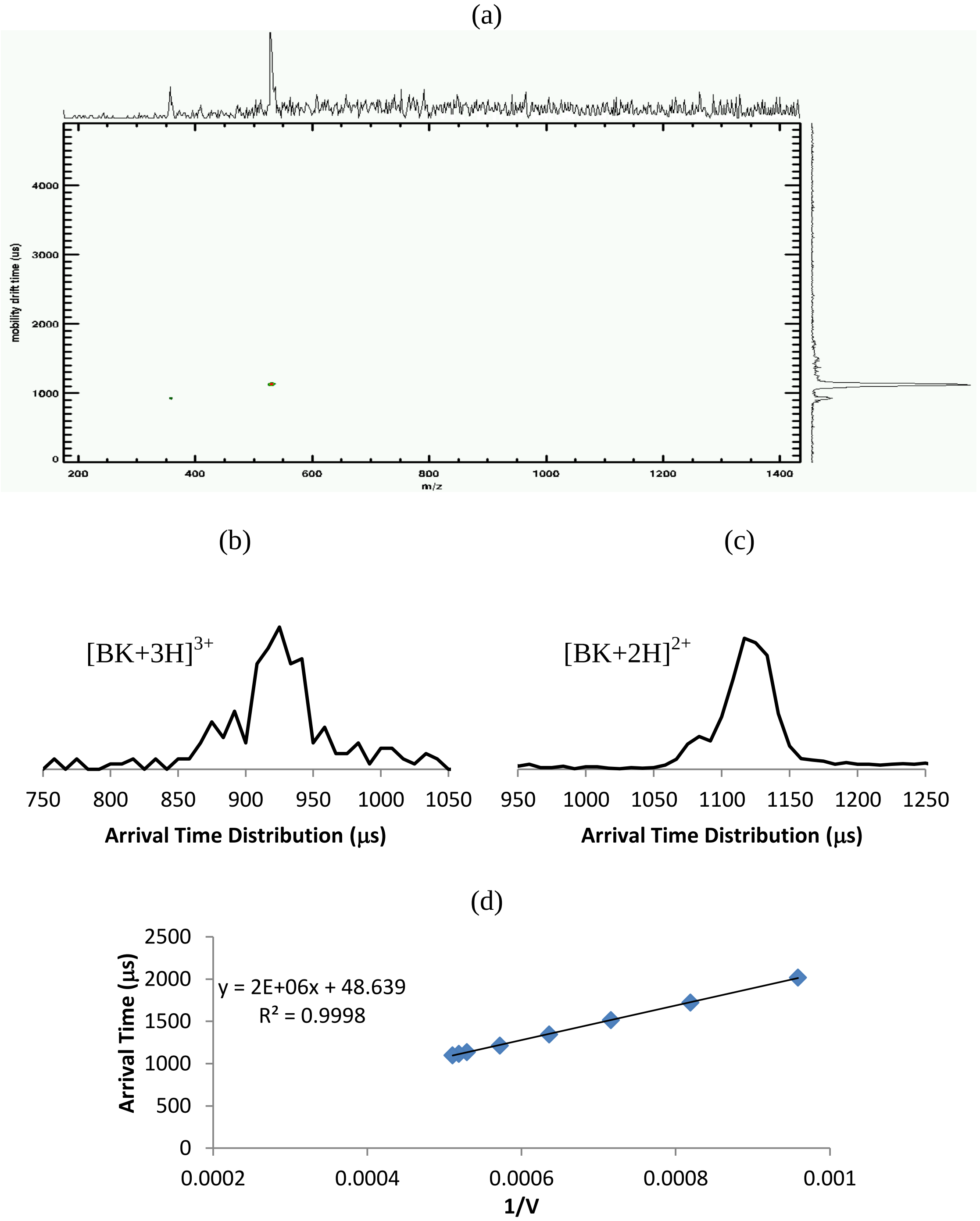

Figure 25. (a) BK ions in 2D conformational space; $[BK+2H]^{2+}$ and $[BK+3H]^{3+}$ are observed at m/z 531 and m/z 354, respectively, (b) m/z selected ATD for $[BK+3H]^{3+}$and (c) for $[BK+2H]^{2+}$at 19.3 V/cm and 1.0 torr He (d) arrival time vs. 1/V plot for $[BK+2H]^{2+}$. The correlation coefficient is 0.9998 for a wide range of field strength (10.4 ~20.3 V/cm).

terminals was indicated in the MD simulations[86]. Intriguingly, the broadening of ATD is negligible and independent of temperature between 300 and 600 K, although two peaks of $[BK+H]^+$ were resolved at 80K[86]. More interestingly, even strong Coulomb repulsion is anticipated to destabilize the salt bridge interaction, the CCS values of $[BK+2H]^{2+}$ calculated from ESI DTIM-MS and ESI PFIG-MS in Table 4 are very close to those of $[BK+H]^+$. It might be a different ionization process such that MALDI would generate 'hot' ions compared to ESI. However, the CCS from $[BK+H]^+$ from another ESI DTIM-MS study was reported to be 242 Å^2, strongly supporting that the conformers from the two different ionization source might have a similar structure[78]. Although it is not clear how conformations of the two charge states have very close CCS and generation of doubly charged ions using MALDI is hard to accomplish for thorough investigation, it is likely a different intramolecular interaction that plays a key role to stabilize the additional charge when ionization occurs. Sawyer *et al*. provided strong evidence for the conformational stability using the RPPGF peptide during a MALDI process, which reveals a compact conformer having a β-turn close to $[BK+H]^+$, while an extended form does not show the similarity at different solvent compositions[88]. It is likely that the charges still interact on the entire globular conformation and intramolecular interactions provide rigidity to prevent the structure from unfolding in a very subtle way. Extended forms were observed by Purves *et al.* using FAIMS and susceptible variation of conformers in the given condition was suggested[89]. The operating condition for FAIMS is different from that of IM-MS which is under single gas species at low pressure using low-to-intermediate electric field but the additional charge obviously increases the instability of ion structures. There are also several studies reporting multimeric conformations which are dissociated to monomers having multiple conformers by low energy activation[5b, 13, 78, 90]. More evident data which can be compared with the results from the ESI PFIG-MS in Figure 25 is provided by Baker *et al*. using the IF interfaced ESI DTIM-MS at elevated pressures[79]. Through the 88 cm long DT by maintaining ~4V/cm field strength, $[BK+2H]^{2+}$ clearly shows more than two conformers reflecting that the salt bridging is not likely as effective as for $[BK+H]^{+}$. Additional confirmation is available from the results of Kemper *et al*. showing multiple structures with high resolution DTIM-MS[57]. From the data presented in Figure 25 (b) $[BK+3H]^{3+}$ is also anticipated to have multiple conformations which is consistent with the results from molecular dynamics simulations which shows possibly three different CCS domains[91]. The observation of multiple conformers from $[BK+2H]^{2+}$ (Figure 25 (c)) is clearly one of the reasons for the difference in CCS values among DTIM in Table 4. Therefore, the ATDs of PFIG are surprisingly compatible in the case of $[BK+3H]^{3+}$ and $[BK+2H]^{2+}$ including the linearity in the plot of arrival time vs. 1/V in Figure 25 (d). Unfortunately, it was not possible to obtain CCS for $[BK+3H]^{3+}$ in the experiment owing to the low ion abundance and poor signal-to-noise ratio at low field strength.

Angiotensin II (DRVYIHPF) is another model peptide that is frequently used to evaluate new instruments[5b]. Under low field condition, in DTIM, the $[M+2H]^{2+}$ of Angiotensin II (+2) (m/z 524) appears in a narrow arrival time without shoulder peaks or peak broadening[57, 92]. The measured ATD in Figure 26 corresponds to the resolution of 41 in ESI PFIG-MS and the peak shape is very close to Gaussian.

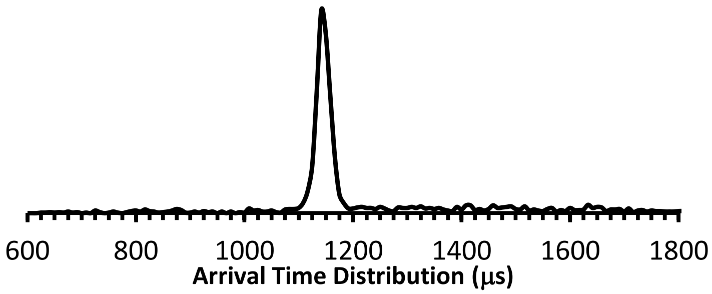

Figure 26. ATD of Angiotensin II (+2) at 19.3 V/cm under 1.0 torr He in ESI PFIG MS. FWHM is 28 μs and the peak centroid is 1155 μs (single peak mobility resolution of ~41).

For much more complicated samples, i.e., gas-phase ions of proteins, it is challenging to understand variations in conformations. However, IM-MS can provide a simplistic and intuitive measurement in this case. In addition, structural information of proteins and their complexes with other partners are critical to understand physiological and biological functions[7]. Cytochrome c is one of the extensively investigated examples and it is a useful model protein to characterize ESI IM-MS for ATD measurements[9, 85, 93].

Comparison of the sum of individual ATDs for each charge state in this study with the results from Baker *et al.*[79] shows remarkable agreement of the results with the drift time profile at 4.0 torr He and 4.0 torr N_2 (see Figure 27). Even though individual peaks from each charge state are convoluted together, the specific charge state ion can be easily identified by picking the spikes along both shoulders.

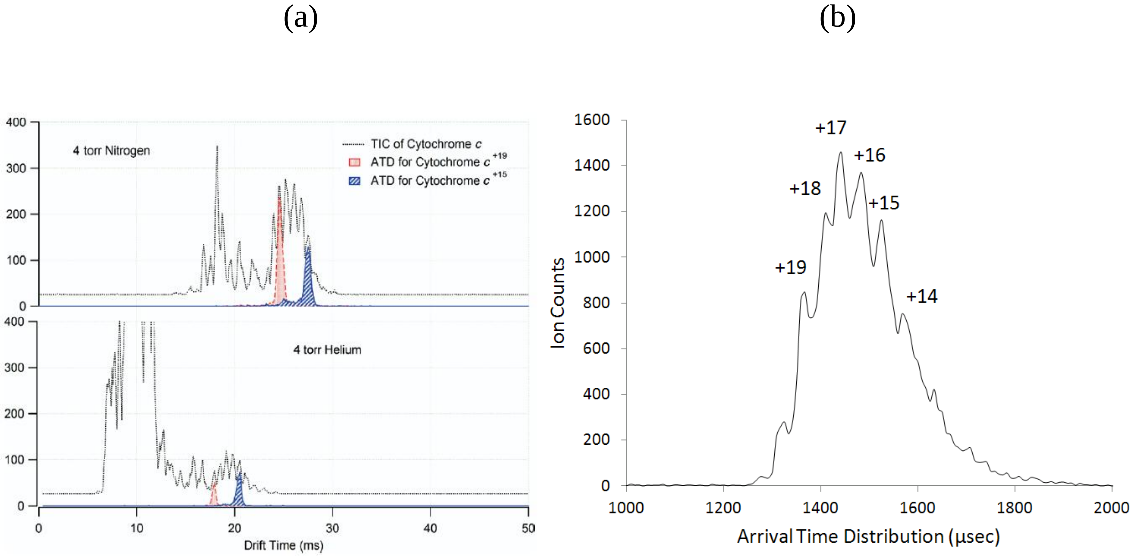

Figure 27. Cytochrome c ATD profiles (a) 4 torr N_2 (top) and 4 torr He (bottom) using 98 cm long DTIM at 18 V/cm the reference[79], adapted with permission from Springer, and (b) 1.0 torr He with 58 cm PFIG at 19.3 V/cm under 1.0 torr He in this study.

The m/z of ions with selected ATDs were compared with the available results from [cyt+14H]$^{14+}$ to [cyt +19H]$^{19+}$ given in Figure 28. The charge states lower than [cyt+14H]$^{14+}$ could not be discerned under the experimental conditions owing to the low MS resolution of the instrument and high background noise. The two different instrumental conditions show very close ATD profiles of each cytochrome C charge state. As expected, unfolding occurs as the charge state increases but the charge increment accelerates ion velocity at a given field strength, which results in shorter ATD at higher charge state. It is likely that the unfolded structure, by Coulombic repulsion, does not significantly increase the number of collisions with the buffer gas molecules.

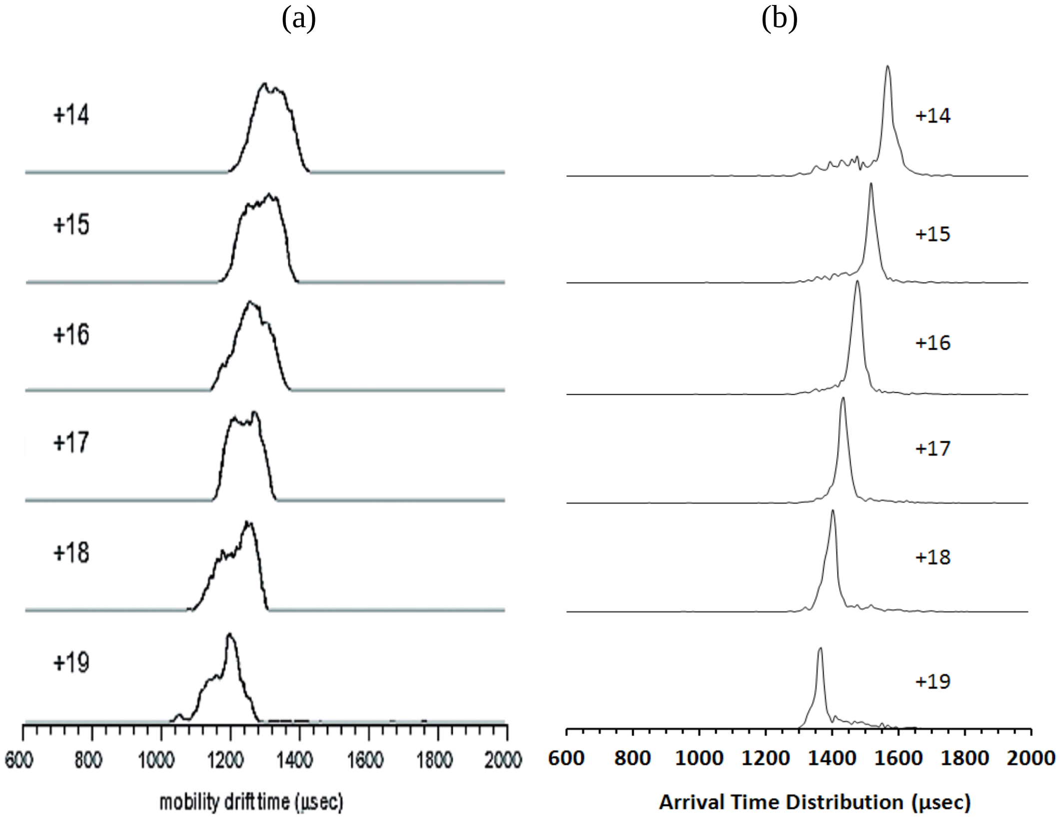

Figure 28. (a) Cytochrome C ATD profiles from the reference[9], adapted with permission from American Chemical Society, Copyright © 2010 and (b) the ATDs having the same charge states from this study.

For the lower charge states of cytochrome c, $[cyt+nH]^{n+}$ (n=3~8), the CCS data from other studies are close to the value calculated from the X-ray crystal structure coordinates (≃ 1339 Å^2)[58a, 85]. MD simulations of cytochrome c started from the crystal structure show linearly extended $[cyt+19H]^{19+}$ and partially unfolded $[cyt+9H]^{9+}$, which support the observations[5a]. However, by subtracting 10 protons from $[cyt+19H]^{19+}$, a partially refolded $[cyt+9H]^{9+}$ conformation is substantially more elongated than the partially unfolded $[cyt+9H]^{9+}$ started from X-ray structure even though the two structures have similar energies[5a]. A possible reason would be that conformational energy contours is very even in the range of intermediate charge states. Unfortunately we did not observe the charge states lower than [cyt+13H]$^{13+}$ at the given experimental condition but these results might be sufficient to support the ATD profiles compatible with the results from others for identification and charge-induced unfolding effect.

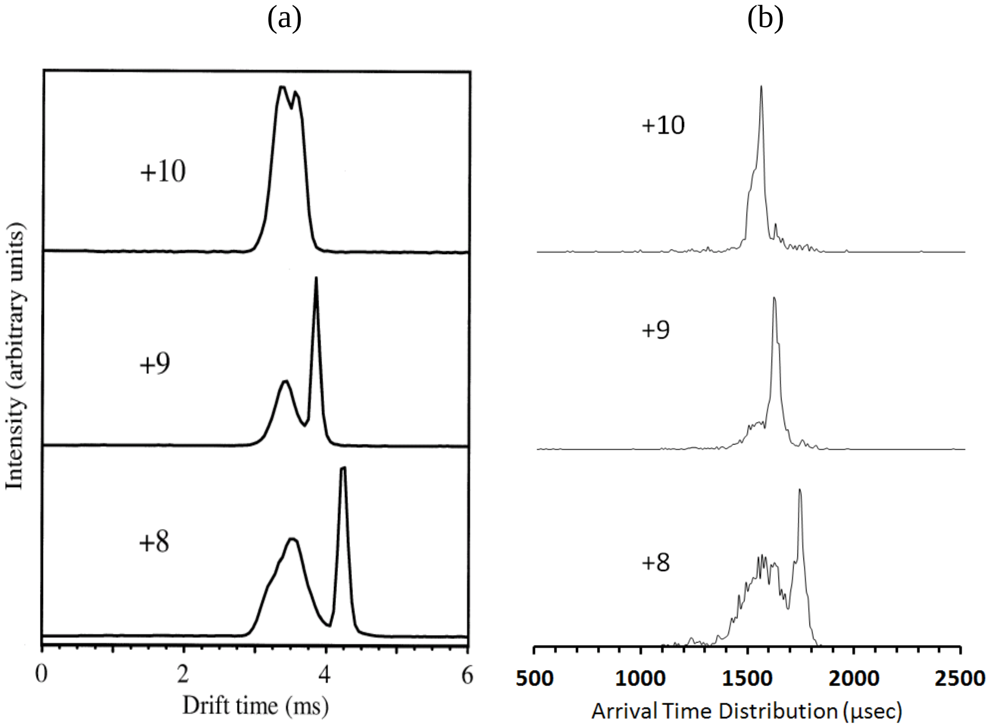

Figure 29. (a) Ubiquitin ATD profiles from the reference[94], adapted with permission from Springer, and (b) ATDs from ESI PFIG-MS having the same charge states.

Since the ATDs of cytochrome c are monotonic and the dynamics of the conformational change according to the charge state increase is not significant under the instrumental condition, it was necessary to compare another small protein having well known multiple conformations at particular charge states for compatibility of the instrument to observe a wide spectrum of conformational change. Gas-phase ions of ubiquitin have been studied extensively by Clemmer *et al*. using ESI DTIM-MS[58b, 95].

This small protein has at least two conformers of each charge state, especially from $[\text{ubi}+5\text{H}]^{5+}$ to $[\text{ubi}+13\text{H}]^{13+}$. The mobility profiles from the charge states $[\text{ubi}+8\text{H}]^{8+}$ to $[\text{ubi}+10\text{H}]^{10+}$ are compared with the reference in Figure 29[94, 96]. The ATD profile for $[\text{ubi}+8\text{H}]^{8+}$ shows a wide distribution ranging from 1200 μs to 1850 μs corresponding to CCS of 1097 $Å^2$ ~ 1630 $Å^2$. It has two dominant conformations with centroids of 1384 $Å^2$ and 1577 $Å^2$. In the case of $[\text{ubi}+9\text{H}]^{9+}$ and $[\text{ubi}+10\text{H}]^{10+}$, the ATD profiles also show a distinctive broad range of conformation distribution corresponding to the CCS of 1340 $Å^2$ to 1736 $Å^2$ and 1514 $Å^2$ to 1847 $Å^2$, respectively. The similarity between the ATD profiles using the instrument and ESI DTIM-MS in Figure 29 strongly suggests that PFIG is a compatible method to DTIM and the intermediate electric field strength (11~19 V/cm·torr) is efficient to complete ATD acquisition within a reasonable time (1min ~5 min) owing to the increased ion transmission. Since conformational changes at various solvent ratios for $[\text{ubi}+8\text{H}]^{8+}$ have been reported by Shi *et al.*[72], the minor differences in the ATD profiles might come from the different solvent composition that affects the non-bonding interactions which include hydrogen bonding and hydrophilic/hydrophobic stabilization between the backbone chain residues and solvent molecules. There is no direct evidence about the tertiary structures of gas phase ubiquitin ions. However, depending on their charge state and solvent composition, it is anticipated that the intermediate state and fully elongated state ("A" and "U") might exist in the ATDs of $[\text{ubi}+8\text{H}]^{8+}$ in Figure 29 but not the native state[72]. The intermediate state likely loses almost of its five-stranded β-sheet and seven reverse turns but still maintains α-helices along the backbone. Therefore, provided that the larger CCS reflects the unfolded ions, the observed two domains in the ATD profile of $[\text{ubi+8H}]^{8+}$ strongly indicates the transition of conformers from the native globular structure to the unfolded linear structure. This partially unfolded form that still maintains folded structural features is an interesting candidate for study of the folding/unfolding process by varying parameters. The dynamics of conformational changes from $[\text{ubi+8H}]^{8+}$ through $[\text{ubi+10H}]^{10+}$ obviously depends on the charge repulsion which drives the gas-phase ion structures to a narrow distribution at large calculated CCS values.

So far, the validation of PFIG by comparison of ATDs and CCSs from model peptides and proteins is successful using the correlation factor α and examination of charge-dependent conformational transition. Hence, the PFIG instrument can be used to validate the data from other instruments. Most of IM-MS instruments were in-house until 2006 when Waters Corporation (Milford, MA) launched the first commercial IM-MS Synapt®. The user-friendly interface and convenient instrument control have drawn tremendous attention for analytical needs. However, it requires complicated and rigorous calibration to obtain accurate CCS owing to adaption of a traveling dc pulse for ion propagation and rf confinement for high ion transmission, making the CCS calculations more complicated. Therefore, the ESI PFIG-MS provided validation of the data from a Synapt G2® instrument which showed up to 9 % difference in CCS when the calibration ions (+1), (+2), and (+13) to (+20) from cytochrome c were used for a series of phosphopeptides (data not shown). The difference might result from ion motions in rf confinement since the effective potential is enhanced by the number of charges in ions as similar as in PFIG. Without using traveling dc wave, the installation of rf confined drift tube with dc field gradient in Synapt® also shows lower correlation coefficient of calibration curve from a series of proteins having different charge states than from multiple charges of a single protein and the standard deviation of measured CCS using different calibrants are dispersed from ±2.5% ~ ±15%[80]. This result implies that careful selection of charge state and calibrant peptide/protein is important to minimize digression of the data. When MD simulations and other computational techniques are used to obtain detailed structures of gas-phase ion *in vacuo*, the precision of CCS calculated from ATD is critical since the empirical values are the criteria filtering the computed structural candidates of gas phase ions and normally it has the narrow range of ± 3%. The top three and the middle two phosphopeptides listed in Table 5 have the same m/z but differ in the phosphorylation site. The Ω values from ESI PF IM-MS and Synapt G2 matched well within ± 2.1 % difference.

Table 5. CCS of phosphopeties using PFIG-MS and commercial IM-MS Synapt G2®. CCS comparison between the PFIG instrument and a commercial ion mobility instrument shows ± 2.1 % difference.

Phosphopeptides (3+)	ESI-PFIG-MS[a]	G2[b,]	% Difference
	Ω (Å ^{2})	Ω (Å ^{2})	
APL(pS)FRGSLPKSYVK	379.5	382.2	0.7
APLSFRG(pS)LPKSYVK	362.3	369.9	2.1
APLSFRGSLPK(pS)YVK	366.8	365.9	0.2
APLSFLGSLPK(pS)YVK	380.6	381.7	0.3
APL(pS)FLGSLPKSYVK	380.0	382.0	0.5
APLSFRGSLPKSYVK	373.8	373.5	0.1

[a] α(+3)=0.766 used for calculation,[b] obtained by (+2) peptides calibration from Synapt G2 HDMS®.

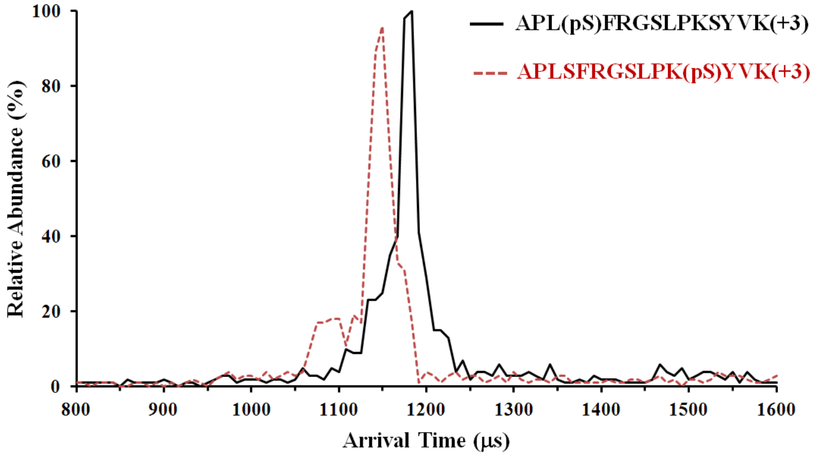

Figure 30. Superposition of the ATD for two phosphorylated peptides having (+3) charge state. The data were taken at 19.3 V/cm·torr (He). The CCS values for APLpSFRGSLPKSYVK (+3) and APLSFRGSLPKpSYVK (+3) are 379 Å ^{2} and 367 Å ^{2}, respectively.

In addition, from the superposition of the arrival time distribution of two peptides having the same m/z 563 but different phosphorylation site shown in Figure 30, the peptide ions can be separable up to 60% of their peak heights. The CCS difference of two conformations was *ca*. 3%. The result implies that varying positions of the phosphate group in peptides with the same sequence provides structural identities which might lead to characteristic interactions in the gas phase conformers between the phosphate group and charged amino acid residues. These results show the potential of using ESI PFIG-MS like other home-built DTIM-MS instruments. The advantages of IM-MS, which has the capability of separating ions having the same m/z based on conformational differences, cannot be overemphasized owing to the opportunities it provides for revealing crucial interactions in physiological molecules.

The potential for differentiating minor variations in CCS is important to provide a deeper understanding and accurate explanation of chemical phenomena. Although peptides and proteins are major candidates for exploration of conformational studies and intramolecular interactions affecting structural variations, their broad ATDs and peak shapes are not ideal to determine the precision of CCS from the instrument. Therefore, c(PG)$_3$ peptide with divalent metal ions were studied. The nonbonding interactions of carbonyl carbon with a metal ion are likely preserved during the ATD measurement and the CCS data are shown in Table 6. The variation of CCS among the three complexes is in agreement with the ionic radii of the metal ions since the effective ionic radius for Mg^{2+}, Ca^{2+}, and Cu^{2+} is 0.72Ǻ, 1.0 Ǻ, and 0.73 Ǻ respectively (crystal radii are 0.86 Ǻ, 1.14 Ǻ, and 0.87 Ǻ)[97]. The cage of c(PG)$_3$ might be expanded accordingly as the size of the ion increases. The experiment was performed in water: methanol (50:50, vol. %) and no protonated c(PG)$_3$ or fragmented ion was observed.

Table 6. CCS of metal complexes with c(PG)$_3$ by ESI-PFIG-MS. All measurements were repeated five times at each voltage setting and the percent relative standard deviation was less than 0.3%.

c(PG)$_3$ metal ion complex	PFIG-MS, Ω (Å ^{2})
[c(PG)$_3$+Mg]$^{2+}$	127 ± 0.41
[c(PG)$_3$+Ca]$^{2+}$	132 ± 0.21
[c(PG)$_3$+Cu]$^{2+}$	130 ± 0.52

Conclusions

The correlation factor α was established to link ESI PFIG-MS and ESI DTIM-MS results for CCS calculation. The factor is charge dependent and the results in comparison with other values are within ±4 %. Individual ATDs were also cross-checked by well known model peptides/proteins and they confirm the compatibility of PFIG-MS. Based on the characterization of PFIG-MS, validation of CCS from the commercial instrument was performed and the results were in ±2 %. Using the series of phosphorylated peptides, multiplication of the correlation factor facilitates the access to PFIG-MS for CCS confirmation with less acquisition time owing to high ion transmission. The precision of the instrument makes it applicable to small molecule studies, including metal ion complexation through non-bonding interactions.

CHAPTER VI

STUDY OF EFFECTIVE TEMPERATURE USING AN ELECTROSPRAY PERIODIC-FOCUSING ION GUIDE-MASS SPECTROMETER

Structural Elucidation and Ion Heating

Elucidation of 3D structure of proteins has a central role in biological chemistry and structural biology studies since the characteristic functional activities of proteins rely heavily on spatial conformations. Conventionally, the study of proteins employs spectroscopic methods including X-ray crystallography and NMR to determine solution and solid phase structures. These two techniques are realistic experimental tools which can provide the level of atomic resolution in current researches. Circular dichroism (CD) is complementary to X-ray and NMR in the determination of secondary or tertiary structures since CD spectroscopy responds to different solution conditions[98]. However, owing to the structural complexity due to the residues that contribute entire conformations through non-covalent interactions, and the difficulty to obtain crystals, the acquisition and interpretation of the experimental data are challenging to accomplish.

In comparison with the tools mentioned above, IM-MS can provide relatively simple and unique opportunity to identify ‘size’ and ‘shape change’ of peptide/protein ions from direct measurement of ATD. Assuming that gas-phase ions reflect their solution phase, and there are fairly strong results in support of this idea[21, 72, 99], IM-MS had opened another window for investigating protein/peptide structures with the development of soft ionization techniques (ESI/MALDI) in the 1980’s[100]. Owing to the fragile nature of protein structures, which involves non-covalent interaction and large degree of freedom, the elucidation of conformational changes from large protein ions using IM-MS is still extremely challenging or almost impossible. However, small protein/peptide ions which have less than 100 residues are relatively accessible for developing models that describe the folding/unfolding of real proteins with the aid of X-ray crystallography data as well as computational data which have been exponentially built up over the last three decades[101]. To shed light on the investigation of this topic using IM-MS, a valid starting point might be the stimulation of conformations by changing the different solvent composition through the use of varying ratios of protic/aprotic solvent as well as pH changes. These two factors might alter conformations of biological molecules in very subtle ways since the energy required to denature and break van der Waals/ hydrogen bonding/ hydrophobic interaction across the peptides and small protein ions is not larger than 10kcal/mol in solution phase (but enough to maintain functionality). As mentioned briefly in Chapter V, the solvent composition change is one of the prominent measures to identify the ATD shift in the case of ubiquitin (+8)[72] and similarly in bradykinin (+3) with at least 7 different conformers[21, 99].

Another method to activate folding/unfolding pathways is heating. After Anfinsen's demonstration of spontaneous ribonuclease refolding[102], the thermodynamic hypothesis stating that the three dimensional structure of a native protein in normal milieu should be the one having the lowest Gibbs free energy has developed into the energy-landscape theory leading to progress in structural prediction of proteins[103].

Owing to inherent instrumental requirements including the delivery of ions from an atmospheric source to the mobility cell in ESI IM-MS, it is possible to observe transition of conformations originated from ion heating. The possibility of heating ions has been recognized from early studies of ubiquitin by heated capillary temperature[95a] and a trapping time study with ion trap (IT)-IM-MS[58b]. This event might be an issue with any type of ESI IM-MS since all instruments share the three major components: (1) ion source interface, (2) mobility cell, and (3) mass analyzer interface where ion heating occurs from heat source for droplet evaporation, high electric field, and steep voltage drop. The ultimate goal of IM-MS instrumentation is to obtain ATD information from the native-like ions in gas-phase and the countermeasure of minimizing this adverse effect should be considered. However, if the phenomenon is well known and addressed adequately, then ion heating might help to understand the folding/unfolding process of gas-phase ions of peptides/proteins as well as to provide a chance to approach the energetic pathway for native-like conformations. In this chapter, the extent of ion heating is discussed in terms of effective temperature (T_{eff})[15b]. The causes of shifted ATDs include application of heated capillary temperature, rf amplitude in the IF interface, and the field strength of PFIG. The results are compared with the results from other instruments.

Experimental

Chemicals and Sample Preparation

Bovine ubiquitin (MW 8560) and bovine insulin (MW 5734) were purchased from Sigma-Aldrich (St. Louis, MO) and used without further purification. A 5 μM solution of bovine ubiquitin was prepared in water: acetic acid (AA) (99.99:0.01, vol. %) solvent to obtain dominant (+7) and (+8) charge states in the given ESI condition. A 15 μM bovine insulin solution consisted of 99% water and 1% AA. The two forms of the peptide substance P (c-terminus amidated, MW 1347.7 and free acid, MW 1348.7) were purchased from American Peptide Company (Sunnyvale, CA) and an 8 μM solution of the peptide was prepared using water: methanol: AA (49.5:49.5:1.0, vol. %) as solvent.

Instrument Conditions

The in-house ESI PFIG-MS was used to measure the ATDs from sample solutions. The entire PFIG length was 58 cm. The heated capillary temperature was varied from 40℃ to 90℃ for ESI droplet heating and the rf amplitude in the IF interface was set to 22~111 V_{pp}. The pressure and dc field inside the IF were maintained at 0.78 torr and 10V/cm without variation during the experiment. For the field energy heating experiment, the dc field in PFIG was changed from 10 V/cm to 19 V/cm at 1.8 V/cm step. All ATDs were measured at 1.0 torr of ultra high purity He (99.999%). Mobility drift time was determined by selecting a peak centroid which was not depleted at higher field strength. Ionwerks software (Houston, TX) was used for data acquisition and processing. The potentials after the PFIG modules and ion transfer optics were adjusted accordingly for each voltage setting by customized National Instrument LabView® software (Austin, TX). All measurements were repeated at least 3 times at the same condition and the relative standard deviation was 0.1%~0.5% for a given voltage setting. Mobility gating frequency was 200 Hz and the pulse width was 20 μs. The TOF MS calibrant was the (+2) and (+3) peaks from tryptophan zipper 1(MW 1606.8) and its pressure was ~1.8×10^{-6} torr. The extraction frequency by push-pull action was 20 kHz with 1.0 μs pulse width and the number of interleaving was 10.

Results and Discussion

As IM-MS instrumentation has progressed to an extent not possible before, recognition of ion heating has emerged by investigating the ATDs from different instruments using the same biological molecule[14b]. One of the molecules ideal for a model is ubiqutin for these two reasons: (1) it is a small protein having 76 amino acid residues without any cross-linking across the sequence which means that its conformers are susceptible to heating and (2) it has been extensively studied over the last 16 years using IM-MS. There is much literatures discussing the conformational shift of ubiquitin ions using IM-MS[58b, 84, 94-96, 104] but it is uncertain whether the smallest values of CCS from the 'coolest' condition on different types of instruments come from its native ion structures. Since PFIG utilizes higher electric field strength than other instruments having similar interface[5b, 36b, 57], the heating effect should be addressed by characterization of the devices.

Heated Capillary Heating

Owing to the guidance of the ion gas flume from atmospheric pressure and desolvation of solvent molecules from ESI droplets to efficiently generate more ions, the HC interface has been adapted in various ESI-MS and ESI IM-MS instruments[36b, 105]. Especially, the rf IF requires a directional flow toward in the acceptance area which is located at 1~5 cm (depending on the acceptance size of the rf IF and differential pumping design) away from the source inlet. From Chapter III, the residence time of gas flow entrained ions is estimated approximately to be hundreds of μs and thermal equilibrium between the capillary wall and gas flow depends on the number of collisions during this time span. If the pressure is assumed to be 100 torr inside the HC, the number of collisions would be $\sim 2\times10^8$ for an ion having MW 1000 and 500 Å^2 of CCS at 300 K. Thus thermal equilibrium between the HC and ions is likely to be established.

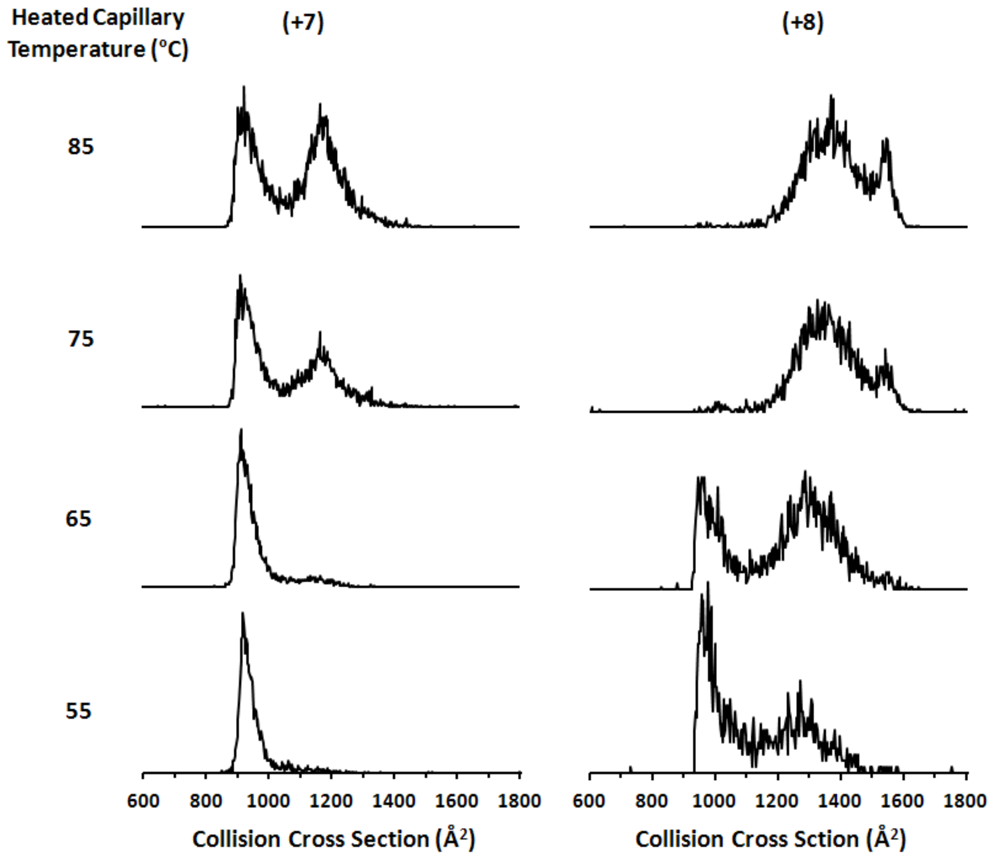

Figure 31. Ubiqutin (+7) and (+8) ATDs at different HC temperatures. PFIG electric field strength was 13.9 V/cm at 1.00 torr (He) and the rf amplitude of the IF was 65 V_{pp}.

The ATDs of pseudo-native ions from the instrument were compared to the results from Wyttenbach *et al*.[76] which used very similar ESI conditions as well as the rf

IF interface but a weak electric field in DTIM-MS. The ATDs from Li *et al.*[95a] might also be appropriate as reference for ubiquitin (+7) and (+8). The reason to pick (+7) and (+8) is that the structure of a gas-phase ion starts transition from the reference[76]. More interestingly, these two charge states are anticipated to show different behavior, that is, (+8) is likely more vulnerable to heat from increased charge repulsion than (+7).

As seen in Figure 31, the temperature increases the population of large CCS conformers. In the case of (+8), the shift of CCS consists of three domains (folded, partially folded, unfolded) and shorter arrival time conformers were depleted earlier than (+7), which indicates that (+7) is more resistive to conformation change. The three domains of (+8) were also observed in the reference using solvent composition change[72]. However, the early study shows only two domains in (+8) and the first domain (930~1050 Å^2) is not shown even at low temperature (25℃), while the population of the second domain of (+7) at 25℃ is more abundant than in this study [95a]. Although the calculated CCSs show excellent agreement with the second domain of (+7) and the two other domains of (+8) in this study, the initial state of ions before mobility injection might be denatured by acetonitrile dominant solvent since (+7) in a water dominant solvent shows an ATD that is very close to the first domain of (+7) from PFIG. Another reason might be the ion channel. To transfer ions against the counter-flow coming out of the DT requires a stiff voltage drop within a short distance (~ 3cm) and results in collisional heating[4b]. The low charge state ions of ubiquitin (+6 ~ +9) show very interesting features of conformational transition as the HC temperature increases, whereas the high charge state ions (+10 ~ +13) do not give significant shifts and population variation (data not shown). By predominant electrostatic repulsion among the charges, largely unfolded conformers would not be affected by the HC temperature. In the case of a small peptide, the transition may not accompany drastic conformational variation as similar to that of highly charged states of a small protein since the resolution of IM-MS would not be high enough to indicate the difference. Overall, the results support that (+7) is the highest charge state which upholds the conformations close to pseudo-native structure and (+8) is sensitive to temperature change, and starts unfolding rapidly. Besides, according to the calculated CCS (averaged hard-sphere projection) from the X-ray crystal structure of ubiquitin (~897Å^2)[95a, 106], the measurement is very likely to indicate that the conformers of gas-phase ions at "cool" conditions of PFIG-MS represents the lower funnel region at the energy landscape of protein folding.

Ion Heating in the rf IF

Ion motion in an inhomogeneous rf electric field results from a large number of collisions between ion and neutral gas molecules under pressurized cell (0.1 mtorr ~ 3 torr). These collisions lead to a heating/cooling effect of ions by accumulation/loss of energy from collisions[107]. Douglas and French reported an rf only quadrupole for a collisional focusing device in a certain pressure range (0.5~10 mtorr) with ion injection energy of 1~30 eV at 1.0 MHz and found less axial kinetic energy at the end of the quadrupole ("cooling")[33]. This can be interpreted as collisional dampening of ion motions to the center axis and slowing ion down by collisions. Theoretical calculation of the final kinetic energy distribution of ions shows an excellent agreement with the actual stopping curves after traveling the length of the rf quadrupole using simple Monte Carlo models assuming elastic hard sphere collision[33]. However, high injection energy is not recommended in this setup since it might increase kinetic energy which could induce energetic collisions to scatter ions, escape from pseudopotential barriers of the quadrupole, or fragmentation ("heating"). Thus, cooling/heating by only rf field under uniformly filled gas is highly conditional and depends on gas pressure, traveling distance of ions, amplitude and frequency of rf potential, bath gas type, and initial ion kinetic energy. "Thermalization" of ions (or achievement of thermal equilibrium of ions with bath gas) is the balance in which all these factors are involved between acceleration before collisions and relaxation after the collision.

For the estimation of the heating effect by rf, it would be convenient to simplify the case as a collision between a mono-atomic bath gas with an ion (for example, one that is 100 times heavier than the gas molecule and singly charged). The energy exchange in each ion-neutral collision is affected by these two factors: (1) the characteristic internal energy distribution of ions and (2) the center-of-mass (CM) kinetic energy depending on the collision partner (gas molecule). Since the internal energy of ions can be estimated using the CM energy of the collision and the internal energy distribution is relatively insensitive under low energy collisional activation[108], acceleration of ions by the rf field in gas which induces ion heating by collision can be analogous to heating the bath gas for shifting the thermal equilibrium to higher temperature. The mean kinetic energy (thermal energy) of the gas molecule is $3/2kT$ and assuming an ion (v_i, m_i) colliding with the gas molecule (v_g, m_g) in thermal equilibrium, then the CM collision energy is as follows

$$E_{CM} = \frac{\mu\langle \boldsymbol{v_r}^2\rangle}{2} = \frac{\mu\langle v_i^{\,2}\rangle}{2} + \frac{\mu\langle v_g^{\,2}\rangle}{2} = \frac{3}{2}kT \tag{6.1}$$

where μ is the reduced mass and $\boldsymbol{v_r}$ is the relative velocity of the two particles, the brackets mean average and the derivation of the equation considers that the scalar product of two vectors is zero if one vector has random orientation[107b]. Since the ion travels under rf, the effective potential approximation (V^*) can estimate the kinetic energy of the ion depending on radial position r from the center of the ring electrodes[35b],

$$V^*(r) = \frac{q^2E(r)^2}{4m_i\omega^2} = q\cdot\frac{qE(r)^2}{4m_i\omega^2} = [C][V] \tag{6.2}$$

As explained in Chapter II and III, $E(r)$ is a given local rf field intensity, m_i and q is the mass and charge of the ion, respectively, and ω is the angular frequency of the applied rf. This effective potential plays the key role to focus ions on the central axis in the rf device. Note that the unit of the effective potential is energy (J) and the right side of the equation which is separable from the charge represents voltage (V) related to the actual rf amplitude. Time-dependent radial motion of the ions in inhomogeneous rf field is the superposition of a smooth drift term and rapid oscillating motion affected by the amplitude [V]. When the adiabaticity condition is satisfied, the kinetic energy of both motions can be transferred into effective potential energy[35b], which implies that the kinetic energy of the rapid oscillation motion at a local point can be written as

$$E_{i,RF} = \frac{1}{2}m_i\langle v_{i,RF}^2\rangle \simeq V^*(r) \tag{6.3}$$

where $v_{i,RF}$ is the instantaneous velocity of the ions from rf oscillations and $E_{i,RF}$ is averaged over a single rf period. Provided that the drift motion (or secular motion) of the ion is very slow compared to the rapid oscillating motion ($v_{i,s} \ll v_{i,RF}$), then the total ion kinetic energy is

$$E_i = \frac{1}{2} m_i \langle v_{i,s}^2 \rangle + \frac{1}{2} m_i \langle v_{i,RF}^2 \rangle \simeq \frac{q^2 E(r)^2}{4 m_i \omega^2} \tag{6.4}$$

And substitution of the $\langle v_{i,RF}^2 \rangle$ to the equation of E_{CM} (6.1) above gives

$$T \propto \frac{q E(r)^2}{4 m_i \omega^2} \tag{6.5}$$

Therefore, at the same condition, the increment of the rf amplitude results in the increase of the ion temperature. The heating effect by the rf amplitude is shown in Figure 32. Again, the (+7) charge state is more resistive to the rf heating compared with the (+8). The field gradient force normally pushes the ion away from the electrode surface to the

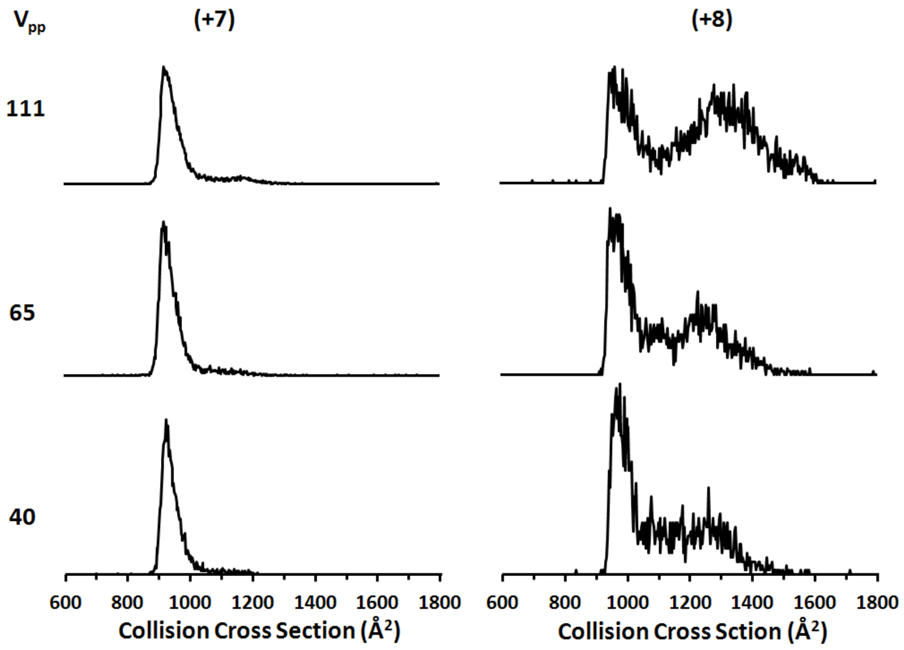

Figure 32. Rf heating from the (+7) and (+8) charge state of bovine ubiqutin with PFIG field strength of 13.9 V/cm at 1.00 torr (He) and the HC temperature 55℃.

center axis (weaker field) since the ion feels large effective potential when it is close to the electrode. In the case of ion packet in the rf IF, charge repulsion among ions might push ions toward the electrode. The increased *r* makes the situation worse, resulting in the ions having a higher temperature than that of the gas if they do not dissipate kinetic energy buildup by the effective potential. Thus, the ion heating by the increased rf amplitude is likely to occur at the end of the IF owing to the narrow tapered region. To the best of my knowledge, there is no result directly reporting the IF heating effect in ATD measurement. Modification of the IF might help to attenuate the heating with the aid of a drift region after the tapered region which allows the ions additional collisions before they enter to the mobility cell. With careful attention to operational conditions, the extra drift motion might cool down the ions and maintain the focusing effect by employing a multipole ion guide.

Injection Energy Heating

After ions pass through a differential region from the ESI source, focusing or accumulation is achieved by simple ion optics or ion trap (IT) and the ions are injected into the mobility cell against the counter-flow of the buffer gas. If a multipole rf ion guide is used for this purpose, operation parameters may affect the pressure inside of the guide. The collisional heating during the process can explain the ATD shift at different injection energy in IM-MS as reported by Valentine *et al*[84]. Injection efficiency may increase when the voltage gap between the last focusing electrode and the entrance electrode (or a gate electrode) of the DT is large, but the heating is increased since the kinetic energy of ion is high. The small voltage drop across the region would heat ions less but injection efficiency would be low against the counterflow. During the experiment in this study, 8~10V drop across the region between the ring and the gate electrode was maintained in the current PFIG-MS and the ATD shift was not observed within the voltage drop (data not shown). Note that the motion of ion during the transmission follows the direction perpendicular to the equipotential line developed around the aperture which would be contoured and fringed, not straight, by distortion of the electric field originated from the shape and size of the apertures. Owing to the He counterflow, ions would not pass through the center of the aperture but around the edge where the flow is weak. Poehler *et al.* showed the CFD result with the combination of particle image velocimetry from a counterflow condition of an atmospheric pressure ionization source where analytes enter around the edge of the sampling cone[109].

Mobility Field Heating

If the field intensity is raised to a level at which the ions acquire excess energy appreciably larger than the thermal energy of the gas molecules, two types of motion are enhanced by the drift field: (1) a directed component accelerated along the field and (2) a random form by collisions representing converted energy acquired from the field. The diffusion of the ions is affected by these motions and perpendicular diffusion to the field direction takes place at a rate different from the diffusion in the electric field direction. The Einstein equation cannot be used to explain different behaviors of diffusion in this case and the ion mobility K is no longer linear as the electric field increases. The velocity distribution of the ions becomes distinctly non-Maxwellian since the average ion speed depends on E as well as T at higher fields. The mean speed is changed by increased field acceleration and the mean collision distance (we assume binary collision) is inversely proportional to E under a constant N. Therefore fast moving ions experience more collisions than slow ions.

The theoretical background for ion mobility, the momentum-transfer theory, is based on the consideration that the energy and momentum from the field should be at steady state and balanced by collisional losses to achieve the drift velocity (v_d). By assuming that all collisions are elastic, the average ion energy is defined by[15b]

$$\frac{1}{2}m_i\langle v_i^2\rangle = \frac{1}{2}m_g\langle v_g^2\rangle + \frac{1}{2}m_i v_d^2 + \frac{1}{2}m_g v_d^2 \tag{6.6}$$

For gas-phase ions of large biological molecules ($m_i \gg m_g$), ions have most of their energy as drift motion. From the definition of relative velocity in the CM coordination, the mean relative energy equation gives

$$\begin{aligned}\langle E_{rel}\rangle = \frac{\mu\langle {v_r}^2\rangle}{2} = \frac{1}{2}\mu\,\langle(\boldsymbol{v_i} - \boldsymbol{v_g})^2\rangle = \frac{1}{2}\mu\langle v_i^2\rangle + \frac{1}{2}\mu\langle v_g^2\rangle \\ = \frac{1}{2}m_g\langle v_g^2\rangle + \frac{1}{2}m_g v_d^2\end{aligned} \tag{6.7}$$

The first term of the right side is $3/2kT$ and the second term represents the random part of the field energy. Since the mean relative energy corresponds to the energy of the ion gained from the field, the effective ion temperature (T_{eff}) which indicates the deviation of the random ion energy from the thermal equilibrium by the additional field dependent factor can be written as

$$\langle E_{rel}\rangle = \frac{3}{2}kT + \frac{1}{2}m_g v_d^2 = \frac{3}{2}kT_{eff} \tag{6.8}$$

Therefore, the increase of the mass of the collision partner (or the field strength which leads to the increase the drift velocity) can achieve the same effect of heating the ion by the temperature increase. It is obvious that higher drift velocity induced by higher field strength changes the collision frequency at a given pressure and the mobility begins to vary, which leads to the onset of non-linear behavior. Thus, it is recommended to perform CCS measurements below the low field limit defined by

$$\frac{1}{2} m_g v_d^2 \ll \frac{3}{2} kT \tag{6.9}$$

The velocity acquired just before a collision depends on the collision period and the energy obtained from the field is inversely proportional to the number density. To minimize the energy gain from the field, the increment of the pressure might be considered. From the definition of the drift velocity ($v_d = K \cdot E$) and consideration of the charge state (+1) at 300 K, the criterion is defined as

$$\frac{E}{N}\,(\mathrm{Td}) \ll 0.78 \left(\frac{m_i}{m_i + m_g}\right)^{\frac{1}{2}} \Omega\ (\mathrm{\mathring{A}}^2) \tag{6.10}$$

where 1 Td = 10^{-17}V·cm^2 and Ω has the unit of 10^{-16} cm^2 for simplicity of the calculation[15b]. Note that the low field limit increases as the CCS increases and the criterion is originated from the elastic hard-sphere collision, which is likely to be appropriate for the cases of atomic ions. Owing to the internal degree of freedom and ion-neutral interaction potentials, the low field limit is difficult to specify and is estimated from empirical CCS values. For example, the field strength less than 2~4

V/cm·torr in the case of an ion having CCS ≃ 50Å^2 with (+1) charge satisfies the condition. In the case of multiply charged ions, the field limit is

$$\frac{E}{N} < \left(\frac{m}{m+M}\right)^{\frac{1}{2}} \frac{d^2}{q} \tag{6.11}$$

where *d* is the sum of the radii of ion and neutral species and *q* is the number of elementary charges on the ion[12]. By considering the charge states of ubiquitin ions in this experiment, the minimum field strength needed for maintaining high ion transmission by PF is larger than the low field limit and it is critical to examine the conformer population shift by

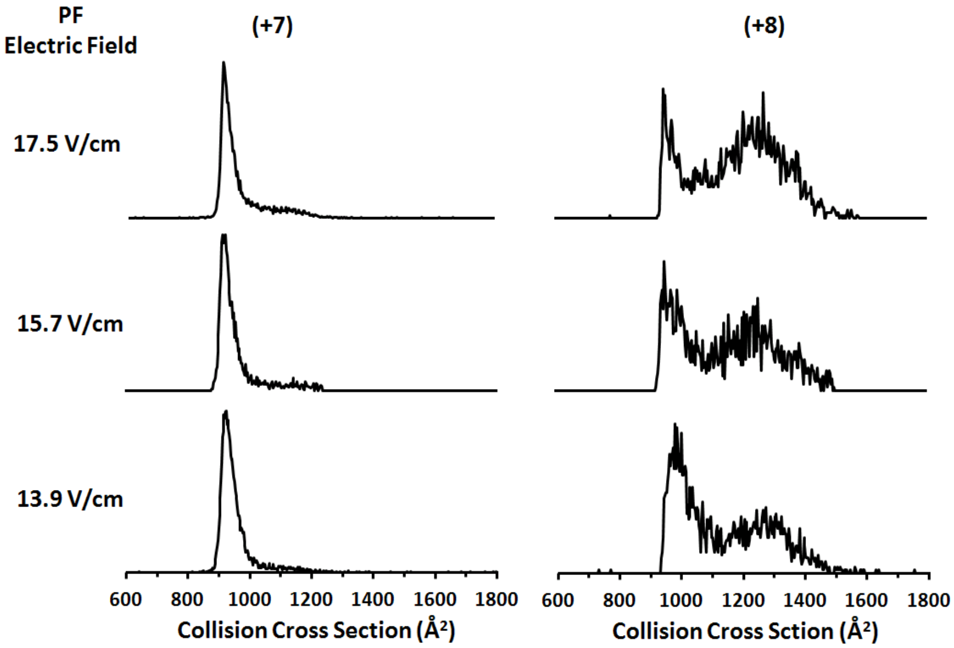

Figure 33. ATDs from the (+7) and (+8) charge state of bovine ubiqutin at various electric field strength in PFIG at 1.00 torr (He) with rf V_{pp} 65 in the IF and the HC temperature 55℃.

field strength variation for versatility in the application of the instrument. From the results presented in Figure 33, the higher field strength accompanies the increased conformer population of larger CCS as anticipated from the effective temperature theory. Although the ATDs were shifted at high field, the extracted peak centroid on the left in both (+7) and (+8) ions did not vary much (less than 0.3% of the relative standard deviation) and allowed it to be used as the out-of-drift tube time measurement for calculation of CCS in the given condition. As shown in the heating by rf amplitude and temperature, the (+7) charge state is more resistive than the (+8). The ATD profiles in Figure 33 are also very similar to the other studies, which confirm that the heating effect by various sources can affect the ATDs.

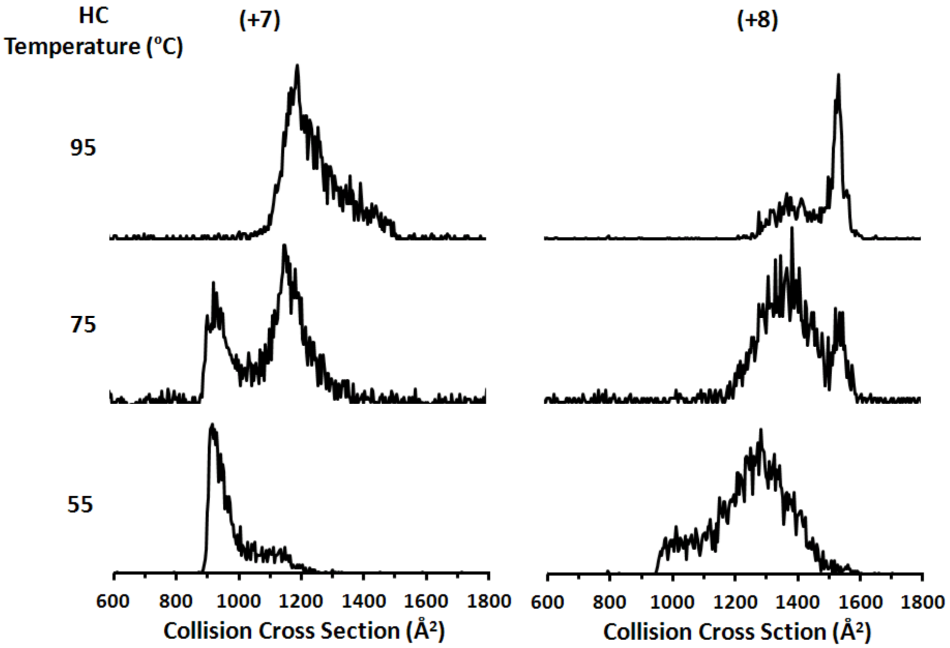

Figure 34. Synergetic heating effect of the ubiquitin (+7) and (+8) at different HC temperature with high field strength (19.3 V/cm) in PFIG under 1.0 torr (He) and rf 65 V_{pp} in the IF.

In high injection energy heating and denaturing of aprotic/protic solvent composition[72, 84, 95a, 96], both (+7) and (+8) charge states exhibit three domains during the unfolding process. The synergetic effect using a combination of the heating parameters can also lead to more extended conformers in gas-phase. Thus, the ATDs were measured at increased field strength of 19.3 V/cm and in the temperature range of 55℃ to 95℃. The data is shown in Figure 34. At 95℃ with 19.3 V/cm, (+7) shows complete depletion of the first conformer domain on the left side and the emerging conformers at ~1410 Å^2, while (+8) reveals similar depletion at lower temperature (55℃) and starts convergence of the conformers to a narrow late ATD on the right side indicating the third domain (~1550 Å^2) from 75℃. This result reconfirms that DTIM using a weak electric field and PFIG at intermediate field less than 17.5 V/cm·torr are sufficiently compatible in ATD

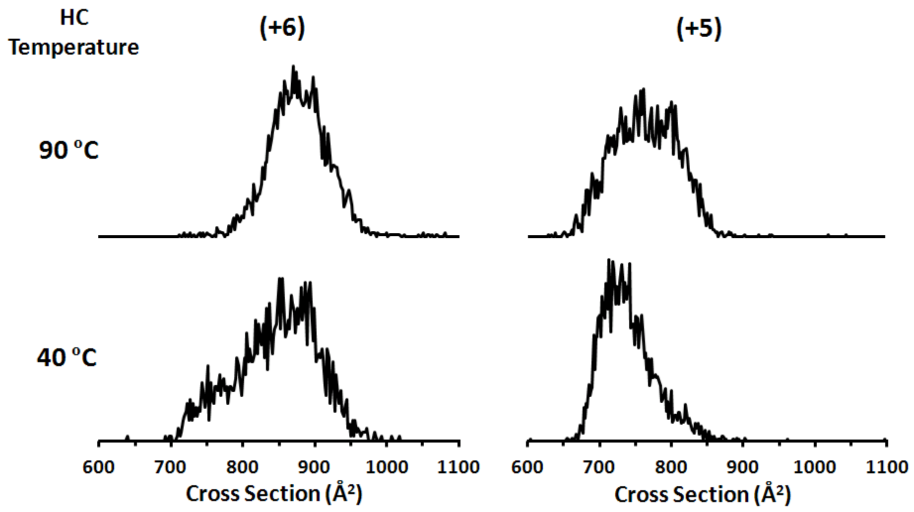

Figure 35. HC temperature change triggering conformational changes of gas-phase ions from insulin (+5) and (+6) charge state. Insulin solution consists of 99% water and 1% acetic acid. Bovine insulin (MW 5734) 15 µM at 1.0 torr He and 13.6 V/cm with rf V_{pp} 64.

measurements. In the case of small peptide ions, the ATD shift may be more susceptible to heating with small change of the field, rf amplitude and the HC temperature than large protein ions since the conformational variation may require less energy per ion. However, the drastic changes in the ATD from small peptide ions have not been observed through the instrument except for alteration of the peak shoulder depending on the experimental parameters (data not shown). It is likely that the resolution of the current instrument is not sufficient to resolve the minor variation in ATD. Deconvolution might be useful to extract structural information from the low peak-to-peak resolution ATD data with MD simulations based on experimental CCS values[110].

Since ubiquitin has no internal cross-linking among amino acid residues, the unfolding process of ions from compact globules to elongated structures might occur freely without internal restriction. If gas-phase ion conformers reflect their original structures, rigid conformers having intramolecular disulfide bonding would be resistive to the heating effect and the alteration of ion structure. The identification of structural rigidity using IM-MS can also provide alternative methods to investigate energy resolved structural changes in gas-phase ion, which help to understand moieties involved to stabilize conformers and energy landscape in the folding process. Insulin is an adequate example having two disulfide bonds across chain A(21 amino acids) and chain B (30 amino acids)[111]. The (+4), (+5) and (+6) charge states are dominant in acidified ESI conditions and other various conditions[112]. From the experimental conditions, the ATD of (+5) and (+6) were measured and the heating effect from the HC was prevalent over other parameters (Figure 35). Compared with ubiquitin, insulin (+5) and (+6) did not show substantial changes in collision cross sections as the heated capillary temperature increased. Instead of shifting the width in the ATD profile to larger CCS, the depletion of smaller conformers and increase of larger conformers are noticeable in both cases. Therefore, the crosslinking between chain A and chain B of insulin might restrict the degree of freedom for unfolding at high temperature and a cyclic structure is maintained. The possible conformational changes would be the untwisting of the two chains by losing non-bonding interaction with unbound moieties of the amino acid residues beyond the cysteine-cysteine sequences. The insulin (+3) and (+4) CCSs from traveling wave IM-MS experiments are 757 $\acute{Å}^2$ and 772 $\acute{Å}^2$ respectively[113] and the reference CCS for (+5) and (+6) are not available. However, considering the peak centroid and charge repulsion, the CCS in Figure 35 is likely acceptable (6~11 %).

With the advance in instrumentation, it has been more important to discuss whether measured states are native-close[14b], rather than the precision of single CCS values. Since the Mason-Schamp equation includes several assumptions and approximations with empirical data[15b], it would be appropriate that the CCS from the equation is assumed to be “calculated” not directly “measured” and it absolutely depends on the ATD which is influenced by ion-neutral interactions, which are not considered in the derivation of the equation. The conversion errors from the ATD to CCS is also obviously noticed when the formula converts very short arrival time to CCS owing to the out-of-drift cell time which should be subtracted from the arrival time, resulting in negative CCS values. This can be overcome by shortening as much as possible the time spent by ions after the mobility cell through improvement of the instrument. However, in spite of the aforementioned limitations, the calculated CCS from recent results for gas-phase ions from lower charge states of peptides and proteins are very close to the CCS from X-ray crystallography and/or NMR data, which indicates comparability of the technique with other structural resolving instruments.

As the investigation of the effective temperature reveals that CCS can be changed by conditions, it is useful to study how “hot” or “cold” the ESI process is. Recently, our group found that the (+3) charge state of substance P, RPKPQQFFGLM, has two

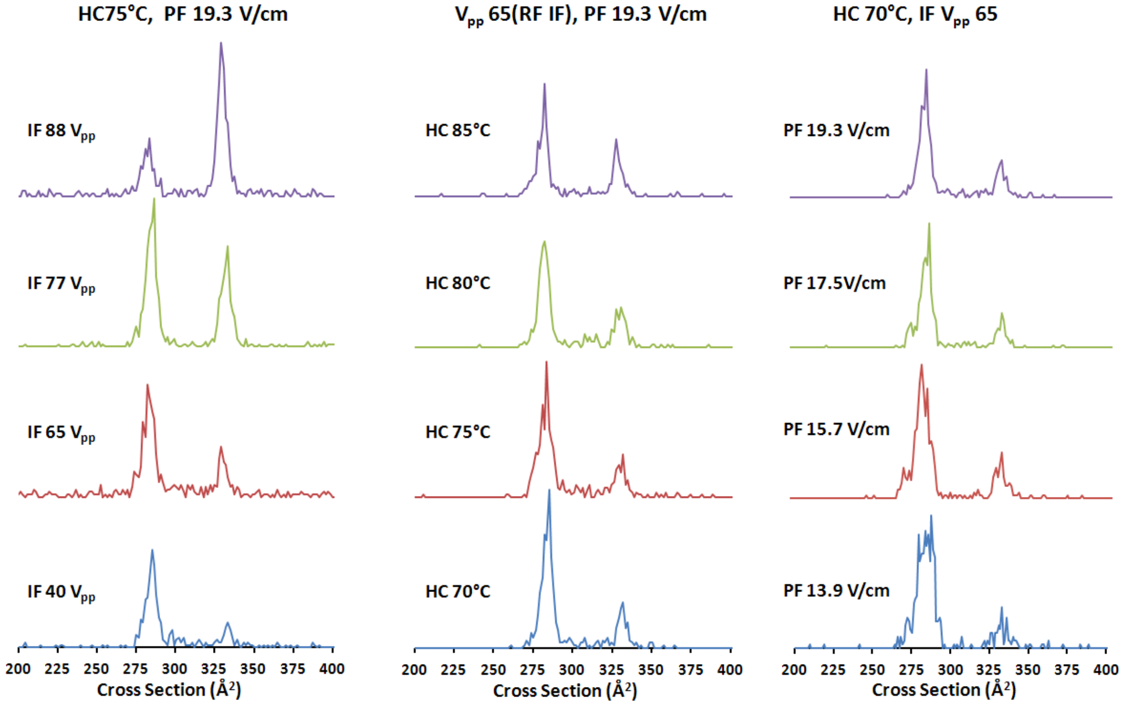

Figure 36. CCS profiles of substance P (+3), RPKPQQFFGLM (MW 1347) amidated c-terminus, at various rf V_{pp}, HC temperature, and PFIG electric field strength. The concentration of the solution was 8 μM in Water: Methanol: AA (49.5:49.5:1.0, vol. %) and PFIG was at 1.0 torr He pressure.

distinctive mobility profiles (form A, form B) and their relative abundance is changed by various interface conditions. The result was reproduced using ESI PFIG-MS and the data is shown in Figure 36. When the field strength is changed from 13.9 V/cm to 19.3 V/cm, the change in the relative abundance of form A and form B is not significant, while the rf amplitude in the IF and the HC temperature are noticeable. The most remarkable outcome is the rf amplitude change which causes a complete inversion between the two profiles. Since the rf heating effect is associated with the ion introduction to the instrument and the HC temperature also exhibits an increase in form B, the two profiles are likely engaged with local minima in the energy profile of conformers when the ions are generated from ESI source. Multimeric conformations were examined by other high resolution MS at the same ESI condition (data not shown) and both forms were identified as a monomer. Hence, using a modified sequence the experiment can help to understand fundamental gas-phase ion structures since the conformational energy barrier is controlled by various factors including steric hindrance and available non-bonding interactions. Thus C-terminus free acid form was also tested for the conformational transition by the interaction of carboxylic acid end with other

Table 7. Substance P (+3) CCS results at various rf amplitudes in the IF. The C-terminus of the sample peptide was amidated (-CONH$_2$).

RF V_{pp}	Substance P (+3), C-terminus amidation	
	Form A, Ω (Å^2)	Form B, Ω (Å^2)
40	281 ± 0.2	331 ± 0.3
65	284 ± 1.1	336 ± 0.7
88	286 ± 0.4	337 ± 0.3

residues along the backbone. The ESI condition was constant and the carboxylic and carbonyl oxygen were expected to be closer to the protonated N-terminus arginine and lysine than the C-terminus amidated form. However, the CCS of form A and form B are 279 ± 0.6 $Å^2$ and 337 ± 0.9 $Å^2$, respectively, which means that the generation of the two different forms is likely to be independent of the interaction between N-terminus and C-terminus when compared with the result in Table 7. The results urge the investigation into the variant of one residue among the backbone that provides significant changes in the ATD profiles. One of the approaches, owing to two proline residues along the backbone, is to look into cis-trans structural isomers having low energy barriers (< 10kcal/mol). For better explanation of the phenomena, MD simulation is on-going to reveal the candidate structures and allows us to evaluate the significance of the individual contribution from each residue interaction. Based on our cryogenic IM-MS data showing that form B does not follow the hydration trend-line (data not shown), desolvation MD simulation is now in progress to provide the trace for the ESI process that ends up with the conformers having corresponding CCS.

Conclusions

IM-MS provides the window for peeping into conformational transitions of gas-phase ions and PFIG-MS has been tested for compatibility with conventional uniform field DTMS using various operational conditions and ATD measurements. However, in both cases, care must be taken to minimize ion heating. The expected level of performance of ESI PFIG-MS is achieved by delivering high transmission of ions through characteristic PF design and monitoring conformational changes from the native-like to the unfolded/fully extended. So far, the resolution of IM-MS cannot defeat the atomic resolution of X-ray crystallography. However, simple and fast acquisition of the configuration of gas-phase ions as well as the capability of observing the ATD shift in real-time at various conditions can be of benefit in the area of elucidation of the development of low energy conformations of gas-phase ions and functional characteristics in biological molecules.

CHAPTER VII

CONCLUSIONS AND FUTURE DIRECTIONS

The development of IM-MS using PFIG as a mobility cell with ESI source is ultimately aimed at its application for the characterization of peptide/protein ions in gas-phase. In fulfillment of this goal, this research has focused on two main areas: (1) implementation of high transmission high resolution IM-MS by hybridization of an rf IF and PFIG to a home-built TOFMS, and (2) specification of operation conditions and application results in comparison with conventional DTIM-MS results. Our research group has previously explored the benefit of high transmission in a mobility cell using a MALDI source. To maximize the benefit of high transmission in PFIG with an ESI source, the home-built rf IF was coupled to the mobility cell and the simple auxiliary ring electrode with the ion-gating aperture design was adapted to overcome the counter flow from the mobility cell. SIMION 8.0 ion trajectory calculation was used for all design and implementation of each section to increase ion transmission. The gas loading was improved by the differential pumping at both ends of the mobility cell. Since the elevated pressure inside the mobility cell is critical in preventing buffer gas contamination by the intruding air from the source and enhancing the focusing afterward, the gas loading was improved by adaptation of differential pumping at both ends of the modular PFIGs. The ion transfer optics was modified to the three long cylindrical electrodes system with 2.0 mm i. d. skimmer separating differential pumping from the ion transfer optics attached to the TOF MS. A significant enhancement of ion focusing (~60-fold increase after the rf IF at the rf amplitude of V_{pp} 111) was noted in the case of BK1-8 ions from the ion current measurement. Using c(PG)$_3$ complexes with Ca^{2+} metal ion, the transmission across the entire instrument was also tested and the total ion count responded to the rf IF amplitude change (~35 fold increase). In spite of the disadvantage of using an ESI source, from which a continuous ion stream is pulsed, the data acquisition time required for a reasonable signal-to-noise ratio(>70) was less than ~ 5 min. In the case of cytochrome c with 1 μM, it was less than 2 min. The current instrument resolution at 19.3 V/cm·torr (He) is ~56 in the case of tryptophan zipper 1(+3) and somatostatin (+3) ions, which is acceptable for measuring ATDs from multiply charged ions.

In terms of the application for investigating CCS of gas-phase ions, however, distinctive motions of ions in PFIG need to be carefully considered in the conversion calculation from measured ATD. Additional motions except the axial drift motion increase the ion traveling time in the PFIG mobility cell. From the data available in the literature, adaptation of the charge-dependent correlation factor ("damping factor") was shown to successfully integrate the gap between DTIM and PFIG. However, although the CCS values are close enough to validate PFIG-MS (within ±4 % difference), comparison of the ATD profiles from extensively studied gas-phase ions of proteins and peptides are essential to evaluate if this technique is on par with other contemporary techniques including a commercial instrument widely used. Along with BK (+2), the individual charge states of horse heart cytochrome c (+14 ~ +19) and ubiquitin (+8 ~ +10) show excellent agreements with the previous results from other groups using

DTIM-MS. The precision of the measurement and differentiation for small CCS change of ions are supported by results from the phosphorylated peptides (+3) and c(PG)$_3$ complexes with (+2) charge state metal ions at the intermediate electric field strength (10 V/cm ~ 20 V/cm) under 1.00 torr He.

As investigated in DTIM and ESI-MS/MS, ion heating during the mobility experiment occurs at high field in the mobility cell or increased HC temperatures using ESI PFIG-MS in the case of ubiquitin (+7 ~ +8) and of substatnce P (+3). Intriguingly, the rf heating inside of the IF interface is noticeable when the amplitude is over 65 V_{pp}. This has not been reported from other research groups using a similar rf IF interface coupled to an ESI source. It is likely due to the end of the tapered IF region where ions are strongly encountered by gas molecules and rapidly increasing effective potential. This additional feature might provide a tool for observing conformational transition following an energetic pathway leading to an unfolding process, while the “cool” condition in the current instrument is capable of delivering CCS values close to native-like gas-phase ions confirmed by other techniques including X-ray crystallography and NMR. However, since IM-MS does not have atomic resolution so far, MD simulations and other computational methods are necessary to understand the interactions among the residues in peptides and proteins which impinge on fundamental changes in conformations.

Advanced instrumentation in IM-MS is a critical and sound foundation for unveiling and accelerating the progress in various disciplines related to structural functionality of biological/chemical molecules. Notably, after development of IM-MS with different type of soft ionization techniques, its application has been stretched out from hard singly charged inorganic ions to soft large proteins over 100,000 Da with the advantages of simplicity, speed of analysis, and sensitivity over other approaches[114]. Although, the current IM-MS instrument has improved transmission, higher mobility resolution and mass resolution will benefit studies on detailed conformational transitions at various solution conditions that address the aggregation of peptides and proteins[8].

Energy-resolved IM-MS is likely applied to track down the energy landscape of protein folding/unfolding and provide a practical solution for misfolding of proteins[115]. The implementation of the technique requires the control of the heating effect from the instrument when ions are introduced to the mobility cell and the cold condition in which it is easy to observe native-like conformers from mimicked physiological solution. The three sources of ion heating discussed in Chapter VI should be specifically defined to acquire the van’t Hoff plot at different temperatures and the Arrhenius plot. For example, for substance P, if the ion residence time in the HC is measured using pulsed ion generation and detection at different temperatures, the kinteics between well resolved peaks can be calculated. The deconvolution technique can be used to resolve the varied population of different conformers and according to the variation of CM energy at single-collision condition, sigmoid curves can be obtained by integration of a decreased/increased conformer profiles[116]. Using a curve fitting method from the single-collision results, the conformational energy difference can be calculated in case of small peptide ions with a well-designed collision cell which can adjust the collision energy with high resolution and reduce ion loss by scattering.

Studying the factors that determine conformations of the gas-phase ion is another area for the application of this instrument. Charge repulsion and heating are the most influential driving forces in the unfolding process. However, as mentioned in Chapter V, the results using MD simulations by subtracting certain charges from the higher charge state to reach the lower charge state conformers does not show the same geometry started from X-ray crystallography data. Investigation of the conformational change after charge reduction and oxidation is anticipated to answer this question. Also, ESI PFIG-MS is applicable to elucidate the mechanism of the controlled charge state of peptides using an rf tube[117] or the environment of an ESI process that accompanies conformational changes.

REFERENCES

1. Bowers, M. T.; Marshall, A. G.; McLafferty, F. W., Mass spectrometry: Recent advances and future directions. *J. Phys. Chem.* **1996,** *100* (31), 12897-12910.

2. (a) Bowers, M. T.; Kemper, P. R.; Vonhelden, G.; Vankoppen, P. A. M., Gas-phase ion chromatography - transition-metal state selection and carbon cluster formation. *Science* **1993,** *260* (5113), 1446-1451; (b) Jurneczko, E.; Kalapothakis, J.; Campuzano, I. D.; Morris, M.; Barran, P. E., Effects of drift gas on collision cross sections of a protein standard in linear drift tube and traveling wave ion mobility mass spectrometry. *Anal. Chem.* **2012,** *84* (20), 8524-31.

3. Zolotov, Y. A., Ion mobility spectrometry. *J. Anal. Chem.* **2006,** *61* (6), 519-519.

4. (a) Clemmer, D. E.; Jarrold, M. F., Ion mobility measurements and their applications to clusters and biomolecules. *J. Mass Spectrom.* **1997,** *32* (6), 577-592; (b) Dugourd, P.; Hudgins, R. R.; Clemmer, D. E.; Jarrold, M. F., High-resolution ion mobility measurements. *Rev. Sci. Instrum.* **1997,** *68* (2), 1122-1129; (c) Gillig, K. J.; Ruotolo, B.; Stone, E. G.; Russell, D. H.; Fuhrer, K.; Gonin, M.; Schultz, A. J., Coupling high-pressure MALDI with ion mobility/orthogonal time-of flight mass spectrometry. *Anal. Chem.* **2000,** *72* (17), 3965-3971.

5. (a) Jarrold, M. F., Peptides and proteins in the vapor phase. *Annu. Rev. Phys. Chem.* **2000,** *51*, 179-207; (b) Wyttenbach, T.; Kemper, P. R.; Bowers, M. T., Design of a new electrospray ion mobility mass spectrometer. *Int. J. Mass spectrom.* **2001,** *212* (1-3), 13-23.

6. Bohrer, B. C.; Merenbloom, S. I.; Koeniger, S. L.; Hilderbrand, A. E.; Clemmer, D. E., Biomolecule analysis by ion mobility spectrometry. *Annu. Rev.Anal.Chem.* **2008,** *1*, 293-327.

7. Chen, S.-H.; Russell, W. K.; Russell, D. H., Combining Chemical Labeling, Bottom-Up and Top-Down Ion-Mobility Mass Spectrometry To Identify Metal-Binding Sites of Partially Metalated Metallothionein. *Anal. Chem.* **2013,** *85* (6), 3229-3237.

8. Chen, L.; Gao, Y. Q.; Russell, D. H., How Alkali Metal Ion Binding Alters the Conformation Preferences of Gramicidin A: A Molecular Dynamics and Ion Mobility Study. *J. Phys. Chem. A* **2011,** *116* (1), 689-696.

9. Sundarapandian, S.; May, J. C.; McLean, J. A., Dual Source Ion Mobility-Mass Spectrometer for Direct Comparison of Electrospray Ionization and MALDI Collision Cross Section Measurements. *Anal. Chem.* **2010,** *82* (8), 3247-3254.

10. Guevremont, R.; Purves, R. W., Atmospheric pressure ion focusing in a high-field asymmetric waveform ion mobility spectrometer. *Rev. Sci. Instrum.* **1999,** *70* (2), 1370.

11. Guevremont, R., High-field asymmetric waveform ion mobility spectrometry: A new tool for mass spectrometry. *J. Chromatogr. A* **2004,** *1058* (1-2), 3-19.

12. Revercomb, H. E.; Mason, E. A., Theory of plasma chromatography gaseous electrophoresis - review. *Anal. Chem.* **1975,** *47* (7), 970-983.

13. Giles, K.; Pringle, S. D.; Worthington, K. R.; Little, D.; Wildgoose, J. L.; Bateman, R. H., Applications of a travelling wave-based radio-frequency-only stacked ring ion guide. *Rapid Commun. Mass Spectrom.* **2004,** *18* (20), 2401-14.

14. (a) Morsa, D.; Gabelica, V. r.; De Pauw, E., Effective Temperature of Ions in Traveling Wave Ion Mobility Spectrometry. *Anal. Chem.* **2011,** *83* (14), 5775-5782; (b) Merenbloom, S. I.; Flick, T. G.; Williams, E. R., How hot are your ions in TWAVE ion mobility spectrometry? *J. Am. Soc. Mass. Spectrom.* **2012,** *23* (3), 553-62.

15. (a) Mason, E. A.; Schamp, H. W., Mobility of gaseous ions in weak electric fields. *Ann. Phys.* **1958,** *4* (3), 233-270; (b) Mason, E. A.; McDaniel, E. W., In *Transport Properties of Ions in Gases*, Wiley: New York, 1988; pp xvi, 560 p.

16. Shvartsburg, A. A.; Mashkevich, S. V.; Baker, E. S.; Smith, R. D., Optimization of Algorithms for Ion Mobility Calculations. *J. Phys. Chem. A* **2007,** *111* (10), 2002-2010.

17. Shvartsburg, A. A.; Jarrold, M. F., An exact hard-spheres scattering model for the mobilities of polyatomic ions. *Chem. Phys. Lett.* **1996,** *261* (1-2), 86-91.

18. Mesleh, M. F.; Hunter, J. M.; Shvartsburg, A. A.; Schatz, G. C.; Jarrold, M. F., Structural Information from Ion Mobility Measurements: Effects of the Long-Range Potential. *J. Phys. Chem.* **1996,** *100* (40), 16082-16086.

19. Clemmer, D. E.; Hudgins, R. R.; Jarrold, M. F., Naked protein conformations - cytochrome-c in the gas-phase. *J. Am. Chem. Soc.* **1995,** *117* (40), 10141-10142.

20. (a) Fenn, J. B.; Mann, M.; Meng, C. K.; Wong, S. F.; Whitehouse, C. M., Electrospray ionization for mass spectrometry of large biomolecules. *Science* **1989,** *246* (4926), 64-71; (b) Schmidt, A.; Karas, M.; Dülcks, T., Effect of different solution flow rates on analyte ion signals in nano-ESI MS, or: when does ESI turn into nano-ESI? *J. Am. Soc. Mass. Spectrom.* **2003,** *14* (5), 492-500; (c) Manisali, I.; Chen, D. D. Y.; Schneider, B. B., Electrospray ionization source geometry for mass spectrometry: past, present, and future. *TrAC, Trends Anal. Chem.* **2006,** *25* (3), 243-256.

21. Pierson, N. A.; Chen, L.; Valentine, S. J.; Russell, D. H.; Clemmer, D. E., Number of Solution States of Bradykinin from Ion Mobility and Mass Spectrometry Measurements. *J. Am. Chem. Soc.* **2011,** *133* (35), 13810-13813.

22. (a) Henderson, S. C.; Valentine, S. J.; Counterman, A. E.; Clemmer, D. E., ESI/ion trap/ion mobility/time-of-flight mass spectrometry for rapid and sensitive analysis of biomolecular mixtures. *Anal. Chem.* **1999,** *71* (2), 291-301; (b) McLean, J. A.; Ruotolo, B. T.; Gillig, K. J.; Russell, D. H., Ion mobility–mass spectrometry: a new paradigm for proteomics. *Int. J. Mass spectrom.* **2005,** *240* (3), 301-315.

23. Siems, W. F.; Wu, C.; Tarver, E. E.; Hill, H. H.; Larsen, P. R.; McMinn, D. G., Measuring the resolving power of ion mobility spectrometers. *Anal. Chem.* **1994,** *66* (23), 4195-4201.

24. Verbeck, G. F.; Ruotolo, B. T.; Sawyer, H. A.; Gillig, K. J.; Russell, D. H., A fundamental introduction to ion mobility mass spectrometry applied to the analysis of biomolecules. *J. Biomol.Tech.* **2002,** *13* (2), 56-61.

25. Shaffer, S. A.; Tang, K. Q.; Anderson, G. A.; Prior, D. C.; Udseth, H. R.; Smith, R. D., A novel ion funnel for focusing ions at elevated pressure using electrospray ionization mass spectrometry. *Rapid Commun. Mass Spectrom.* **1997,** *11* (16), 1813-1817.

26. Gillig, K. J.; Ruotolo, B. T.; Stone, E. G.; Russell, D. H., An electrostatic focusing ion guide for ion mobility-mass spectrometry. *Int. J. Mass spectrom.* **2004,** *239* (1), 43-49.

27. Dahl, D. A., simion for the personal computer in reflection. *Int. J. Mass spectrom.* **2000,** *200* (1–3), 3-25.

28. Department of Computer Science of PUC-Rio, Brazil. Lua programing language is downloadable from www.lua.org, accessed on September 29, 2013.

29. Soppart, O.; Baumbach, J. I., Comparison of electric fields within drift tubes for ion mobility spectrometry. *Meas. Sci.Technol.* **2000,** *11* (10), 1473-1479.

30. Paschen, F., Ueber die zum Funkenübergang in Luft, Wasserstoff und Kohlensäure bei verschiedenen Drucken erforderliche Potentialdifferenz. *Annalen der Physik* **1889,** *273* (5), 69-96.

31. (a) Silveira, J. A.; Gamage, C. M.; Blase, R. C.; Russell, D. H., Gas-phase ion dynamics in a periodic-focusing DC ion guide. *Int. J. Mass spectrom.* **2010,** *296* (1-3), 36-42; (b) Blase, R. C.; Silveira, J. A.; Gillig, K. J.; Gamage, C. M.; Russell, D. H., Increased ion transmission in IMS: A high resolution, periodic-focusing DC ion guide ion mobility spectrometer. *Int. J. Mass spectrom.* **2011,** *301* (1-3), 166-173; (c) Gamage,

C. M.; Silveira, J. A.; Blase, R. C.; Russell, D. H., Gas-phase ion dynamics in a periodic-focusing DC ion guide (Part II): Discrete transport modes. *Int. J. Mass spectrom.* **2011,** *303* (2-3), 154-163.

32. Guan, S. H.; Marshall, A. G., Stacked-ring electrostatic ion guide. *J. Am. Soc. Mass. Spectrom.* **1996,** *7* (1), 101-106.

33. Douglas, D. J.; French, J. B., Collisional focusing effects in radio-frequency quadrupoles. *J. Am. Soc. Mass. Spectrom.* **1992,** *3* (4), 398-408.

34. (a) Shaffer, S. A.; Prior, D. C.; Anderson, G. A.; Udseth, H. R.; Smith, R. D., An ion funnel interface for improved ion focusing and sensitivity using electrospray ionization mass spectrometry. *Anal. Chem.* **1998,** *70* (19), 4111-9; (b) Shaffer, S. A.; Tolmachev, A.; Prior, D. C.; Anderson, G. A.; Udseth, H. R.; Smith, R. D., Characterization of an improved electrodynamic ion funnel interface for electrospray ionization mass spectrometry. *Anal. Chem.* **1999,** *71* (15), 2957-64; (c) Kim, T.; Tolmachev, A. V.; Harkewicz, R.; Prior, D. C.; Anderson, G.; Udseth, H. R.; Smith, R. D., Design and implementation of a new electrodynamic ion funnel. *Anal. Chem.* **2000,** *72* (10), 2247-55; (d) Tolmachev, A. V.; Kim, T.; Udseth, H. R.; Smith, R. D.; Bailey, T. H.; Futrell, J. H., Simulation-based optimization of the electrodynamic ion funnel for high sensitivity electrospray ionization mass spectrometry. *Int. J. Mass spectrom.* **2000,** *203* (1-3), 31-47; (e) Julian, R. R.; Mabbett, S. R.; Jarrold, M. F., Ion funnels for the masses: experiments and simulations with a simplified ion funnel. *J. Am. Soc. Mass. Spectrom.* **2005,** *16* (10), 1708-12; (f) Page, J. S.; Kelly, R. T.; Tang, K.; Smith, R. D., Ionization and transmission efficiency in an electrospray ionization-mass spectrometry interface. *J. Am. Soc. Mass. Spectrom.* **2007,** *18* (9), 1582-90; (g) Kelly, R. T.; Tolmachev, A. V.; Page, J. S.; Tang, K.; Smith, R. D., The ion funnel: theory, implementations, and applications. *Mass Spectrom. Rev.* **2010,** *29* (2), 294-312.

35. (a) Dehmelt, H. G., Radiofrequency Spectroscopy of Stored Ions I: Storage. In *Advances in Atomic and Molecular Physics*, Bates, D. R.; Immanuel, E., Eds. Academic Press: 1968; Vol. Volume 3, pp 53-72; (b) Gerlich, D., Inhomogeneous Rf-Fields - a Versatile Tool for the Study of Processes with Slow Ions. *Adv. Chem. Phys.* **1992,** *82*, 1-176.

36. (a) Tang, K.; Shvartsburg, A. A.; Lee, H. N.; Prior, D. C.; Buschbach, M. A.; Li, F.; Tolmachev, A. V.; Anderson, G. A.; Smith, R. D., High-sensitivity ion mobility spectrometry/mass spectrometry using electrodynamic ion funnel interfaces. *Anal. Chem.* **2005,** *77* (10), 3330-9; (b) Koeniger, S. L.; Merenbloom, S. I.; Valentine, S. J.; Jarrold, M. F.; Udseth, H. R.; Smith, R. D.; Clemmer, D. E., An IMS-IMS analogue of MS-MS. *Anal. Chem.* **2006,** *78* (12), 4161-4174.

37. Macdonald, F.; Lide, D. R., CRC handbook of chemistry and physics: From paper to web. *Abstr Pap Am Chem S* **2003,** *225*, U552-U552.

38. Fernandez-Lima, F. A.; Becker, C.; Gillig, K. J.; Russell, W. K.; Tichy, S. E.; Russell, D. H., Ion mobility-mass spectrometer interface for collisional activation of mobility separated ions. *Anal. Chem.* **2009,** *81* (2), 618-24.

39. Avila, K.; Moxey, D.; de Lozar, A.; Avila, M.; Barkley, D.; Hof, B., The Onset of Turbulence in Pipe Flow. *Science* **2011,** *333* (6039), 192-196.

40. Warsi, Z. U. A., *Fluid dynamics : theoretical and computational approaches*. 3rd ed.; Taylor & Francis: Boca Raton, 2006; p 845 p.

41. (a) García-Valladares, O., Numerical simulation of non-adiabatic capillary tubes considering metastable region. Part I: Mathematical formulation and numerical model. *Int. J. Refrig.* **2007,** *30* (4), 642-653; (b) Pantazis, S.; Valougeorgis, D., Rarefied gas flow through a cylindrical tube due to a small pressure difference. *Eur. J. Mech. B-Fluid* **2013,** *38* (0), 114-127.

42. Moore, J. H.; Davis, C. C.; Coplan, M. A.; Greer, S. C., *Building scientific apparatus*. 4th ed.; Cambridge University Press: Cambridge, UK ; New York, 2009; p xiii, 647 p.

43. Greene, F. T.; Milne, T. A., Mass Spectrometric Detection of Polymers in Supersonic Molecular Beams. *J. Chem. Phys.* **1963,** *39* (11), 3150-3151.

44. Rues, D., Deleeuw, J.H., Rarefied gas dynamics. *Zeitschrift Fur Flugwissenschaften* **1966,** *14* (10), 459-&.

45. Anderson, J. B.; Fenn, J. B., Velocity Distributions in Molecular Beams from Nozzle Sources. *Phys. Fluids* **1965,** *8* (5), 780-787.

46. Covey, T. R.; Thomson, B. A.; Schneider, B. B., Atmospheric pressure ion sources. *Mass Spectrom. Rev.* **2009,** *28* (6), 870-897.

47. Pauly, H., *Atom, molecule, and cluster beams*. Springer: Berlin ; New York, 2000.

48. White, F. M., *Fluid mechanics*. 6th ed.; McGraw-Hill: New York, 2008; p xiii, 864 p. ill.

49. Scoles, G., *Atomic and Molecular Beam Methods:Volume 1*. Oxford University Press, Inc.,: New York, 1988; Vol. 1.

50. Skyrme, A.; Rodriguez, N.; Ierusalimschy, R., Exploring Lua for Concurrent Programming. *J Univers Comput Sci* **2008,** *14* (21), 3556-3572.

51. Wyttenbach, T.; Helden, G.; Batka, J.; Carlat, D.; Bowers, M., Effect of the long-range potential on ion mobility measurements. *J. Am. Soc. Mass. Spectrom.* **1997,** *8* (3), 275-282.

52. Javahery, G.; Thomson, B., A segmented radiofrequency-only quadrupole collision cell for measurements of ion collision cross section on a triple quadrupole mass spectrometer. *J. Am. Soc. Mass. Spectrom.* **1997,** *8* (7), 697-702.

53. (a) Kim, T.; Tang, K. Q.; Udseth, H. R.; Smith, R. D., A multicapillary inlet jet disruption electrodynamic ion funnel interface for improved sensitivity using atmospheric pressure ion sources. *Anal. Chem.* **2001,** *73* (17), 4162-4170; (b) Tang, K. Q.; Tolmachev, A. V.; Nikolaev, E.; Zhang, R.; Belov, M. E.; Udseth, H. R.; Smith, R. D., Independent control of ion transmission in a jet disrupter dual-channel ion funnel electrospray ionization MS interface. *Anal. Chem.* **2002,** *74* (20), 5431-5437.

54. Baykut, G.; von Halem, O.; Raether, O., Applying a dynamic method to the measurement of ion mobility. *J. Am. Soc. Mass. Spectrom.* **2009,** *20* (11), 2070-81.

55. Jarrold, M. F., Drift-tube studies of atomic clusters. *J. Phys. Chem.* **1995,** *99* (1), 11-21.

56. Tang, X.; Bruce, J. E.; Hill, H. H., Design and performance of an atmospheric pressure ion mobility Fourier transform ion cyclotron resonance mass spectrometer. *Rapid Commun. Mass Spectrom.* **2007,** *21* (7), 1115-1122.

57. Kemper, P. R.; Dupuis, N. F.; Bowers, M. T., A new, higher resolution, ion mobility mass spectrometer. *Int. J. Mass spectrom.* **2009,** *287* (1-3), 46-57.

58. (a) Badman, E. R.; Hoaglund-Hyzer, C. S.; Clemmer, D. E., Monitoring structural changes of proteins in an ion trap over similar to 10-200 ms: Unfolding transitions in cytochrome c ions. *Anal. Chem.* **2001,** *73* (24), 6000-6007; (b) Myung, S.; Badman, E. R.; Lee, Y. J.; Clemmer, D. E., Structural transitions of electrosprayed ubiquitin ions stored in an ion trap over similar to 10 ms to 30 s. *J. Phys. Chem. A* **2002,** *106* (42), 9976-9982.

59. Knorr, F. J.; Eatherton, R. L.; Siems, W. F.; Hill, H. H., Fourier-transform ion mobility spectrometry. *Anal. Chem.* **1985,** *57* (2), 402-406.

60. Chen, Y. H.; Siems, W. F.; Hill, H. H., Fourier transform electrospray ion mobility spectrometry. *Anal. Chim. Acta* **1996,** *334* (1-2), 75-84.

61. Belov, M. E.; Buschbach, M. A.; Prior, D. C.; Tang, K.; Smith, R. D., Multiplexed ion mobility spectrometry-orthogonal time-of-flight mass spectrometry. *Anal. Chem.* **2007,** *79* (6), 2451-62.

62. Fuhrer, K., Gonin, Marc, Gillig, Kent J., Egan, Thomas, Mccully, Michael I., Schultz, John A. Time-of-flight mass spectrometer for monitoring of fast processes U.S. Patent 79019286. 2006.

63. Bradbury, N. E.; Nielsen, R. A., Absolute values of the electron mobility in hydrogen. *Physical Review* **1936,** *49* (5), 0388-0393.

64. Kelly, R. T.; Page, J. S.; Tang, K.; Smith, R. D., Array of Chemically Etched Fused-Silica Emitters for Improving the Sensitivity and Quantitation of Electrospray Ionization Mass Spectrometry. *Anal. Chem.* **2007,** *79* (11), 4192-4198.

65. (a) Wu, X.-G., Ion dynamics in non-perfect quadrupole traps. *Int. J. Mass spectrom.* **2007,** *263* (1), 59-65; (b) Collings, B., Fragmentation of ions in a low pressure linear ion trap. *J. Am. Soc. Mass. Spectrom.* **2007,** *18* (8), 1459-1466.

66. Jovanovic, B.; Stankovic, K.; Vujisic, M.; Osmokrovic, P., Initiation and progress of breakdown in the range to the left of the paschen minimum. *IEEE T. Dielect. El. In.* **2011,** *18* (4), 954-963.

67. Wiley, W. C.; McLaren, I. H., Time-of-Flight Mass Spectrometer with Improved Resolution. *Rev. Sci. Instrum.* **1955,** *26* (12), 1150-1157.

68. Ross, A. S.; Luettgen, S., Speciation of cyclo(Pro-Gly)3 and its divalent metal-ion complexes by electrospray ionization mass spectrometry. *J. Am. Soc. Mass. Spectrom.* **2005,** *16* (9), 1536-1544.

69. Burgus, R.; Ling, N.; Butcher, M.; Guillemin, R., Primary Structure of Somatostatin, A Hypothalamic Peptide That Inhibits the Secretion of Pituitary Growth Hormone. *P. Natl. Acad. Sci.* **1973,** *70* (3), 684-688.

70. (a) Cochran, A. G.; Skelton, N. J.; Starovasnik, M. A., Tryptophan zippers: stable, monomeric beta -hairpins. *P. Natl. Acad. Sci.* **2001,** *98* (10), 5578-83; (b) Chen, L.; Shao, Q.; Gao, Y. Q.; Russell, D. H., Molecular dynamics and ion mobility spectrometry study of model beta-hairpin peptide, trpzip1. *J. Phys. Chem. A* **2011,** *115* (17), 4427-35.

71. Giles, K., Travelling wave ion mobility. *Int. J. Ion Mobil. Spectrom.* **2013,** *16* (1), 1-3.

72. Shi, H.; Pierson, N. A.; Valentine, S. J.; Clemmer, D. E., Conformation types of ubiquitin [M+8H]8+ Ions from water:methanol solutions: evidence for the N and A States in aqueous solution. *J. Phys. Chem. B* **2012,** *116* (10), 3344-52.

73. Ruotolo, B. T.; Benesch, J. L.; Sandercock, A. M.; Hyung, S. J.; Robinson, C. V., Ion mobility-mass spectrometry analysis of large protein complexes. *Nat. Protoc.* **2008,** *3* (7), 1139-52.

74. (a) Giles, K.; Wildgoose, J. L.; Langridge, D. J.; Campuzano, I., A method for direct measurement of ion mobilities using a travelling wave ion guide. *Int. J. Mass spectrom.* **2010,** *298* (1-3), 10-16; (b) Thalassinos, K.; Slade, S. E.; Jennings, K. R.; Scrivens, J. H.; Giles, K.; Wildgoose, J.; Hoyes, J.; Bateman, R. H.; Bowers, M. T., Ion mobility mass spectrometry of proteins in a modified commercial mass spectrometer. *Int. J. Mass spectrom.* **2004,** *236* (1-3), 55-63.

75. Silveira, J. A.; Jeon, J.; Gamage, C. M.; Pai, P. J.; Fort, K. L.; Russell, D. H., Damping factor links periodic focusing and uniform field ion mobility for accurate determination of collision cross sections. *Anal. Chem.* **2012,** *84* (6), 2818-24.

76. Wyttenbach, T.; Bowers, M. T., Structural stability from solution to the gas phase: native solution structure of ubiquitin survives analysis in a solvent-free ion mobility-mass spectrometry environment. *J. Phys. Chem. B* **2011,** *115* (42), 12266-75.

77. Hannis, J. C.; Muddiman, D. C., Nanoelectrospray mass spectrometry using non-metalized, tapered (50 → 10 μm) fused-silica capillaries. *Rapid Commun. Mass Spectrom.* **1998,** *12* (8), 443-448.

78. Counterman, A. E.; Valentine, S. J.; Srebalus, C. A.; Henderson, S. C.; Hoaglund, C. S.; Clemmer, D. E., High-order structure and dissociation of gaseous peptide aggregates that are hidden in mass spectra. *J. Am. Soc. Mass. Spectrom.* **1998,** *9* (8), 743-759.

79. Baker, E. S.; Clowers, B. H.; Li, F.; Tang, K.; Tolmachev, A. V.; Prior, D. C.; Belov, M. E.; Smith, R. D., Ion mobility spectrometry-mass spectrometry performance using electrodynamic ion funnels and elevated drift gas pressures. *J. Am. Soc. Mass. Spectrom.* **2007,** *18* (7), 1176-87.

80. Bush, M. F.; Hall, Z.; Giles, K.; Hoyes, J.; Robinson, C. V.; Ruotolo, B. T., Collision Cross Sections of Proteins and Their Complexes: A Calibration Framework and Database for Gas-Phase Structural Biology. *Anal. Chem.* **2010,** *82* (22), 9557-9565.

81. Gill, A. C.; Jennings, K. R.; Wyttenbach, T.; Bowers, M. T., Conformations of biopolymers in the gas phase: a new mass spectrometric method. *Int. J. Mass spectrom.* **2000,** *195–196* (0), 685-697.

82. Poully, J.-C.; Grégoire, G.; Ballivian, R.; Dugourd, P.; Schermann, J. P., Coupling infrared multiphoton dissociation spectroscopy, mass-spectrometry and ion mobility spectrometry for the determination of structures of angiotensin II cations. *Vib. Spectrosc* **2011,** *56* (1), 105-109.

83. Florance, H. V.; Stopford, A. P.; Kalapothakis, J. M.; McCullough, B. J.; Bretherick, A.; Barran, P. E., Evidence for alpha-helices in the gas phase: a case study using Melittin from honey bee venom. *The Analyst* **2011,** *136* (17), 3446-52.

84. Valentine, S. J.; Counterman, A. E.; Clemmer, D. E., Conformer-dependent proton-transfer reactions of ubiquitin ions. *J. Am. Soc. Mass. Spectrom.* **1997,** *8* (9), 954-961.

85. Shelimov, K. B.; Clemmer, D. E.; Hudgins, R. R.; Jarrold, M. F., Protein structure in vacuo: Gas-phase confirmations of BPTI and cytochrome c. *J. Am. Chem. Soc.* **1997,** *119* (9), 2240-2248.

86. Wyttenbach, T.; vonHelden, G.; Bowers, M. T., Gas-phase conformation of biological molecules: Bradykinin. *J. Am. Chem. Soc.* **1996,** *118* (35), 8355-8364.

87. Lee, S. C.; Russell, A. F.; Laidig, W. D., 3-Dimensional sutructure of bradykinin in SDS miscelles - study using nuclear-magnetic-resonance, distance geometry, and restrained molecular mechanics and dynamics. *Int. J. Pept. Protein Res.* **1990,** *35* (5), 367-377.

88. Sawyer, H. A.; Marini, J. T.; Stone, E. G.; Ruotolo, B. T.; Gillig, K. J.; Russell, D. H., The structure of gas-phase bradykinin fragment 1-5 (RPPGF) ions: an ion mobility spectrometry and H/D exchange ion-molecule reaction chemistry study. *J. Am. Soc. Mass. Spectrom.* **2005,** *16* (6), 893-905.

89. Purves, R. W.; Barnett, D. A.; Ells, B.; Guevremont, R., Gas-phase conformers of the [M + 2H](2+) ion of bradykinin investigated by combining high-field asymmetric waveform ion mobility spectrometry, hydrogen/deuterium exchange, and energy-loss measurements. *Rapid Commun. Mass Spectrom.* **2001,** *15* (16), 1453-6.

90. Shvartsburg, A. A.; Smith, R. D., Fundamentals of traveling wave ion mobility spectrometry. *Anal. Chem.* **2008,** *80* (24), 9689-99.

91. Chirot, F.; Calvo, F.; Albrieux, F.; Lemoine, J.; Tsybin, Y.; Dugourd, P., Statistical Analysis of Ion Mobility Spectrometry. I. Unbiased and Guided Replica-Exchange Molecular Dynamics. *J. Am. Soc. Mass. Spectrom.* **2012,** *23* (2), 386-396.

92. Lee, Y. J.; Hoaglund-Hyzer, C. S.; Taraszka, J. A.; Zientara, G. A.; Counterman, A. E.; Clemmer, D. E., Collision-induced dissociation of mobility-separated ions using an orifice-skimmer cone at the back of a drift tube. *Anal. Chem.* **2001,** *73* (15), 3549-55.

93. Covey, T.; Douglas, D. J., Collision cross-sections for protein ions. *J. Am. Soc. Mass. Spectrom.* **1993,** *4* (8), 616-623.

94. Badman, E. R.; Hoaglund-Hyzer, C. S.; Clemmer, D. E., Dissociation of different conformations of ubiquitin ions. *J. Am. Soc. Mass. Spectrom.* **2002,** *13* (6), 719-723.

95. (a) Li, J. W.; Taraszka, J. A.; Counterman, A. E.; Clemmer, D. E., Influence of solvent composition and capillary temperature on the conformations of electrosprayed ions: unfolding of compact ubiquitin conformers from pseudonative and denatured solutions. *Int. J. Mass spectrom.* **1999,** *185*, 37-47; (b) Koeniger, S. L.; Merenbloom, S. I.; Clemmer, D. E., Evidence for many resolvable structures within conformation types of electrosprayed ubiquitin ions. *J. Phys. Chem. B* **2006,** *110* (13), 7017-7021.

96. Koeniger, S. L.; Clemmer, D. E., Resolution and structural transitions of elongated states of ubiquitin. *J. Am. Soc. Mass. Spectrom.* **2007,** *18* (2), 322-31.

97. Shannon, R., Revised effective ionic radii and systematic studies of interatomic distances in halides and chalcogenides. *Acta Crystallogr. A* **1976,** *32* (5), 751-767.

98. Berova, N.; Nakanishi, K. j.; Woody, R., *Circular dichroism : principles and applications*. 2nd ed.; Wiley-VCH: New York, 2000; p xix, 877 p.

99. Pierson, N. A.; Chen, L.; Russell, D. H.; Clemmer, D. E., Cis-Trans Isomerizations of Proline Residues Are Key to Bradykinin Conformations. *J. Am. Chem. Soc.* **2013,** *135* (8), 3186-3192.

100. van der Spoel, D.; Marklund, E. G.; Larsson, D. S. D.; Caleman, C., Proteins, Lipids, and Water in the Gas Phase. *Macromol. Biosci.* **2011,** *11* (1), 50-59.

101. Baker, D., A surprising simplicity to protein folding. *Nature* **2000,** *405* (6782), 39-42.

102. Anfinsen, C. B., Principles that Govern the Folding of Protein Chains. *Science* **1973,** *181* (4096), 223-230.

103. Wolynes, P. G., Energy landscapes and solved protein–folding problems. *Philos. T. R. Soc. A* **2005,** *363* (1827), 453-467.

104. Wright, P. J.; Zhang, J.; Douglas, D. J., Conformations of gas-phase ions of ubiquitin, cytochrome c, apomyoglobin, and β-lactoglobulin produced from two different solution conformations. *J. Am. Soc. Mass. Spectrom.* **2008,** *19* (12), 1906-1913.

105. Whitehouse, C. M.; Dreyer, R. N.; Yamashita, M.; Fenn, J. B., Electrospray interface for liquid chromatographs and mass spectrometers. *Anal. Chem.* **1985,** *57* (3), 675-679.

106. Vijaykumar, S.; Bugg, C. E.; Cook, W. J., Structure of ubiquitin refined at 1.8 A resolution. *J. Mol. Biol.* **1987,** *194* (3), 531-544.

107. (a) Chernushevich, I. V.; Thomson, B. A., Collisional cooling of large ions in electrospray mass spectrometry. *Anal. Chem.* **2004,** *76* (6), 1754-1760; (b) Tolmachev, A. V.; Vilkov, A. N.; Bogdanov, B.; Pasa-Tolic, L.; Masselon, C. D.; Smith, R. D., Collisional activation of ions in RF ion traps and ion guides: the effective ion temperature treatment. *J. Am. Soc. Mass. Spectrom.* **2004,** *15* (11), 1616-28.

108. Wysocki, V. H.; Kenttämaa, H. I.; Cooks, R. G., Internal energy distributions of isolated ions after activation by various methods. *Int. J. Mass Spectrom. Ion Processes* **1987,** *75* (2), 181-208.

109. Poehler, T.; Kunte, R.; Hoenen, H.; Jeschke, P.; Wissdorf, W.; Brockmann, K. J.; Benter, T., Numerical Simulation and Experimental Validation of the Three-Dimensional Flow Field and Relative Analyte Concentration Distribution in an Atmospheric Pressure Ion Source. *J. Am. Soc. Mass. Spectrom.* **2011,** *22* (11), 2061-2069.

110. McLean, J. R.; McLean, J. A.; Wu, Z.; Becker, C.; Perez, L. M.; Pace, C. N.; Scholtz, J. M.; Russell, D. H., Factors that influence helical preferences for singly charged gas-phase peptide ions: the effects of multiple potential charge-carrying sites. *J. Phys. Chem. B* **2010,** *114* (2), 809-16.

111. Stretton, A. O. W., The first sequence: Fred Sanger and insulin. *Genetics* **2002,** *162* (2), 527-532.

112. (a) Tokihiro, K.; Irie, T.; Hirayama, F.; Uekama, K., Mass Spectroscopic Evidence on Inhibiting Effect of Maltosyl–β-Cyclodextrin on Insulin Self-association. *Pharm. Pharmacol. Commun.* **1996,** *2* (11), 519-522; (b) Pagnotti, V. S.; Chubatyi, N. D.; McEwen, C. N., Solvent Assisted Inlet Ionization: An Ultrasensitive New Liquid Introduction Ionization Method for Mass Spectrometry. *Anal. Chem.* **2011,** *83* (11), 3981-3985; (c) Wang, B.; Lietz, C. B.; Inutan, E. D.; Leach, S. M.; Trimpin, S., Producing Highly Charged Ions without Solvent Using Laserspray Ionization: A Total Solvent-Free Analysis Approach at Atmospheric Pressure. *Anal. Chem.* **2011,** *83* (11), 4076-4084.

113. Salbo, R.; Bush, M. F.; Naver, H.; Campuzano, I.; Robinson, C. V.; Pettersson, I.; Jorgensen, T. J.; Haselmann, K. F., Traveling-wave ion mobility mass spectrometry of protein complexes: accurate calibrated collision cross-sections of human insulin oligomers. *Rapid Commun. Mass Spectrom.* **2012,** *26* (10), 1181-93.

114. (a) Ruotolo, B. T.; Giles, K.; Campuzano, I.; Sandercock, A. M.; Bateman, R. H.; Robinson, C. V., Evidence for Macromolecular Protein Rings in the Absence of Bulk Water. *Science* **2005,** *310* (5754), 1658-1661; (b) Jarrold, M.; Constant, V., Silicon cluster ions: Evidence for a structural transition. *Phys. Rev. Lett.* **1991,** *67* (21), 2994-2997.

115. Williams, D. M.; Pukala, T. L., Novel insights into protein misfolding diseases revealed by ion mobility-mass spectrometry. *Mass Spectrom. Rev.* **2013,** *32* (3), 169-187.

116. Schultz, R. H.; Armentrout, P. B., The charge-transfer reaction N^{+}_{2} (X, v = 0) + Ar → Ar^{+} + N_2 from thermal to 20 eV C.M. *Chem. Phys. Lett.* **1991,** *179* (5−6), 429-434.

117. Peng, Y. E.; Zhang, S.; Gong, X.; Ma, X.; Yang, C.; Zhang, X., Controlling Charge States of Peptides through Inductive Electrospray Ionization Mass Spectrometry. *Anal. Chem.* **2011,** *83* (23), 8863-8866.

APPENDIX

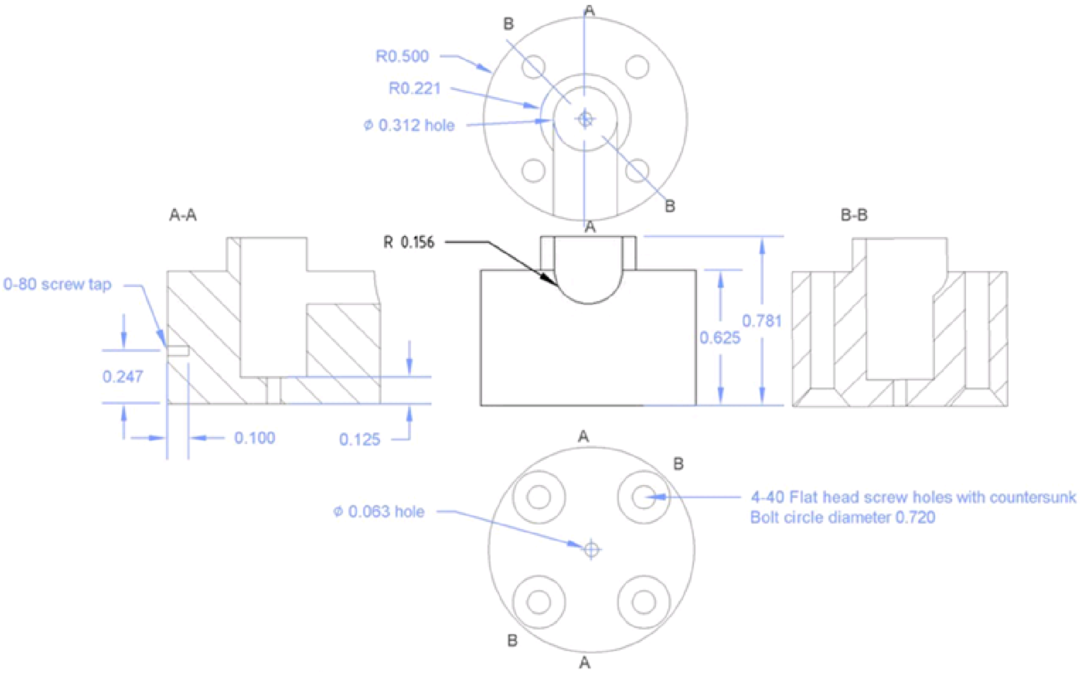

A 1. Heated capillary head cover (Alumimum)

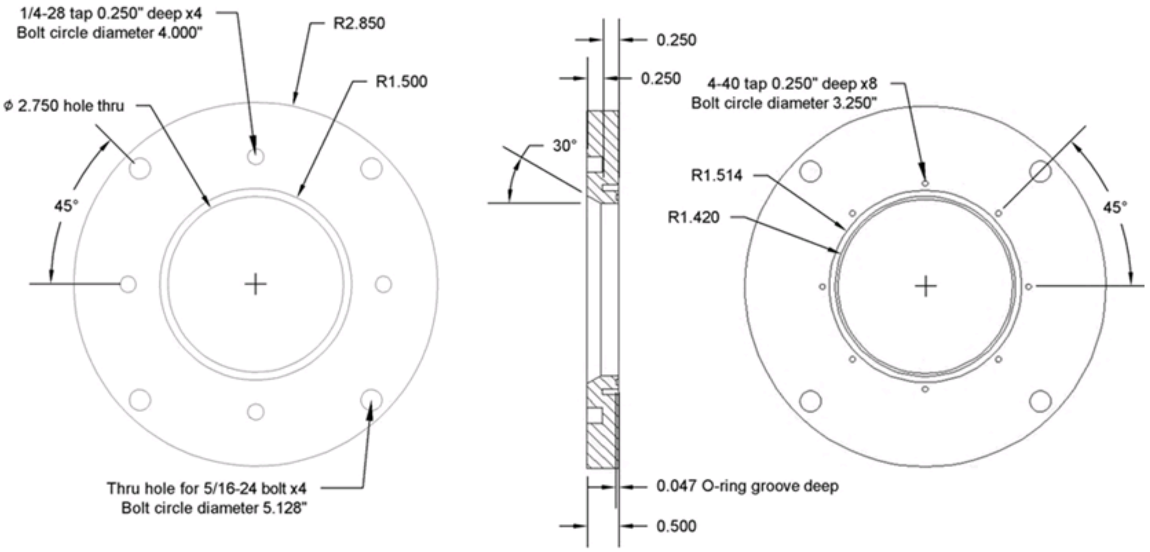

A 2. ESI source cover flange

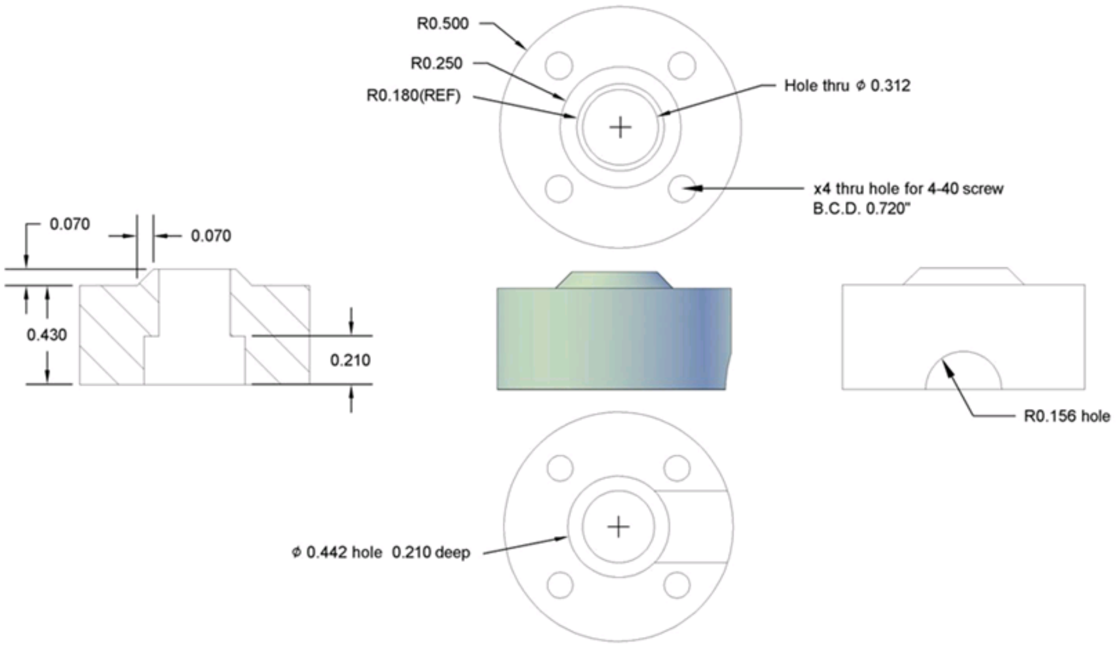

A 3. Heated capillary insert (PEEK)

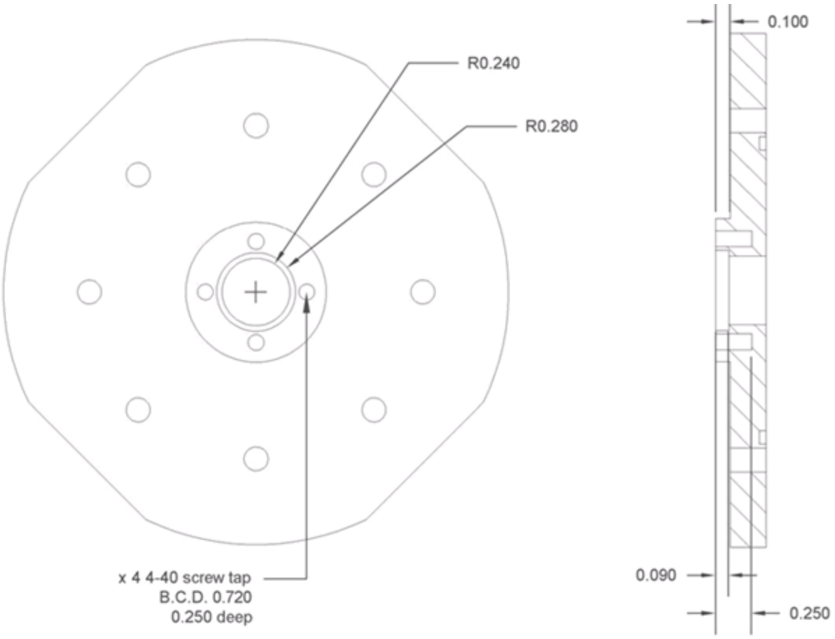

A 4. Heated capillary-bellows coupler (PEEK)

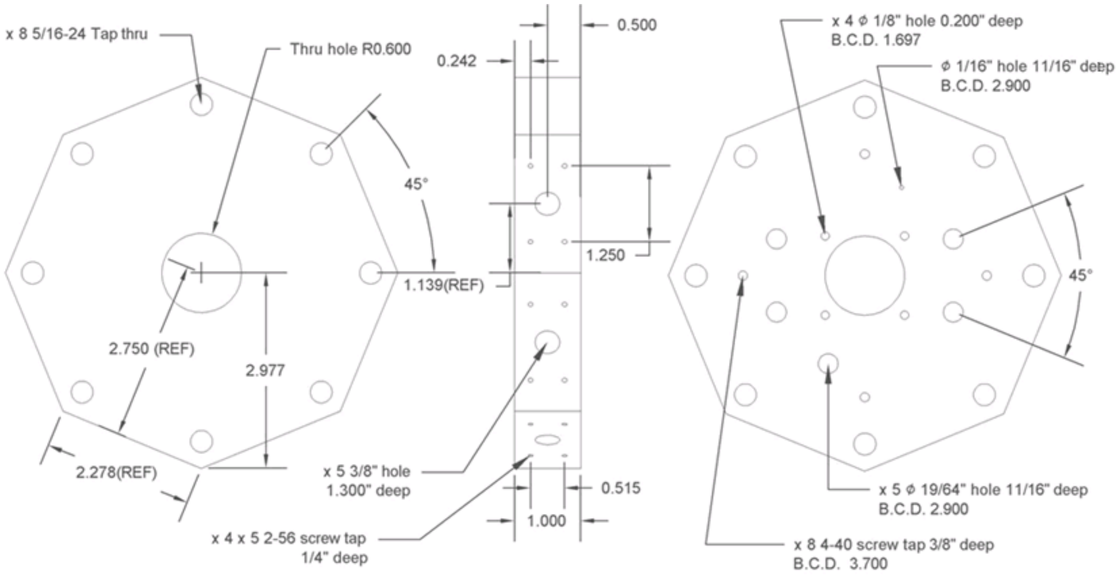

A 5. Ion funnel support and feedthru flange

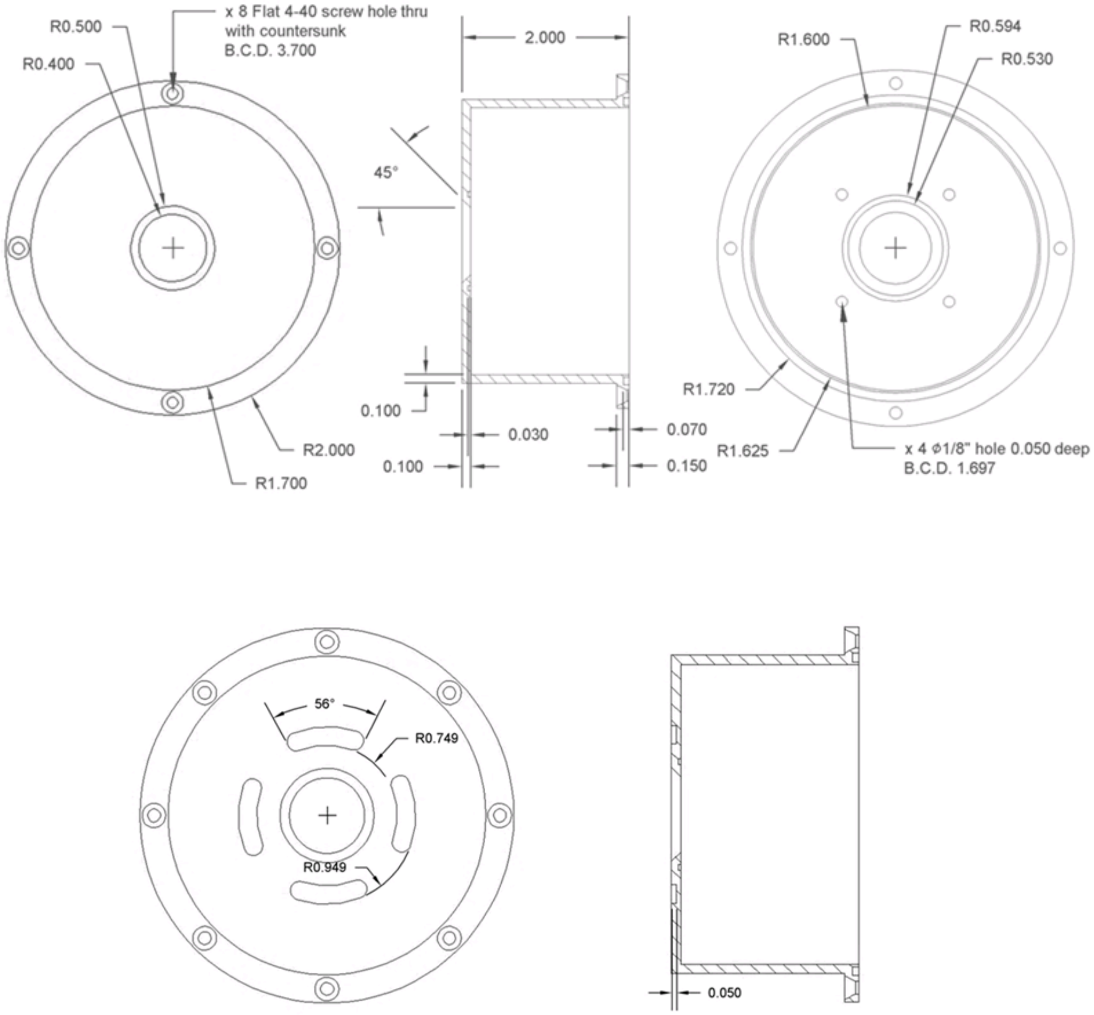

A 6. Ion funnel enclosure

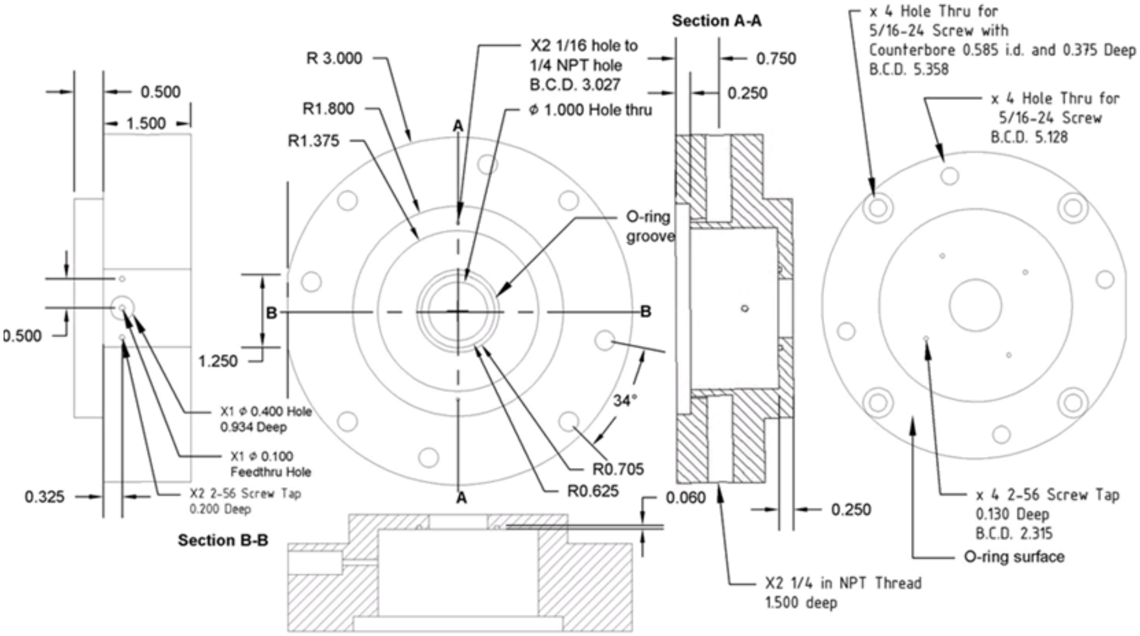

A 7. Front flange of the first PFIG module

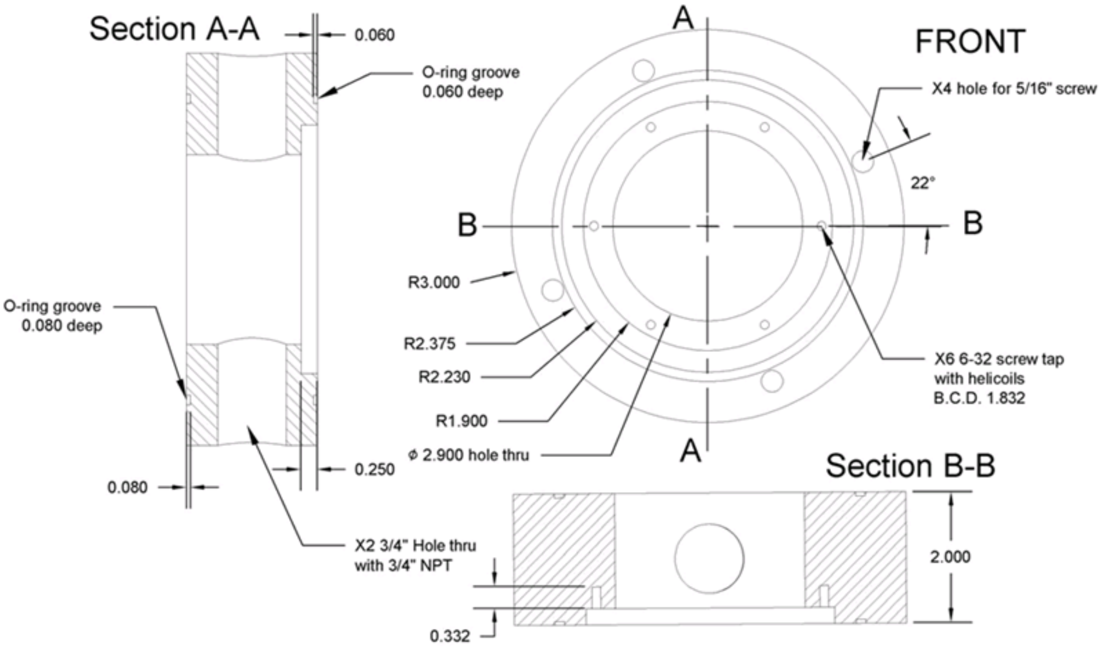

A 8. Differential pumping chamber attached to TOF MS

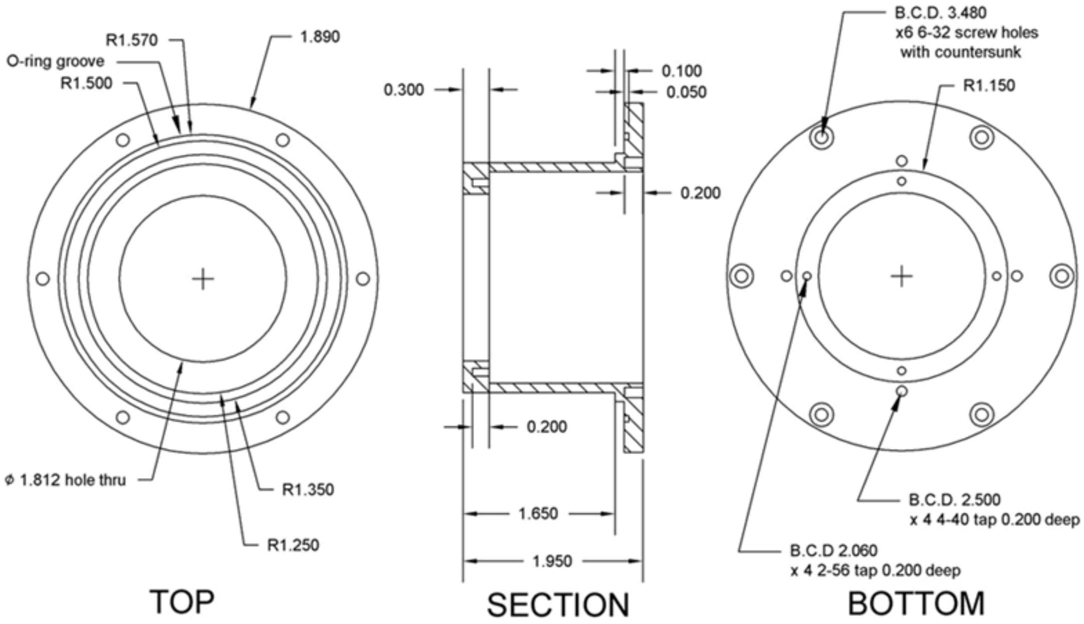

A 9. Ion transfer optic enclosure (to TOF MS)

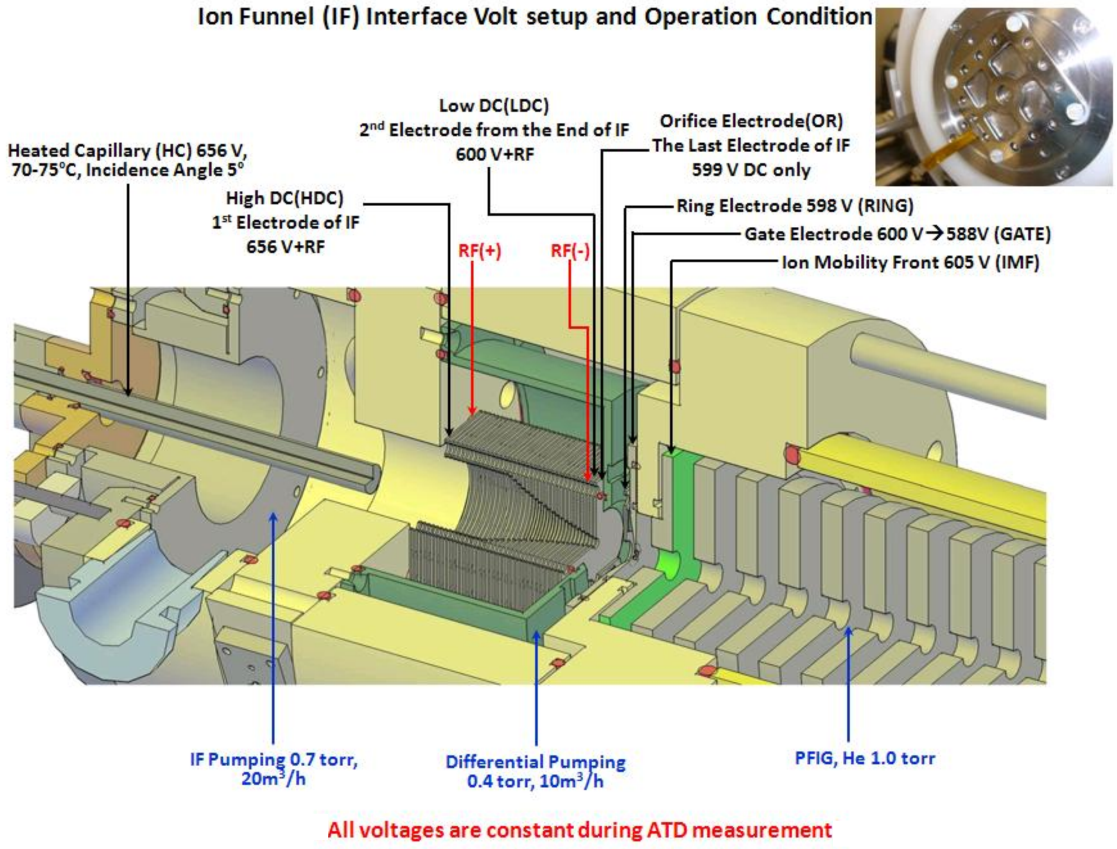

A 10. Voltage setup and schematic for the rf IF interface

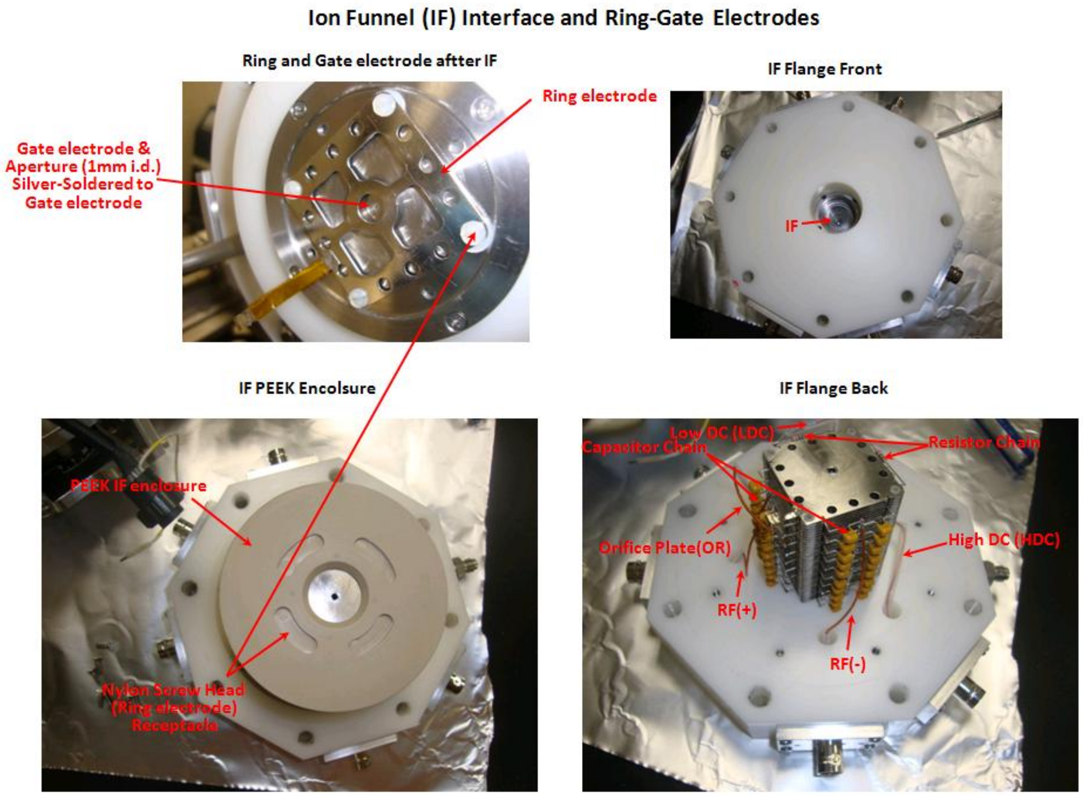

A 11. Photos of wiring and assembly of the rf IF interface and ring-gate electrodes

Ion Transfer Optics Volt setup and Operation Condition (in TOF)

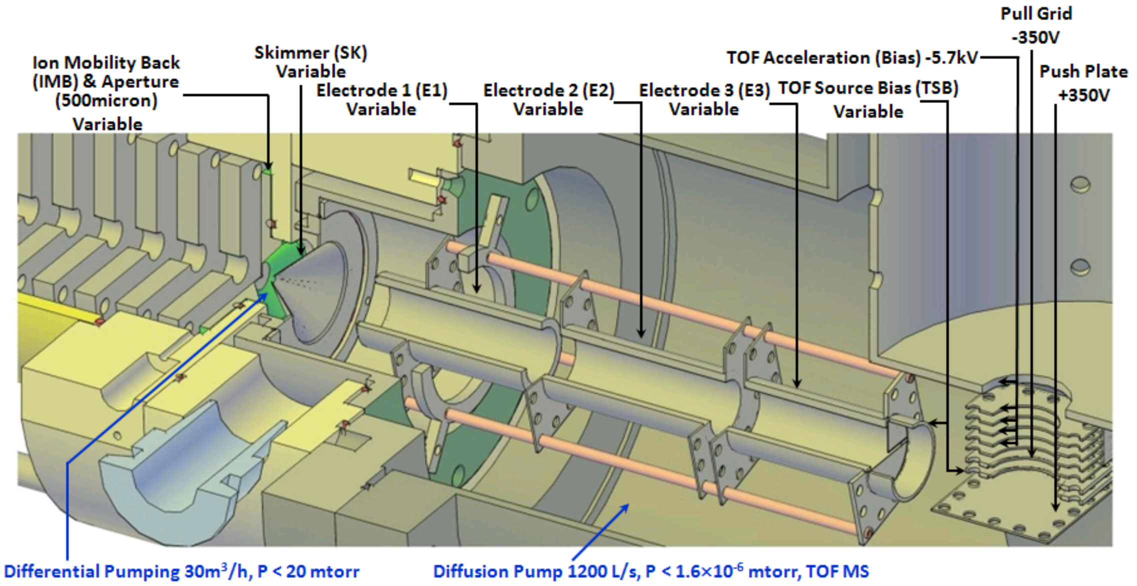

Volt set	Electrodes				
	Ion Mobility Back (IMB)	Skimmer (SK)	Electrode 1 (E1)	Electrode 2 (E2)	Electrode 3 (=TOF Source Bias, TSB)
A	1	3	29	111	256
B	103	104	130	212	358
C	205	207	232	313	450
D	307	308	334	415	552
E	409	411	435	518	659
F	513	515	539	622	767

All voltages are negative and accordingly adjusted from the Volt set F to A during ATD measurement

A 12. Ion transfer optics and voltages setup for ATD measurements

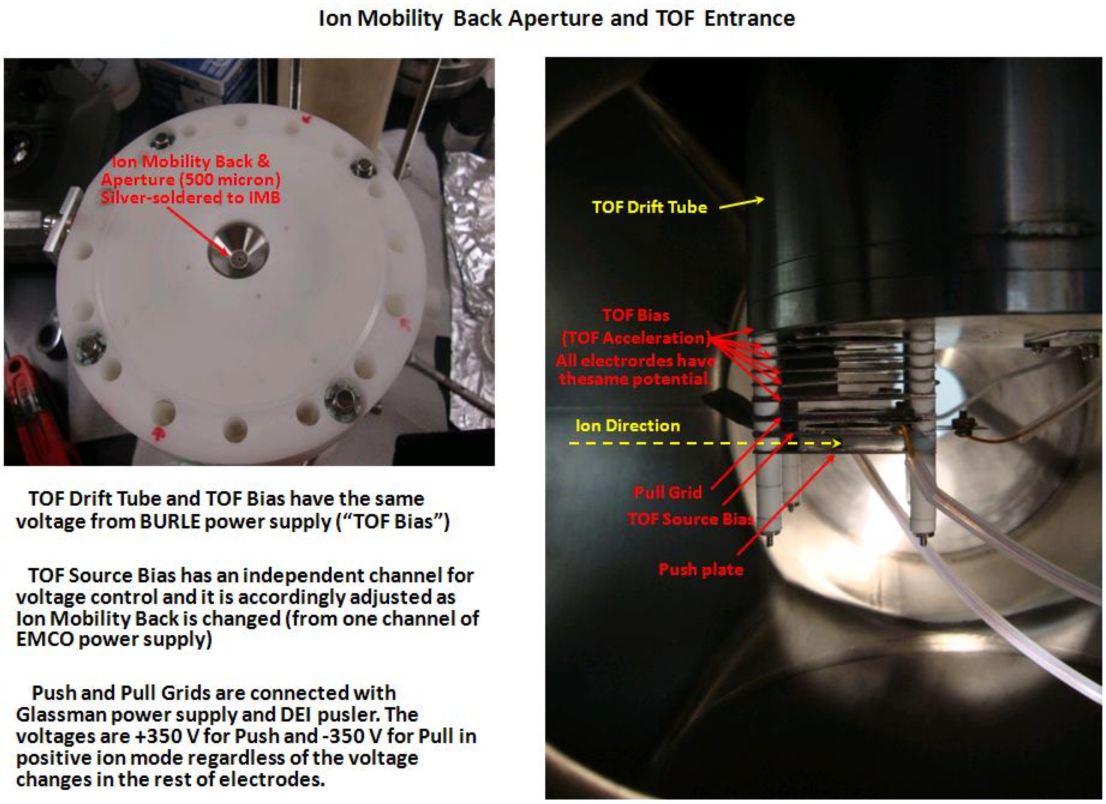

Ion Mobility Back Aperture and TOF Entrance

TOF Drift Tube and TOF Bias have the same voltage from BURLE power supply (“TOF Bias”)

TOF Source Bias has an independent channel for voltage control and it is accordingly adjusted as Ion Mobility Back is changed (from one channel of EMCO power supply)

Push and Pull Grids are connected with Glassman power supply and DEI pusler. The voltages are +350 V for Push and -350 V for Pull in positive ion mode regardless of the voltage changes in the rest of electrodes.

A 13. Mobility back aperture and TOF entrance

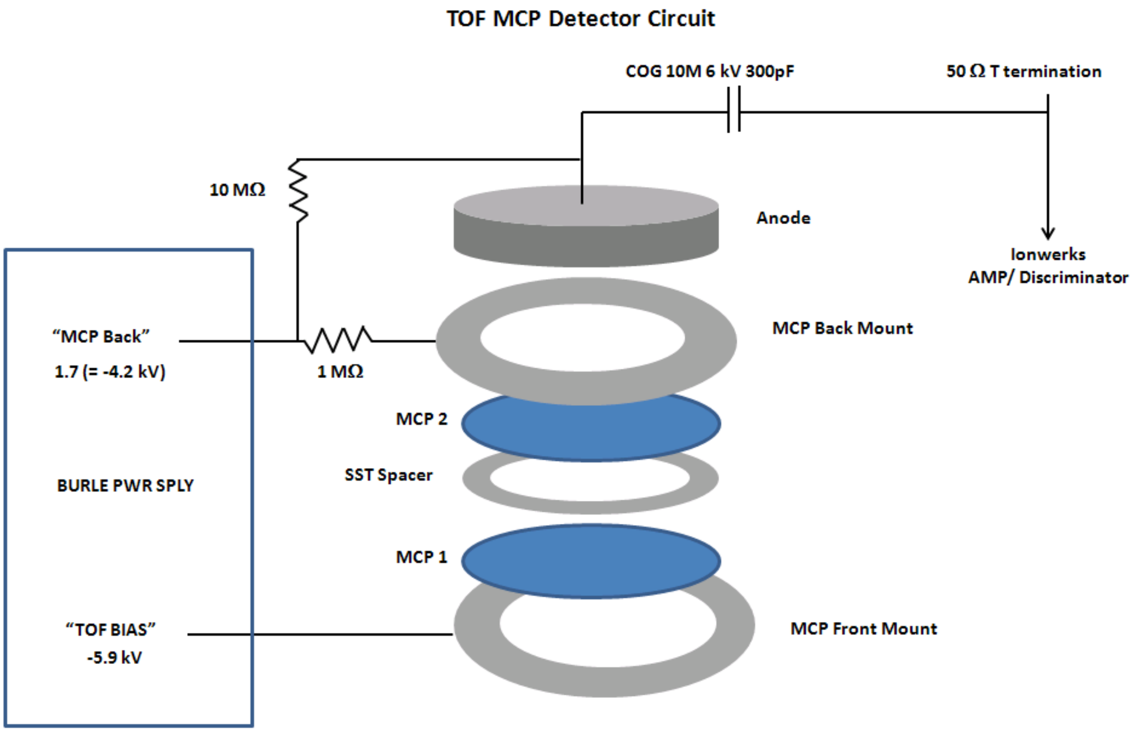

A 14. Electrical connection of TOF MS MCP detector

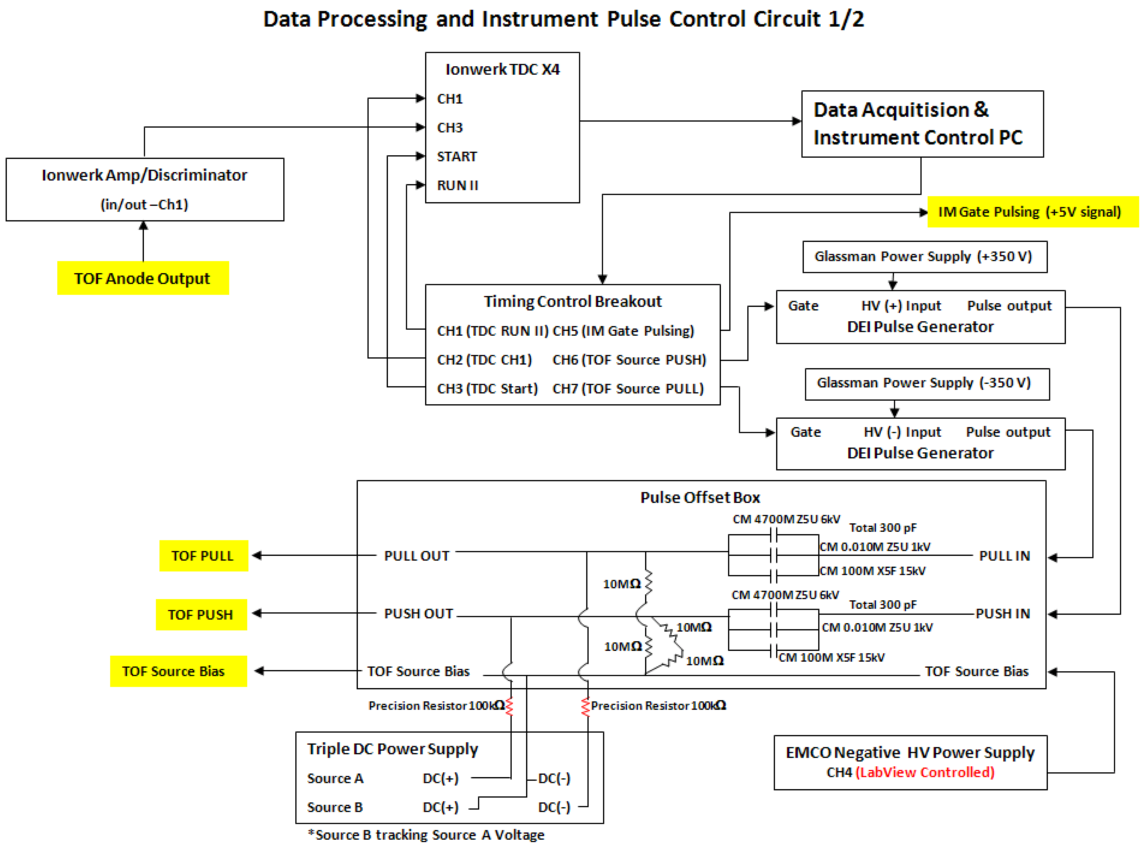

A 15. Data acquisition and instrument pulse control

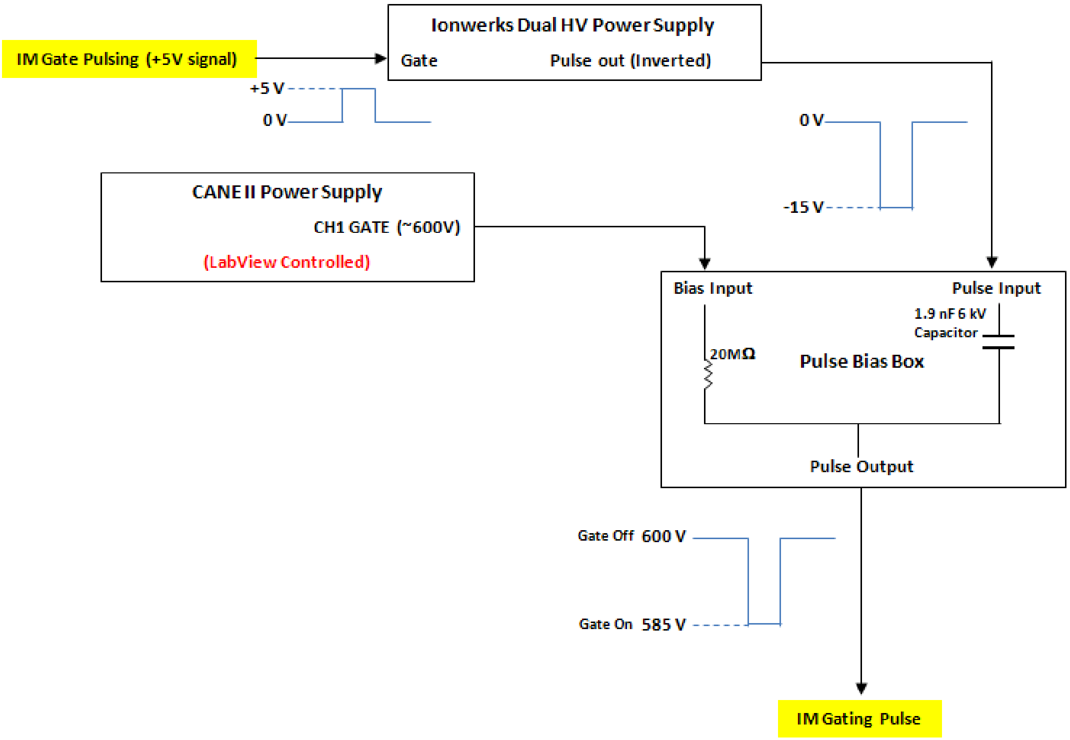

Data Processing and Instrument Pulse Control Circuit 2/2

A 16. Pulse generation for ion mobility gating

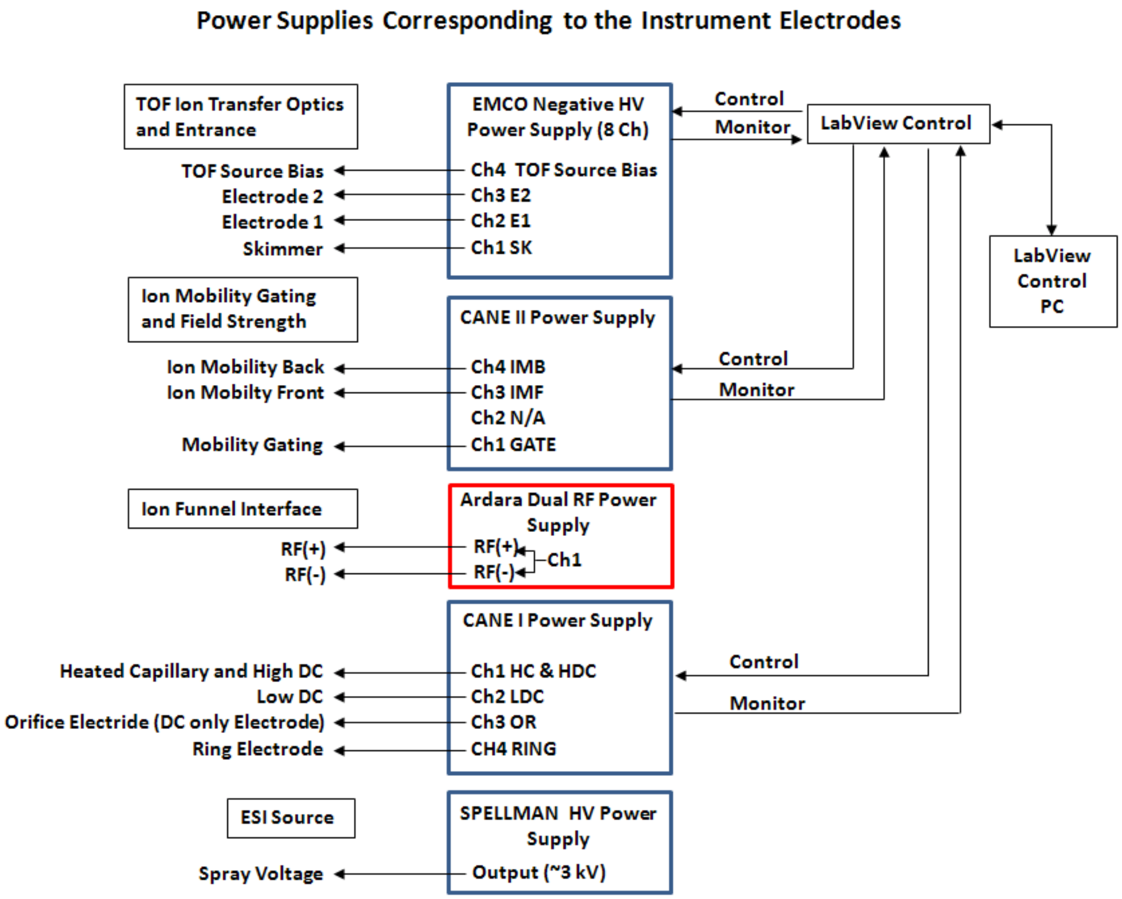

A 17. Instrument electrodes and corresponding power supply